Analytic Properties of the Quark Propagator: QED_3, QCD and Kaon Photoproduction

Dissertation

zur Erlangung des Grades eines Doktors
der Naturwissenschaften

der Fakultät für Physik
der Eberhard–Karls–Universität zu Tübingen

vorgelegt von
Steven Ahlig
aus Lauterbach

2001

Tag der mündlichen Prüfung: 25. Juli 2001
Dekan: Prof. Dr. G. J. Wagner
1. Berichterstatter: Priv. Doz. Dr. R. Alkofer
2. Berichterstatter: Prof. Dr. H. Müther

Abstract

Confinement and dynamical chiral symmetry breaking are the basic phenomena of strong interactions. However, these fundamental issues are not understood in a satisfactory way. Especially the confinement problem is still unsolved albeit various ideas have been developed. Neither dynamical chiral symmetry breaking nor confinement can be explained within perturbation theory. Therefore it is necessary to employ genuin non–perturbative methods. The Dyson–Schwinger approach proves to be well suited since it yields the basic Greens functions: the gluon- and quark propagators. Previous studies strongly support the assumption that the propagators actually do indicate dynamical chiral symmetry breaking as well as confinement.

In the first chapter the electron propagator for (2+1)–dimensional Quantum Electrodynamics (QED_3) is investigated within the Dyson–Schwinger approach. It will be shown for two different truncation schemes that QED_3 has a phase where the electrons are confined and where the chiral symmetry is spontaneously broken. Because of this close similarity of QED_3 and Quantum Chromodynamics (QCD) it is interesting to compare the analytic structure of the fermion propagator for both theories. The results for the electron propagator in the confined phase of QED_3 are qualitatively different from the corresponding results in the unconfined phase. This strongly indicates that the propagator actually does contain the confinement signature.

In the main part the coupled system of Dyson–Schwinger equations for the gluon-, quark-, and ghost propagators of Landau gauge QCD is solved. The solutions are discussed for all $0 \leq N_f \leq 6$ and for various quark masses. The results show that the chiral symmetry is spontaneously broken and that gluons are confined via the violation of the positivity constraints. No postitivity violation could be found for the quark propagator, however, the results are very similar to the results for the electron propagator in QED_3 in the confined phase. Furthermore it has been found that for all $0 \leq N_f \leq 6$ the gluon propagator is infrared vanishing whereas the ghost propagator is infrared diverging. This infrared behaviour of the propagators implies that the running coupling α_s for all $0 \leq N_f \leq 6$ has an infrared fixed point at $\alpha_s \approx 9.5$.

In the last chapter it is shown that meson production processes can give constraints on the quark propagator for time–like momenta. This complements the Dyson–Schwinger studies which are set up in Euclidean space and thus yield the propagator only for space–like momenta. Kaon photoproduction will be shown to be especially well suited for these investigations and the corresponding cross sections are calculated within the covariant diquark–quark model. Hereby different possibilities for the implementation of confinement at the level of the propagators are compared. The results for the cross sections clearly show that a realistic quark propagator must not rise for time–like momenta. This especially entails that exponential type propagators are no valid approximation of the quark propagator.

Zusammenfassung

Confinement und dynamische chirale Symmetriebrechung sind die zentralen Phänomene der starken Wechselwirkung. Es ist bisher jedoch nicht gelungen, diese beiden Grundtatsachen auf überzeugende Weise theoretisch zu erklären. Insbesondere das Confinement–Problem kann nicht als gelöst betrachtet werden, obgleich verschiedenste Ansätze entwickelt worden sind. Weder dynamische chirale Symmetriebrechung noch Confinement können im Rahmen der Störungstheorie verstanden werden, weshalb es notwendig ist, nicht–störungstheoretische Methoden anzuwenden. Der Dyson–Schwinger Zugang erweist sich als geeignet, da mit dieser Methode die fundamentalen Greens–Funktionen, die Gluon- und Quark–Propagatoren, zugänglich werden. Bisherige Studien unterstützen die Annahme, dass die Propagatoren sowohl dynamische chirale Symmetriebrechung als auch Confinement anzeigen.

Im ersten Kapitel wird der Elektron–Propagator in (2+1)–dimensionaler Quantenelektrodynamik (QED_3) im Rahmen des Dyson–Schwinger Zugangs untersucht. Für zwei verschiedene Trunkierungen wird gezeigt, dass QED_3 eine Phase hat, in der die Elektronen 'confined' sind und die chirale Symmetrie spontan gebrochen ist. Aufgrund dieser Gemeinsamkeiten von QED_3 und Quantenchromodynamik (QCD) ist es sinnvoll, die analytische Struktur der Fermion–Propagatoren in beiden Theorien zu vergleichen. Die Ergebnisse für den Elektron–Propagator in der 'confined' Phase von QED_3 sind qualitativ verschieden von den entsprechenden Ergebnissen in der 'unconfined' Phase. Dies kann als Argument dafür gewertet werden, dass der Propagator tatsächlich die Confinement–Signatur trägt.

Im Hauptteil wird das gekoppelte System von Dyson–Schwinger Gleichungen für die Gluon-, Quark- und Geist–Propagatoren der QCD in Landau–Eichung untersucht. Die Lösungen werden für $0 \leq N_f \leq 6$ und für verschiedene Quark–Massen diskutiert. Die Ergebnisse zeigen, dass die chirale Symmetrie gebrochen und dass die Gluonen aufgrund von Positivitäts–Verletzungen 'confined' sind. Für den Quark–Propagator konnte keinerlei Positivitäts–Verletzung nachgewiesen werden, jedoch sind die Ergebnisse qualitativ sehr ähnlich zu den Ergebnissen für den Elektron–Propagator in der 'confined' Phase von QED_3. Die Ergebnisse zeigen weiterhin, dass für alle $0 \leq N_f \leq 6$ der Gluon–Propagator für kleine Impulse gegen 0 geht, während der Geist–Propagator divergiert. Dieses Infrarotverhalten der Propagatoren impliziert, dass die laufende Kopplung α_s für alle $0 \leq N_f \leq 6$ einen Infrarot–Fixpunkt bei $\alpha_s \approx 9.5$ hat.

Im letzten Kapitel wird gezeigt, dass Meson–Produktionsprozesse genutzt werden können, um die qualitativen Eigenschaften des Quark–Propagators bei zeitartigen Impulsen zu untersuchen. Dies ergänzt die Dyson–Schwinger Studien, die im Euklidischen formuliert sind und somit nichts über die Eigenschaften der Propagatoren für zeitartige Impulse aussagen. Kaon Photoproduktion wird sich als besonders geeignet erweisen und im Rahmen des kovarianten Diquark–Quark Modells untersucht werden. Hierbei werden verschiedene Möglichkeiten verglichen, wie Confinement auf der Ebene der Propagatoren realisiert sein könnte. Die Ergebnisse für die Wirkungsquerschnitte zeigen, dass ein realistischer Quark–Propagator für zeitartige Impulse nicht ansteigen kann. Dies schliesst insbesondere ein, dass exponentielle Propagatoren keine gültige Näherung des Quark–Propagators sind.

Contents

1 Introduction **3**

2 Quantum Electrodynamics in 2+1 Dimensions **6**
2.1 Basic Concepts of QED_3 7
2.2 Dyson-Schwinger Equations for QED_3 10
2.3 Non–Perturbative Fermion-Photon Vertex 11
2.4 Dyson-Schwinger Equations: Bare Vertex Approximation 15
2.5 Dyson-Schwinger Equations: Ball-Chiu Vertex 20

3 Basic Concepts of QCD **24**
3.1 The QCD Lagrangian 24
3.2 Symmetries of the QCD Lagrangian 25
3.3 Asymptotic Freedom and Running Coupling 27
3.4 Confinement 28
3.5 A Note on Euclidean Quantum Field Theory 30

4 DSEs for Gluons and Ghosts **32**
4.1 DSEs of Landau Gauge QCD 32
4.2 Subtraction Scheme 37
4.3 Nonperturbative Running Coupling and Renormalization 41
4.4 Leading Order Infrared Analysis 43
4.5 Scale Invariant Representation 46

5 Dynamical Quarks **50**
5.1 The Quark Dyson-Schwinger Equation 50
5.2 Quark-Loop Contribution to the Gluon DSE 53
5.3 Infrared Behaviour of the Quark Loop 56
5.4 Renormalization of the Quark Loop 58

6 Results for Gluons, Ghosts and Quarks **63**
6.1 Accuracy of the Approach 63
6.2 Quenched Approximation 71
6.3 Dynamical Quarks 72
6.4 Comparison to Lattice Results 79

6.5 Positivity 80

7 Phenomenological Constraints on the Quark Propagator 85
7.1 Brief Review of the Diquark-Quark Model 86
7.2 Confining Model Propagators 93
7.3 Kinematical Particularities of Production Processes 95
7.4 Results for Kaon Photoproduction 97

8 Conclusions and Outlook 104

A Dyson-Schwinger Equations: Numerical Methods 108
A.1 Dyson-Schwinger Equations for QED_3 108
A.2 Chebyshev Approximation 111
A.3 Dyson-Schwinger Equations for QCD 113

B Technicalities 116
B.1 Symmetries of the Mass Terms in QED_3 116
B.2 Angle Integrals 117
B.3 Kaon Photoproduction $p\gamma \to \Lambda K$ 118

Chapter 1

Introduction

Particle physics aims at an understanding of the basic phenomena that constitute the material world at the most fundamental level. The main method of experimental investigation are scattering experiments. These have been much refined and extended since the early days and led to the discovery of nuclei, hadrons and finally quarks. These basic entities and their interactions are theoretically described within the framework of local gauge theories. The developments that led to this now accepted theoretical framework are shortly summarised in the following.

Starting with the use of accelerators and colliders the number of known elementary particles increased very rapidly. This astounding diversity was in glaring contrast to the small number of different particles that were known in the first quarter of the twentieth century. The large number and apparant similarity of those new particles suggested that they all consist of other more fundamental constituents. This hypothesis then lead to the proposition of the *quark model* [Ne'61], [GM62], [GMN64] which classified and ordered the then known 'zoo' of hadrons in a satisfying way.

However, the thus introduced fundamental degrees of freedom, the *quarks*, have never been observed as free particles albeit they very successfully describe the diversity of hadronic states. This suggested that there must be a very strong interaction between quarks at large distances which prevents the hadrons from breaking up into their constituents. The phenomenon that quarks occur only as constituents of hadrons gave rise to the notion of *confinement*.

The conclusion that the interaction between quarks must be very strong in order to prevent the hadron from breaking up into its constituents was then found to be in apparent disagreement with the electron–nucleon scattering results obtained at the SLAC [S^+75]. These results clearly indicated that the nucleon is made up of point–like constituents. However, the results also implied that these constituents are essentially non–interacting inside the nucleon. This lead to the conclusion that the coupling strength of quarks is large for large distances but becomes small at small distances, e.g. for the case that the quarks are confined within a nucleon where they are very close to each other. The fact that the coupling strength vanishes for small distances has been called *asymptotic freedom*.

Up to 1972 there were a variety of quark models and parton models which all explained

some of the experimental data. But none of these models has been considered to be a fundamental theory which should (in principle) be able to explain all the experimental results. This changed in 1973 when it was discovered [GW73], [Pol73] that non–Abelian gauge theories comprise asymptotic freedom, i.e. they do have the property that the coupling strength becomes small at small distances. Non–Abelian gauge theories had been investigated since the pioneering work of Yang and Mills [YM54]. But only after one had realised that these non-Abelian gauge theories comprise asymptotic freedom various lines of research converged to the formulation of *Quantum Chromodynamics* (QCD) [FGML73], [Wei73]. QCD has been developed on the basis of the quark model, however, it is different with regard to the internal colour degree of freedom. This quantum number had to be introduced in order to consistently describe the Δ^{++} resonance, it is the charge of the strong interaction. Essentially, QCD emerges if the gauge principle is applied to this internal colour degree of freedom. This then introduces *gluons* which are the gauge bosons of the strong interaction.

The masses of the light quark flavours are small if compared to typical hadronic scales and therefore they can be neglected in a first approximation. In this approximation and if only the light quark flavours are considered the Lagrangian of QCD becomes invariant under chiral transformations. However, as has been realised first in [Nam60], [Gol61] the vacuum may have a smaller symmetry than the action thus leading to spontaneous breaking of the corresponding symmetry. This idea could be readily applied to QCD and the pseudoscalar mesons could thus be identified as the Goldstone bosons of the *spontaneously broken chiral symmetry*.

During the first years QCD has been investigated using mainly perturbative techniques which can be applied for large momenta where the coupling constant is small. These calculations gave credibility and confidence to the hypothesis that QCD actually *is* the correct theory of the strong interactions. However, the most basic phenomena of QCD, i.e. confinement and spontaneous chiral symmetry breaking cannot be described using perturbative methods since the coupling strength at the relevant scale is large. This then lead to the development of a great variety of non–perturbative methods. Among these are e.g. lattice simulations [Wil74] and Dyson–Schwinger studies [Dys49], [Sch51].

Dyson–Schwinger equations (DSEs) form an infinite system of coupled equations for the Greens functions, i.e. for the transition amplitudes of a quantum field. The ensemble of these Greens functions is one of several possible hierarchies of functions which map the content of a local quantum field theory to an infinite set of functions [Haa96] and an exact solution to the DSEs does in principle contain all possible information on the corresponding field theory. However, in order to render the solution of the system of DSEs feasible it is necessary to truncate the infinite system of DSEs to a finite subsystem of equations. This truncated system of DSEs can then be solved and one thus obtains the most basic Greens functions: the propagators of gluons and quarks.

The main objective of the present work is the investigation of the coupled system of DSEs for Landau gauge QCD within a truncation scheme that preserves the basic symmetries of the theory. Whilst there can be little doubt that the propagators do contain the signature as well as the quantitative information on dynamical chiral symmetry breaking it is still an open question whether confinement is equally apparent in the propagators. The investigation [vSHA98] could answer this question for the gluons in the affirmative while

the corresponding studies for the quark propagator are the focus of the present investigation.

Three different approaches are pursued in the following and their relation is examined: First the propagators of electrons and photons in (2+1) dimensional Quantum Electrodynamics (QED_3) are investigated. This is suggestive because QED_3 is known to have a phase where the electrons are confined. This allows to study the confinement phenomenon within the DSE approach for a theory that is formally much simpler than QCD. Following this the propagators of gluons, ghosts and quarks in Landau gauge QCD are examined. Here, special emphasis is put on the quark DSE and on the quark–loop contribution to the gluon DSE. The results will be discussed for different numbers of quark flavours as well as for various current quark masses. Finally it is investigated whether meson production processes can give phenomenological constraints on the quark propagator. The calculations are performed within the covariant diquark–quark model and give qualitative constraints on the quark propagator in the time–like region.

Chapter 2

Quantum Electrodynamics in 2+1 Dimensions

In this chapter Quantum Electrodynamics in two space- and one time dimension will be investigated. This theory is usually called QED_3 and it is interesting because of various reasons. One has argued that QED_3 has a very close resemblance to the models that are investigated in order to understand high-T_c superconductors. Aside from this there are various other applications in condensed matter physics, e.g. studies of the fractional quantum Hall effect. For these applications of QED_3 the reader is referred to [CSM98]. However, this line of research is not what the present work is concerned with. While being defined for 2+1 dimensions, QED_3 is very similar to Quantum Chromodynamics (QCD) in 3+1 dimensions (i.e. QED_3 is very different from QED in 3+1 dimensions). This is because QED_3 is known to have a phase where the initial chiral symmetry of the theory is spontaneously broken and it is also known that the fermions are confined in this phase. These are the basic reasons why QED_3 is regarded a very interesting model theory: studying QED_3 it might be possible to investigate chiral symmetry breaking and confinement within a theory which is structurally much simpler than QCD while sharing the same basic phenomena.

In order to put the present work into context it is appropriate to give a (very) short guide to the literature: QED_3 has been investigated starting with the pioneering work of Cornwall [Cor80], Pisarski [Pis84] and Appelquist et al. [ABKW86]. These studies emphasize the similarity of QED_3 and QCD and especially investigate the formal structure of QED_3 as well as chiral symmetry breaking. In [ABKW86] the Dyson-Schwinger formalism is used in combination with a $1/N$-expansion for the polarization. This $1/N$-expansion approach has been extended by Nash [Nas89] and further investigated by Curtis et al. [CPW92]. The Dyson-Schwinger approach has been further developed by Burden et al. [BPR92] and especially by Maris [Mar93], [Mar95] and [Mar96]. The work [Mar95] focuses on confinement in QED_3 and relates this to the analytic structure of the fermion propagator. The analytic structure and the infrared behaviour of the fermion propagator is examined (using the Landau-Khalatnikov transformation) by Aitchison et al. [AACKK$^+$96], [AMM97], by Burden et al. [BT98] and recently by Bashir [Bas00]. An effective action approach is pursued by Gusynin et al. [GMS98], by Campbell-Smith [CS98], by Hott et al. [HM99] and

by Gies et al. [Gie99], [DG00]. Finally, the research on QED$_3$ is reviewed by Roberts and Williams [RW94] and most recently by Alkofer and v. Smekal [AvS00].

The investigation of chiral symmetry breaking and of the analytic structure of the quark propagator in QED$_3$ is the focus of the following sections. First some of basic concepts of QED$_3$ will be recalled. Following this the DSEs are introduced. These equations make reference to the full photon-electron vertex of QED$_3$ and are therefore (at this stage) not a closed system of equations. The truncation scheme that is used and especially the corresponding vertex ansatz are discussed and 2 different truncations are compared. The results for the electron- and photon propagators and the investigation of the phase structure of QED$_3$ close this chapter.

2.1 Basic Concepts of QED$_3$

This section briefly recalls some of the basic concepts and ideas that constitute the formal structure of QED$_3$. The discussion builds on the investigations [Cor80], [Pis84] and [ABKW86] where the basic theoretical framework of QED$_3$ has been uncovered. An introduction to this basic formalism can also be found in [Gie99].

The Lagrangian of massless QED$_3$ is

$$L = \bar{\Psi} i \not{D} \Psi - \frac{1}{4} F^{\mu\nu} F_{\mu\nu} \tag{2.1}$$

with the covariant derivative $D_\mu = \partial_\mu + ieA_\mu$. In this notation Ψ is a four component Dirac spinor which includes an index for N fermion flavours. The coupling constant e has dimension mass$^{1/2}$ which implies that any dynamically generated mass scale will be a pure number times e^2. There are no infinite renormalizations of the bare Lagrangian.

In 3 dimensions one could use two-component spinors and a 2×2 representation of the Dirac algebra $\{\gamma_\mu, \gamma_\nu\} = 2\delta_{\mu\nu}$ using e.g. $\gamma^0 = \sigma_2, \gamma^1 = i\sigma_3$ and $\gamma^2 = i\sigma_1$. However, there is no other 2×2 matrix that anti-commutes with all these γ^μ. This implies that there is no generator of a chiral symmetry that could be broken by a mass term of the form $m\bar{\psi}\psi$, where ψ is a two component spinor. That is, in the 2×2 representation the massless theory has no more symmetry than the massive theory since there is *no notion* of chiral symmetry in this case.

Therefore it is more interesting to take Ψ to be a four component spinor which is constructed from two two-component spinors ψ_1 and ψ_2 in the way

$$\Psi = \begin{pmatrix} \psi_1 \\ \psi_2 \end{pmatrix} \tag{2.2}$$

and to take correspondingly a 4×4 representation of the Dirac algebra, e.g.

$$\gamma^0 = \begin{pmatrix} \sigma_3 & 0 \\ 0 & -\sigma_3 \end{pmatrix} \quad , \quad \gamma^1 = i \begin{pmatrix} \sigma_1 & 0 \\ 0 & -\sigma_1 \end{pmatrix} \quad \text{and} \quad \gamma^2 = i \begin{pmatrix} \sigma_2 & 0 \\ 0 & -\sigma_2 \end{pmatrix} . \tag{2.3}$$

However, there are now two 4×4 matrices

$$\gamma^3 = i \begin{pmatrix} 0 & \mathbb{1} \\ \mathbb{1} & 0 \end{pmatrix} \quad \text{and} \quad \gamma^5 = i \begin{pmatrix} 0 & \mathbb{1} \\ -\mathbb{1} & 0 \end{pmatrix} \tag{2.4}$$

which anti-commute with γ^0, γ^1 and γ^2. Therefore the Lagrangian (2.1) which corresponds to the massless theory is invariant under each of the transformations

$$\Psi \to exp(i\alpha\gamma^3)\Psi \quad \text{and} \tag{2.5}$$

$$\Psi \to exp(i\beta\gamma^5)\Psi \, . \tag{2.6}$$

For each four-component spinor there is a global $U(2)$ symmetry which is generated by

$$\mathbb{1}, \gamma^3, \gamma^5, [\gamma^3, \gamma^5] \tag{2.7}$$

and the full symmetry of (2.1) therefore is $U(2N)$. A mass term of the usual form (whether it be explicit or due to spontaneous symmetry breaking)

$$m\bar{\Psi}\Psi \tag{2.8}$$

would break this symmetry to the subgroup

$$SU(N)_{(1+[\gamma^3,\gamma^5])} \times SU(N)_{(1-[\gamma^3,\gamma^5])} \times U(1)_{[\gamma^3,\gamma^5]} \times U(1)_{\mathbb{1}} \tag{2.9}$$

which would imply the emergence of $(2N)^2 - 2N^2 = 2N^2$ Goldstone bosons in the case that the symmetry has been broken spontaneously. There would be N^2 Goldstone bosons due to the breaking of the γ^3 symmetry, which would couple to $\bar{\Psi}\gamma^3\gamma^\mu\Psi$ and the same number of Goldstone bosons due to the breaking of the γ^5 symmetry, which would couple to $\bar{\Psi}\gamma^5\gamma^\mu\Psi$.

However, there is another option, the mass term could also be of the form

$$m\bar{\Psi}\frac{1}{2}[\gamma^3, \gamma^5]\Psi \, . \tag{2.10}$$

Comparing the two alternatives (2.8) and (2.10) for the mass term, one finds that they are quite different. The 'normal' mass term (2.8) breaks chiral symmetry but is parity conserving, whereas the mass term (2.10) is invariant under the chiral transformations (2.5) and (2.6) but it is not invariant under parity transformations. (See section B.1 for a detailed discussion.)

In [BR91] the potential that corresponds to the non–perturbative polarization scalar Π is derived. The authors obtain for the potential V at large distances r:

$$V(\vec{r}) = -e^2 \int \frac{d^2k}{(2\pi)^2} exp(i\langle k, r\rangle) \frac{1}{k^2} \frac{1}{1 + \Pi(k^2)} \, , \tag{2.11}$$

$$V(\vec{r}) = V(r) = \frac{e^2}{2\pi} \frac{1}{1 + \Pi(0)} \ln(e^2 r) + const. + \mathcal{O}\left(\frac{1}{r}\right) \, . \tag{2.12}$$

This demonstrates that the potential at large distances r is dominated by a logarithmic term given that $\Pi(0)$ is finite. I.e. QED_3 has logarithmic confinement if the polarization scalar becomes constant in the infrared which will be shown to be true in the confined phase, see sections 2.4 and 2.5. This link between the infrared behaviour of the polarization and

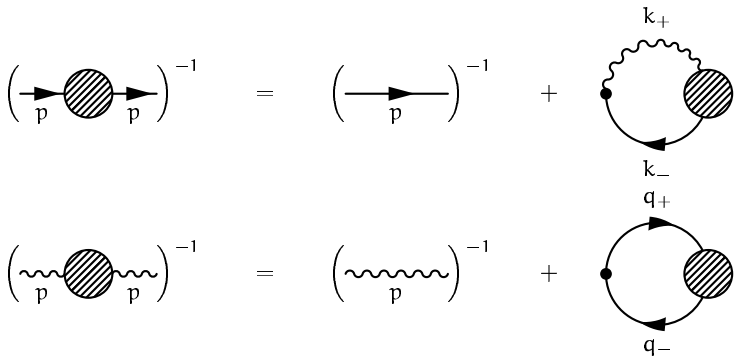

Figure 2.1: Diagrammatical representation of the coupled system of DSEs for the fermion- and photon propagator in QED$_3$

the potential V is illustrated in the subsequent sections where the numerical results are discussed.

It is interesting to note that in QED$_3$ it is possible to introduce a mass term for the gauge field without spoiling gauge invariance. To make this more explicit we add the term

$$\frac{\mu}{2}\epsilon^{\mu\nu\sigma}F_{\mu\nu}A_\sigma \tag{2.13}$$

to the Lagrangian (2.1) and derive the Euler-Lagrange equations of motion. For each fermion flavour k separately these equations read

$$\partial_\sigma F^{\sigma\mu} + \mu\epsilon^{\mu\rho\sigma}F_{\rho\sigma} = e\bar{\Psi}_k\gamma^\mu\Psi_k \ , \tag{2.14}$$

$$\left[\not{D} - m\right]\Psi_k = 0 \ . \tag{2.15}$$

These equations are invariant under the gauge transformation

$$A_\mu \to A_\mu + \partial_\mu\Lambda \quad , \quad \Psi \to exp(ie\Lambda)\Psi \ . \tag{2.16}$$

I.e. in QED$_3$ it is possible to have a *normal* mass term for the gauge field without breaking gauge invariance[1].

2.2 Dyson-Schwinger Equations for QED$_3$

The coupled system of DSEs for the propagators of the fermion and the photon are given by

$$S^{-1}(p) = S_0^{-1}(p) - ie^2 \int \frac{d^3k}{(2\pi)^3} D_{\mu\nu}(k_+)\Gamma_\mu(k_+, k_-)S(k_-)\gamma_\nu \,, \tag{2.17}$$

$$D_{\mu\nu}^{-1}(p) = g_{\mu\nu}p^2 - p_\mu p_\nu \left(1 - \frac{1}{\xi}\right) + \Pi_{\mu\nu}(p) \quad \text{and} \tag{2.18}$$

$$\Pi_{\mu\nu}(p) = ie^2 \int \frac{d^3k}{(2\pi)^3} tr\Big(\gamma_\mu S(q_+)\Gamma_\nu(q_+, q_-)S(q_-)\Big) \,. \tag{2.19}$$

Hereby the (Minkowski) momenta k_+, k_-, q_+, q_- are constrained by momentum conservation

$$k_+ = \eta p + k \,, \tag{2.20}$$

$$k_- = (1-\eta)p - k \tag{2.21}$$

and correspondingly for q_+, q_- with $\eta \in [0, 1]$. The most common choices are the asymmetric momentum routing: $\eta = 0$ and the symmetric momentum routing: $\eta = 1/2$.

For the numerical solution it is advantageous to first transform the system of equations (2.17), (2.18) and (2.19) to a more suitable form. To this end we use the most general form of the fermion propagator (for Euclidean momenta)

$$S^{-1}(p) = -i\not{p}A(p) + B(p) \tag{2.22}$$

which defines the scalar functions A and B usually called the vectorial and the scalar self-energy. An equivalent and often used form is

$$S(p) = -i\not{p}\sigma_v(p^2) + \sigma_s(p^2) \tag{2.23}$$

where the two scalar functions σ_v and σ_s are related to A and B according to:

$$\sigma_v(p^2) = \frac{A(p^2)}{p^2A^2(p^2) + B^2(p^2)} \qquad \text{and} \qquad \sigma_s(p^2) = \frac{B(p^2)}{p^2A^2(p^2) + B^2(p^2)} \,. \tag{2.24}$$

The photon propagator reads

$$D_{\mu\nu}(q) = \left(\delta_{\mu\nu} - \frac{q_\mu q_\nu}{q^2}\right)\frac{1}{q^2(1+\Pi(q))} + \xi\frac{q_\mu q_\nu}{q^4} \tag{2.25}$$

where $\xi = 0$ (Landau gauge) is used in the following. The polarization scalar Π is defined via the relation

$$\Pi_{\mu\nu}(p) = (\delta_{\mu\nu}p^2 - p_\mu p_\nu)\Pi(p) \tag{2.26}$$

[1]The Lagrangian changes only by a total derivative under gauge transformations, which leaves the action unchanged.

However, this equation is ambiguous as it stands since equation (2.19) has to be regularized. The divergent part of (2.19) turns out to be proportional to $\delta_{\mu\nu}$. Therefore it has been proposed [BPR92] to apply the projector

$$\delta^{\mu\nu}p^2 - 3p^\mu p^\nu \tag{2.27}$$

to both sides of (2.26). This projects out the divergent part of $\Pi_{\mu\nu}$ and gives

$$\Pi(p) = \frac{1}{2p^2}\left(\delta^{\mu\nu} - 3\frac{p^\mu p^\nu}{p^2}\right)\Pi_{\mu\nu}(p) \tag{2.28}$$

which is finite and thus well defined.

Using the definitions (2.22) and (2.28) and applying appropriate traces to (2.17), (2.18) and (2.19) one arrives at a coupled system of equations for the self-energies of the fermion A, B and the polarization scalar Π. For two different approximations these equations are given explicitely in sections 2.4 and 2.5.

2.3 Non–Perturbative Fermion-Photon Vertex

This section centers on the fermion-photon vertex and especially the ansatz that has been developed by Ball and Chiu [BC80a], [BC80b] and extended by Curtis and Pennington [CP90] will be examined.

The DSEs (2.17), (2.18) and (2.19) do not form a closed system of equations. This is because they necessarily depend on the full fermion-photon vertex Γ_μ. This vertex is the solution of its own DSE which in turn depends on even higher order Green's function. This infinite hierarchy of DSEs (the first levels thereof have been indicated) cannot be solved as it is. In order to render a solution feasible a certain truncation scheme has to be applied. The common approach is to construct the vertex functions instead of solving the corresponding DSE. This then leads to a closed system of equations for the propagators, however, it cannot avoid the drawback of introducing truncations. The vertex construction rests on the basic symmetries of the theory: the discrete symmetries and especially the gauge symmetry as expressed by the Ward-Takahashi identity (WTI). This identity determines the longitudinal part of the vertex but it leaves the transversal part unconstrained. The transversal part has to be constrained using other conditions like multiplicative renormalizability, however, it is not possible to completely determine the transverse part. In the following the construction of the vertex, following [BC80a], [BC80b] and [CP90] is shortly summarized.

The WTI

$$q^\mu\Gamma_\mu(k,p) = S^{-1}(k) - S^{-1}(p) \tag{2.29}$$

with $q = k - p$ relates the full fermion-photon vertex Γ_μ and the full fermion propagator S. The most general solution to this WTI can be written in the form

$$\Gamma_\mu(k,p) = \Gamma^T_\mu(k,p) + \frac{q_\mu}{q^2}\left(S^{-1}(k) - S^{-1}(p)\right) \tag{2.30}$$

where Γ^T_μ denotes the purely transverse part of the vertex that satisfies $q^\mu\Gamma^T_\mu(k,p) = 0$. I.e. the solution of (2.29) completely determines the longitudinal part, however, it does not constrain the transverse part in any way. It turns out to be more useful to start out with the differential form of the WTI (2.29):

$$\frac{\partial S^{-1}(p)}{\partial p_\mu} = \Gamma^\mu(p,p)\ . \tag{2.31}$$

This can be solved and gives the $(k = p)$-limit of the full vertex Γ_μ. The most natural procedure is then to extend this vertex to the case that $k \neq p$ in a k,p-symmetric way that also solves (2.29). This k,p-symmetric extension of the solution to (2.31) (which solves (2.29) and (2.31)) then reads:

$$\Gamma^L_\mu(k,p) = \frac{1}{2}\big(A(k^2) + A(p^2)\big)\gamma_\mu + \frac{1}{2}\Delta A(k,p)(k+p)_\mu(\not{k} + \not{p}) \\ - \Delta B(k,p)(k+p)_\mu \tag{2.32}$$

where the two auxiliary functions ΔA and ΔB are defined according to

$$\Delta A(k,p) = \frac{A(k^2) - A(p^2)}{k^2 - p^2} \qquad \Delta B(k,p) = \frac{B(k^2) - B(p^2)}{k^2 - p^2} \tag{2.33}$$

To this solution for the longitudinal part any transversal part Γ^T_μ satisfying

$$q^\mu\Gamma^T_\mu(k,p) = 0 \qquad \text{and} \qquad \Gamma^T_\mu(p,p) = 0 \tag{2.34}$$

can be added without affecting the WTI (2.29) and its differential form (2.31). The most general form of the transverse part can be decomposed into eight tensors $T_{j\mu}$ according to

$$\Gamma^T_\mu(k,p) = \sum_{j=1}^{8} \tau_j(k^2, p^2, q^2)T_{j\mu}(k,p) \tag{2.35}$$

which are multiplied by a corresponding number of coefficient functions τ_j (see [CP90] for the definition of the tensors $T_{j\mu}$). The full fermion-photon vertex should especially allow to multiplicatively renormalize the fermion DSE according to

$$S_R(p,\mu) = Z_2^{-1}S_0(p,\Lambda) \tag{2.36}$$

which relates the bare propagator S_0 to the renormalized propagator S_R. As first noted by King [Kin83], further investigated Brown et al. [BD89] and used by Curtis et al. [CP90]: multiplicative renormalizability is a highly nontrivial constraint when applied to the transverse part of the vertex. And especially a vertex with $\Gamma^T_\mu = 0$ does in principle not allow for multiplicative renormalization of the fermion DSE. Using the leading-logarithm approximation for the perturbative limit of the fermion self-energy A Curtis et al. [CP90] proposed the ansatz

$$\Gamma^T_\mu(k,p) = \frac{1}{2}\big(A(k^2) - A(p^2)\big)\Omega(k,p)T_{6\mu}(k,p) \tag{2.37}$$

with

$$T_{6\mu}(k,p) = \gamma_\mu(k^2 - p^2) - (k+p)_\mu(\not{k} - \not{p}) \tag{2.38}$$

$$\Omega(k,p) = \frac{k^2 + p^2}{\left(k^2 - p^2\right)^2 + \left(M^2(k^2) + M^2(p^2)\right)^2} \tag{2.39}$$

where the definition of the mass function $M = B/A$ has been used.

The full vertex (ansatz) is the sum of the longitudinal part and the transverse part

$$\Gamma_\mu(k,p) = \Gamma^L_\mu(k,p) + \Gamma^T_\mu(k,p) \tag{2.40}$$

where the longitudinal part Γ^L and the transverse part Γ^T are defined in (2.32) and (2.37), respectively. The vertex (2.40) solves the WTI (2.29) and guarantees multiplicative renormalizability of the fermion DSE. A growing number of Dyson-Schwinger studies rely on this vertex ansatz, see e.g. [AvS00] and references therein.

Dong et al. [DMR94] argue that there is a problem with the ansatz (2.37) for the transverse part that has been proposed by Curtis et al. [CP90]. In the chirally symmetric phase the mass function M vanishes. This allows to simplify the ansatz (2.37) and one obtains

$$\Omega(k,p)T_{6\mu}(k,p) = \frac{k^2 + p^2}{\left(k^2 - p^2\right)^2}\left[\gamma_\mu(k^2 - p^2) - (k+p)_\mu(\not{k} - \not{p})\right] \tag{2.41}$$

which becomes singular in the limit that $k \to p$. The authors in [DMR94] argue that this formal singularity leads to a kinematic singularity in the full vertex, including the Curtis-Pennington ansatz for the transversal part. This would be an unwanted feature because absence of kinematic singularities was one of the constraints that were used in the construction. However, the term $\Omega T_{6\mu}$ is always multiplied by $(A(k^2) - A(p^2))$ which should be sufficient to cancel the formal divergence in $\Omega T_{6\mu}$ such that the vertex is free of kinematical singularities. In a numerical approach this might well pose a technical problem even if it is none in principle.

The transverse part has been constructed using the fermion DSE and the Ward-Takahashi identity. However, if the coupled system of DSEs (2.17), (2.18) and (2.19) is to be solved than the full vertex enters the fermion equation (2.17) but also in the photon equation (2.19). As has been mentioned already: In order to solve the system of DSEs it is advantageous to first transform the DSE for the quark propagator S into a system of two coupled equations for the scalar functions A and B which are defined in (2.22). The DSE for A can then be written (in a symbolic way) as $A(p^2) = 1 + \Sigma_A\left[p^2, \Gamma\right]$ which defines the self–energy contribution Σ_A which is used below. Here the dependence on the vertex Γ has been made explicit for later convenience.

While being consistent with the fermion DSE it turns out that the Curtis-Pennington ansatz (2.37) does not lead to stable results that could be physically interpreted if it is used in the photon equation (2.19). In order to facilitate the following discussion it is advantageous to first introduce some notation. The longitudinal part of the full vertex is given in (2.32) and the first of the three terms reduces to the bare vertex in the perturbative limit. This term

will be denoted by Γ^I:

$$\Gamma^I_\mu(k,p) = \frac{1}{2}\big(A(k^2) + A(p^2)\big)\gamma_\mu \tag{2.42}$$

The definition of the transverse part Γ^T is given in (2.37). In the following the infrared limit of the vectorial self-energy A and of the polarization scalar Π will be examined. Hereby the contribution of the large loop momenta to this infrared limit is the primary concern. The following discussion is restricted to the DSEs for A and Π. For both equations two cases are considered: first the full vertex Γ is set equal to Γ^I as defined in (2.42) and second the full vertex Γ is set equal to Γ^T as defined in (2.37). For both vertex ansätze the UV–contribution to the IR limit of A and Π is examined. Neither the other contributions to the longitudinal part (2.32) of the vertex nor the corresponding considerations for the DSE for B alter the conclusion that will be drawn in the following.

The DSE for the vectorial self-energy A and for the full vertex (2.40) is given in section (2.5). Using this equation one can derive the UV contribution (large loop momenta) to the infrared limit ($p^2 \to 0$) if the vertex Γ in the DSE for A is set equal to Γ^I or to Γ^T. The results are

$$\Sigma_A \propto \int dk\, \big(A(k^2) + A(p^2)\big)\frac{d}{dk^2}\frac{1}{1+\Pi(k^2)} \quad \text{for} \quad \Gamma = \Gamma^I\,, \tag{2.43}$$

$$\Sigma_A \propto p\int dk\, \frac{1}{k^3}\frac{1}{1+\Pi(k^2)} \quad \text{for} \quad \Gamma = \Gamma^T\,. \tag{2.44}$$

Obviously the infrared limit of Σ_A is dominated by the (Γ^I)-contribution to the full vertex. The (Γ^T)-contribution is strongly suppressed due to the additional $1/k^3$ factor and it is vanishing in the infrared limit $p^2 \to 0$. This is contrasted by the results for the polarization scalar (2.19). For this case the results are:

$$\Pi \propto \int dk\, \sigma_v(k^2)\frac{k^4}{(k^2+M^2(k^2))^2} \quad \text{for} \quad \Gamma = \Gamma^I\,, \tag{2.45}$$

$$\Pi \propto \int dk\, \frac{k^4}{M^4(k^2)}\frac{dA(k^2)}{dk^2} \quad \text{for} \quad \Gamma = \Gamma^T \tag{2.46}$$

where the σ_v is defined in (2.24). The (Γ^I)-contribution gives a finite contribution to the infrared limit and in fact, looking more closely at the remaining contributions of the longitudinal vertex Γ^L it turns out that the (Γ^I)-contribution is the dominant one. The (Γ^T)-contribution puts very tight constraints on the behaviour of $A(k^2)$ for large k^2. This contribution appears to be divergent unless A becomes constant *very* rapidly for large k^2 which is apparently inconsistent with the fermion DSE. This is strongly supported by numerical studies which fail to find a stable solution if the transverse part (2.37) is included (for the polarization).

While these studies have been carried out within the context of QED_3 it appears that the problems with the transverse part (2.37) that have been discussed are much more general. It has been reported by Bloch [Blo01] that in QED_4 it is not possible to find a stable numerical

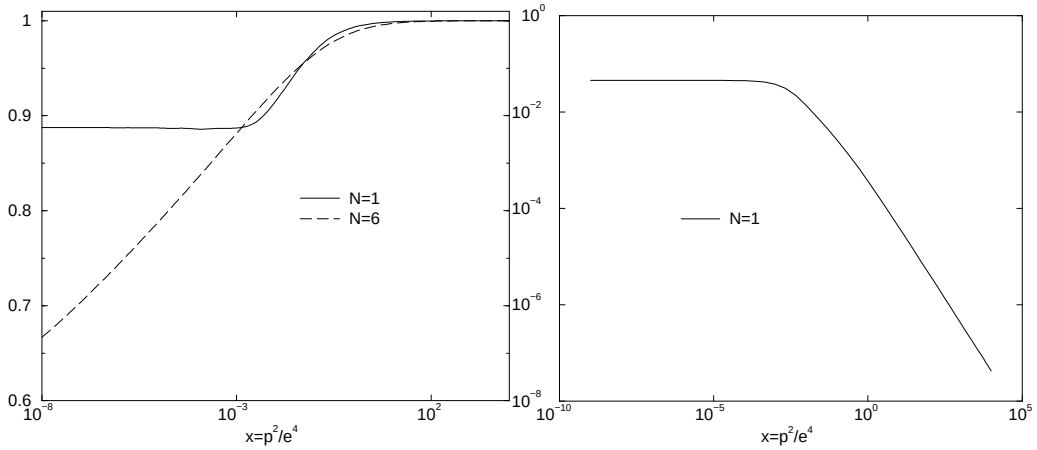

Figure 2.2: Results for the fermion propagator self-energies A and B which are defined in (2.22) for the bare vertex approximation, i.e. using the system of equations (2.47), (2.48) and (2.49). *Left panel:* Results for A for the two cases $N = 1$ and $N = 6$. *Right panel:* Results for B (in units of $e^2 = 1$) for $N = 1$. For $N = 6$ one finds that $B = 0$.

solution to the coupled system of DSEs if the CP contribution to the polarization is included (see also [Blo95]).

The construction of the longitudinal part of the vertex (2.40) uses only the Ward-Takahashi identity (2.29). The construction of the transverse part makes recourse to the fermion equation while ignoring the DSE for the photon propagator. It seems that the photon DSE encompasses some additional constraints that must not be ignored in the construction of the transverse part of the full vertex.

In the following, for the calculations for QED_3 as well as for the calculations for QCD the (Γ^T)-contribution to the polarization will be ignored.

2.4 Dyson-Schwinger Equations: Bare Vertex Approximation

In this section we investigate the coupled system of DSEs (2.17), (2.18) and (2.19) in the bare vertex approximation, i.e. using the ansatz $\Gamma_\nu(p,q) = \gamma_\nu$ for the fermion-photon vertex Γ_ν. This system of equations has been investigated by Maris [Mar95], [Mar96].

Starting with the DSEs for the fermion- and photon propagators, as defined in (2.17), (2.18) and (2.19) one derives a coupled system of equations for the self-energies A, B and the polarization scalar Π. This is achieved by applying appropriate combinations of traces

to (2.17), (2.18) and (2.19). For the case that $\Gamma_\nu(p,q) = \gamma_\nu$ the resulting equations are:

$$A(p) = 1 + \frac{2e^2}{p^2}\int \frac{d^3k}{(2\pi)^3}\sigma_\nu(k_-)\frac{\langle k_+, p\rangle\langle k_+, k_-\rangle}{k_+^2}\frac{1}{k_+^2(1+\Pi(k_+))} \tag{2.47}$$

$$B(p) = 2e^2\int \frac{d^3k}{(2\pi)^3}\sigma_s(k_-)\frac{1}{k_+^2(1+\Pi(k_+))} \tag{2.48}$$

$$\Pi(p) = 4N\frac{e^2}{p^2}\int \frac{d^3k}{(2\pi)^3}\left(\langle q_+, q_-\rangle - \frac{3}{p^2}\langle p, q_+\rangle\langle p, q_-\rangle\right)\sigma_\nu(k_+)\sigma_\nu(k_-) \tag{2.49}$$

where the definitions of σ_ν and σ_s are given in (2.24). The momenta are defined as indicated in fig. 2.2 and as specified in section 2.2. For the numerical analysis the asymmetric momentum routing (i.e. $\eta = 0$) is used.

The results for the fermion propagator that are obtained in the bare vertex approximation (i.e. using the DSEs (2.47), (2.48) and (2.49)) are shown in fig. 2.2. The left panel shows the results for the vectorial self-energy A for the two cases $N = 1$ and $N = 6$. For one fermion flavour $A(x)$ becomes constant at about 0.88 for $x \lesssim 10^{-3}$. This is in contrast to the infrared behaviour for $N = 6$; in this case A obviously has a power-like behaviour $A = bx^\beta$. Since the infrared behaviour of the vectorial self-energy is qualitatively (very) different for the two cases $N = 1$ and $N = 6$ that have been examined one could argue that the theory undergoes a phase transition at some $1 < N < 6$. This will be investigated later on in detail.

The corresponding results for the scalar self-energy B are shown in the right panel of fig. 2.2 in units of the coupling $e^2 = 1$. For $N = 1$ one obtains that $B(x)$ becomes constant at about 0.04 for $x \lesssim 10^{-4}$ whereas for $N = 6$ one finds a very small $B \leq 10^{-14}$ which does not become constant for small x. If these calculations are repeated with increases numerical effort then one finds that B becomes increasingly smaller for $N = 6$ whereas the results are completely stable for the case $N = 1$. This clearly demonstrates that for $N = 6$ one actually has $B = 0$.

The results for the polarization scalar Π that correspond to the results in fig. 2.2 are shown in fig. 2.3. The results for $N = 1$ and $N = 6$ are qualitatively different quite similar to the results that have been found for the vectorial self-energy A which are shown in the left panel of 2.2. For $N = 1$ one finds that the polarization scalar becomes constant at about $\Pi \approx 1.9$ for $x \lesssim 10^{-4}$ whereas for $N = 6$ Π is found to have a power–like behaviour (cf. fig. 2.3).

This qualitative difference in the behaviour of Π supports the assumption that has been mentioned already: the theory might undergo a phase transition somewhere between $N = 1$ and $N = 6$.

In order to investigate this supposed phase transition it is most instructive to look at the infrared limit of the fermion self-energies A, B and of the polarization scalar Π. The infrared limit of A and B is shown in fig. 2.4. The left panel shows the results for $A(0)$; one finds that $A(0)$ is exactly 1 for $N = 0$. $A(0)$ becomes smaller but remains finite for $0 < N \lesssim 3.2$. At $N \approx 3.2$ the shape of A changes: whereas A is constant in the infrared for $N < 3.2$ it has a power-like behaviour $A(x) \propto x^\beta$ for $N > 3.2$. These two cases are shown in the left panel of fig. 2.2 where the two exemplary cases $N = 1$ and $N = 6$ are

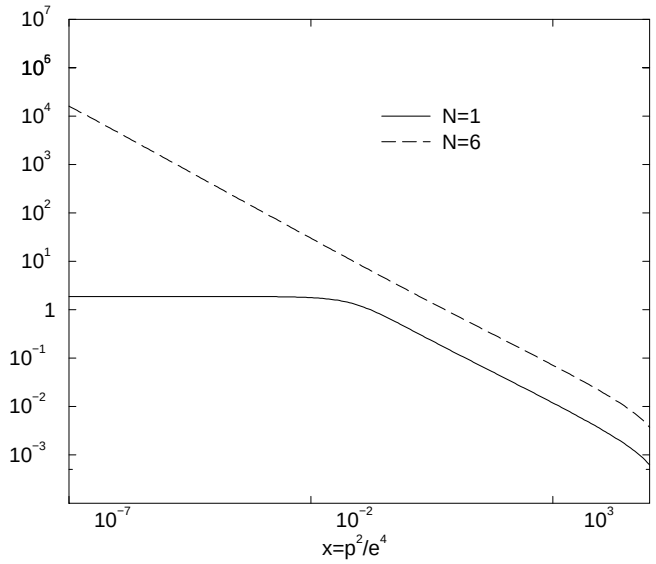

Figure 2.3: Results for the polarization scalar Π for $N = 1$ and $N = 6$ in the bare vertex approximation, i.e. using the system of equations (2.47), (2.48) and (2.49).

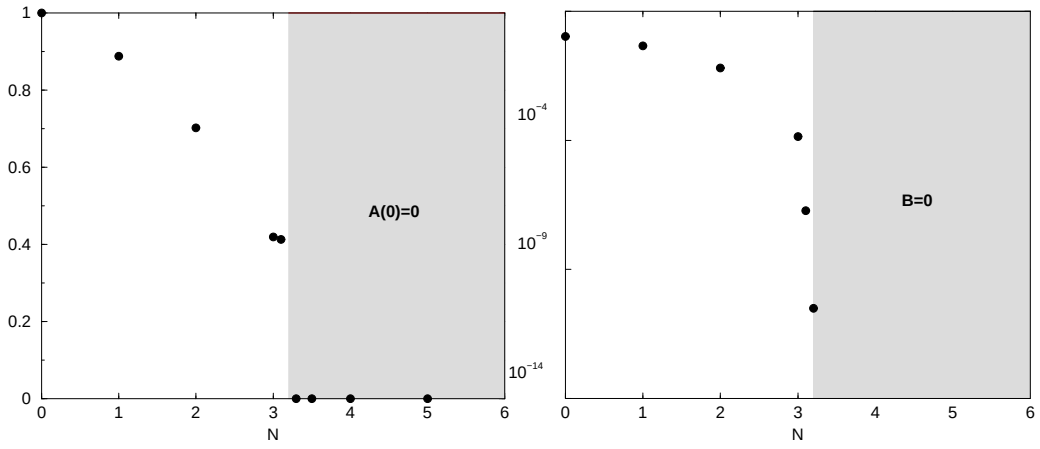

Figure 2.4: Results for infrared limit of A and B in the bare vertex approximation, i.e. using the system of equations (2.47), (2.48) and (2.49). *Left panel:* Results for the infrared limit $A(0)$ for $0 \leq N \leq 6$. For $N \gtrsim 3.2$ (i.e. within the shaded area) one finds that $A(0) = 0$. *Right panel:* Results for the infrared limit $B(0)$ (in units of $e^2 = 1$) for $0 \leq N \leq 6$.

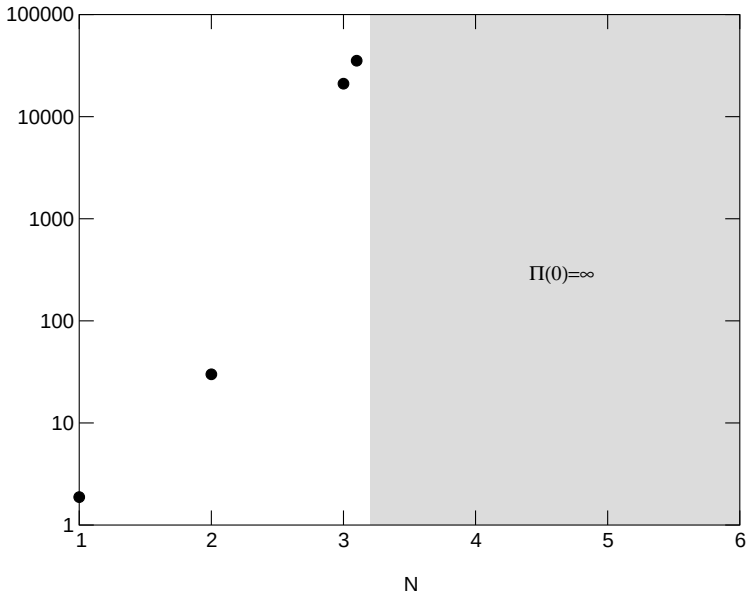

Figure 2.5: Results for the infrared limit of the polarization scalar Π for the bare vertex approximation, i.e. using the system of equations (2.47), (2.48) and (2.49). For $N = 0$ one of course finds that $\Pi = 0$.

compared which are representative for the two phases. For $N \lesssim 3.2$ one always finds that A becomes constant in the infrared as the $N = 1$ result that is shown in the left panel of 2.2. And for $N \gtrsim 3.2$ one always finds that A has the power-like behaviour as the $N = 6$ result that is shown in the left panel of fig. 2.2. The infrared behaviour of A for $N > 3.2$ especially implies that $A(0) = 0$ in this phase.

The infrared limit of B (in units of $e^2 = 1$) is shown in the right panel of fig. 2.4. This demonstrates even more explicitely that the theory undergoes a phase transition at $N \approx 3.2$. For $N = 0$ one finds that $B(0) \approx 0.105$. Then, for $N = 1, 2$ the value of $B(0)$ slowly decreases and drops below 10^{-12} at $N \approx 3.2$. For $N \gtrsim 3.2$ the value of $B(0)$ depends on the numerical effort that is used which has to be expected in this case. Increased numerical effort gives still smaller values for $B(0)$ for $N \gtrsim 3.2$ while the results for $N < 3.2$ are completely stable. This has to be interpreted in the way that for $N \gtrsim 3.2$ the infrared limit of B is 0 (i.e. $B = 0$ for all momenta). The infrared limit of B measures the extent to which the chiral symmetry is spontaneously broken, i.e. $B(0)$ is an order parameter. The results shown in fig. 2.4 imply that QED_3 has 2 phases: the first phase is realized for $N < 3.2$ and corresponds to the Nambu-Goldstone phase, i.e. chiral symmetry is spontaneously broken. The second phase is realized for $N > 3.2$ and it corresponds to the Wigner-Weyl phase, i.e. the original chiral symmetry remains unbroken.

The infrared limit of the polarization scalar Π is shown in fig. 2.5. Also this figure clearly demonstrates that the system undergoes a phase transition at $N \approx 3.2$. Whereas

$\Pi(0)$ steadily increases for $N \lesssim 3.2$ one finds that $\Pi(0)$ remains essentially constant for $N \gtrsim 3.2$. The two phases correspond to a different qualitative behaviour of Π in the infrared. Whereas for $N < 3.2$ one always finds that Π becomes constant in the infrared (as exemplified by the $(N = 1)$-result shown in fig. 2.3) one obtains that for $N > 3.2$ the polarization scalar Π has a power-like behaviour (as exemplified by the $(N = 6)$-result shown in fig. 2.3). The results in fig. 2.5 give the value of the polarization $\Pi(x)$ at very small but still finite x. However, taking into account that the polarization scalar Π for $N > 3.2$ has a power-like behaviour one has to conclude that in the infrared limit one has:

$$\Pi(x) \to \infty \qquad \text{for} \qquad x \to 0 \qquad (\text{for} \qquad N > 3.2) \tag{2.50}$$

whereas $\Pi(0)$ is finite for $N < 3.2$. The result (2.11) then implies that the phase transition at $N \approx 3.2$ is not only a phase transition between a chirally symmetric phase and a phase where the chiral symmetry is spontaneously broken. This phase transition also separates a phase where the potential (2.11) is logarithmically confining from a phase where the potential (2.11) becomes constant a large distances.

The infrared behaviour of A (in the bare vertex approximation) and for the chirally symmetric phase is known analytically. It has been first conjectured in [ABKW86] and has been derived analytically in [AMM97]. The authors give the explicit expression

$$A^{-1}(p) \to \exp\left(\frac{24}{5N\pi^2} - \frac{2}{N\pi}\right) \frac{2^\gamma \pi^{3/2} \gamma \Gamma(\gamma/2)}{4\pi\Gamma\left(\frac{3-\gamma}{2}\right)} \left(\frac{\alpha}{p}\right)^\gamma \tag{2.51}$$

for $p \to 0$ with $\gamma = 8/(3N\pi^2)$. For the following discussion the result (2.51) will be written in the form

$$b(N)\left(\frac{p^2}{e^4}\right)^{\beta(N)} \tag{2.52}$$

thus defining the coefficient b and the exponent β. The corresponding results for the coefficient $b(N)$ and the exponent $\beta(N)$ as calculated from (2.51) are compared in table 2.1 with the DSE results that have been discussed in this section. This comparison also illustrates the accuracy of the approach; the DSEs quite accurately yield the infrared behaviour of the propagator.

QED_3 has been investigated in order to study a theory which has the same basic phenomena as QCD (confinement and spontaneous chiral symmetry breaking) while being much simpler. It will be argued in section 3.2 and discussed more thoroughly in section 6.5 that there is convincing evidence that positivity is directly linked to confinement. Since the present results are to be compared to the corresponding results for QCD it is suggestive to examine whether the fermion propagator in QED_3 in the confined phase does violate positivity. These results are presented here mainly for later convenience and the reader is referred to section 6.5 for a discussion of the theoretical background. The standard positivity constraint refers to the spectral density that is defined in the Källen–Lehmann representation. In an Euclidean approach the positivity of this spectral density directly translates into

N	$b(N)$	$\beta(N)$	$b(N)_{bare}$	$\beta(N)_{bare}$	$b(N)_{BC}$	$\beta(N)_{BC}$
5	1.0069	0.02702	1.06668	0.02989	1.09975	0.02895
6	1.0059	0.02516	1.04505	0.02447	1.08163	0.02371
7	1.0050	0.01929	1.03146	0.02071	1.07401	0.02001
8	1.0044	0.01689	1.02233	0.01794	1.06769	0.01738
15	1.0024	0.00901	0.99976	0.00927	1.05098	0.00889

Table 2.1: Results for the infrared behaviour of A in the chirally symmetric phase. The analytic result (2.51) (columns 2 and 3) is compared to the DSE results for the bare vertex approximation (4. and 5. column) for the Ball–Chiu (BC) vertex ansatz (6. and 7. column).

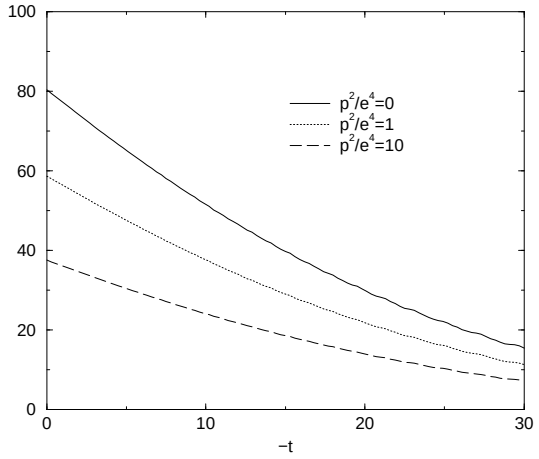

Figure 2.6: Results for the one–dimensional Fourier transform (2.53) of the quark propagator for three different values of $\vec{p}^2$.

Osterwalder–Schrader reflection positivity [OS73],[OS75], see section 3.5 where this will be discussed.

For the most basic Greens function, for the propagator, Osterwalder–Schrader reflection positivity can be written in the form (see section 6.5)

$$\int dp_0\, \sigma_v(p_0^2 + \vec{p}^2) exp(ip_0 t) \geq 0\ . \tag{2.53}$$

The results for this Fourier transform are shown in fig. 2.6 and it is obvious that they do not indicate any violation of Osterwalder–Schrader reflection positivity.

2.5 Dyson-Schwinger Equations: Ball-Chiu Vertex

This section centers on the discussion of the coupled system of DSEs for A, B and the polarization scalar Π if the vertex ansatz (2.32) is used for the full fermion-photon vertex Γ.

The equations that are given below refer to the full Curtis-Pennington ansatz (including the transverse part (2.37)). However, for the reasons that have been discussed in section 2.3 the transverse part Γ^T is not taken into account for the numerical analysis.

Using the full vertex $\Gamma = \Gamma^L + \Gamma^T$ one obtains:

$$A(p) = 1 + \frac{e^2}{p^2}\int \frac{d^3k}{(2\pi)^3}\frac{1}{q^2(1+\Pi(q))}\Big(\sigma_v(k)\big(A(k)+A(p)\big)a_1(p,k) + \sigma_v(k)\Delta A(p,k)a_2(p,k) + \sigma_s(k)\Delta B(p,k)a_3(p,k)\Big) \quad (2.54)$$

where the auxiliary functions a_1, a_2 and a_3 have been introduced. These are defined as follows:

$$a_1(p,k) = \frac{1}{q^2}\big(-k^2p^2 + (k^2+p^2)\langle p,k\rangle - \langle p,k\rangle^2\big)\,, \quad (2.55)$$

$$a_2(p,k) = -\frac{p^2+k^2}{q^2}\big(p^2k^2 - \langle p,k\rangle^2\big) + \Omega(p,k)\langle p,k\rangle(p^2-k^2)\,, \quad (2.56)$$

$$a_3(p,k) = -\frac{2}{q^2}\big(p^2k^2 - \langle p,k\rangle^2\big)\,. \quad (2.57)$$

The equation for B reads:

$$B(p) = e^2\int \frac{d^3k}{(2\pi)^3}\frac{1}{q^2(1+\Pi(q))}\Big(\big(A(k)+A(p)\big)\sigma_s(k) + \sigma_s(k)\Delta A(p,k)b_2(p,k) + \sigma_v(k)\Delta B(p,k)b_3(p,k)\Big) \quad (2.58)$$

where again some auxiliary functions have been introduced:

$$b_2(p,k) = \frac{2}{q^2}\big(p^2k^2 - \langle p,k\rangle^2\big) + \Omega(p,k)(p^2-k^2)\,, \quad (2.59)$$

$$b_3(p,k) = -\frac{2}{q^2}\big(p^2k^2 - \langle p,k\rangle^2\big)\,. \quad (2.60)$$

The DSE for the polarization scalar $\Pi(p)$ is given by:

$$\Pi(p) = 2N\frac{e^2}{p^2}\int \frac{d^3k}{(2\pi)^3}\Big(\big(A(k)+A(q)\big)\sigma_v(k)\sigma_v(q)\pi_1(k,p) - \Delta A(k,q)p^2\pi_2(k,p) + 2\Delta B(k,q)\pi_3(k,p) - \Delta A(k,q)\Omega(k,q)\pi_4(k,p)\Big) \quad (2.61)$$

where π_1, π_2, π_3 and π_4 are defined as follows

$$\pi_1(k,p) = k^2 + 2\langle p,k\rangle - \frac{3}{p^2}\langle p,k\rangle^2\,, \quad (2.62)$$

$$\pi_2(k,p) = \sigma_v(k)\sigma_v(q)\big[-k^2 + \frac{2}{p^2}\langle p,k\rangle^2 - \langle p,k\rangle\big] + \sigma_s(k)\sigma_s(q)\,, \quad (2.63)$$

$$\pi_3(k,p) = \sigma_v(k)\sigma_s(q)\langle p,k\rangle + \sigma_s(k)\sigma_v(q)\big[p^2 - \langle p,k\rangle\big] \quad (2.64)$$

and

$$\pi_4(k,p) = \sigma_v(k)\sigma_v(q)\big[2p^2k^2 + p^2\langle p,k\rangle - 4k^2\langle p,k\rangle - 5\langle p,k\rangle^2 + \frac{6}{p^2}\langle p,k\rangle^3\big] - \sigma_s(k)\sigma_s(q)\big[2\langle p,k\rangle - p^2\big] \ . \quad (2.65)$$

The system of equations (2.54), (2.58) and (2.61) has been solved, however, for the reasons that have been discussed in section 2.3 the CP-contribution to these DSEs has been neglected. This amounts to the modifications

$$a_2(p,k) = -\frac{p^2+k^2}{q^2}\big(p^2k^2 - \langle p,k\rangle^2\big) \ , \quad (2.66)$$

$$b_2(p,k) = \frac{2}{q^2}\big(p^2k^2 - \langle p,k\rangle^2\big) \quad \text{and} \quad (2.67)$$

$$\pi_4(k,p) = 0 \quad (2.68)$$

which have been used instead of (2.56), (2.59) and (2.65). Since the results that are obtained for the thus specified truncation scheme are very similar to the results that have been obtained for the bare vertex approximation it suffices to concisely summarize the results.

The qualitative features and especially the phase structure of the theory are the same as for the bare vertex approximation. More precisely: the solutions to the system of DSEs (2.54), (2.58) and (2.61) (subject to the modifications (2.66)-(2.68)) show that the theory undergoes a phase transition at a critical number of flavours N_{crit}. For $N < N_{crit}$ one finds a phase where the chiral symmetry is spontaneously broken and where the electrons are logarithmically confined since the polarization scalar is finite the infrared (cf. eq (2.11)). One the other hand, for $N > N_{crit}$ one finds that the chiral symmetry is unbroken and that the electrons are not confined since the polarization scalar diverges in the infrared (cf. eq (2.11)). The critical number of flavours N_{crit} which marks the phase transition is somewhat smaller than the corresponding result that has been found in the bare vertex approximation. The system of equations (2.54), (2.58) and (2.61) yields $N_{crit} = 2.8$ whereas for the bare vertex approximation it has been found that $N_{crit} = 3.2$.

The results for the vectorial self-energy A and especially for its infrared behaviour are very similar as compared to the results that have been found for the bare vertex approximation which are shown in the left panel of fig. 2.2. The two phases are again distinguished by a qualitatively different infrared behaviour of A. For $N < N_{crit}$ one finds that A becomes constant in the IR whereas for $N > N_{crit}$ one obtains that A has a power-like behaviour for small momenta. This especially implies that $A(x) \to 0$ for $x \to 0$ in the non-confined phase, i.e. for $N > N_{crit}$. These results are in complete qualitative agreement with the results shown in the left panel of fig. 2.2. With regard to the IR limit of A in the confined phase (i.e. for $N < N_{crit}$) there is a small quantitative difference to the results that have been obtained for the bare vertex approximation: $A(0)$ being about 5% to 10% larger (in the confined phase) for the system of equations (2.54), (2.58) and (2.61). Although the result (2.51) is valid only for the bare vertex approximation it is interesting to compare it to the results for the Ball–Chiu ansatz. One finds that the coefficient $b(N)$ is about 5% larger

and that the exponent $\beta(N)$ is about 3% smaller than the corresponding results for the bare vertex approximation, see table 2.1.

Also the results for the scalar self-energy B are quite similar to the corresponding results that have been obtained in the bare vertex approximation (cf. fig. 2.2). I.e. as for the bare vertex approximation one finds that B becomes constant in the infrared for $N < N_{crit}$ and that it vanishes for $N > N_{crit}$. This implies that (also for the Ball–Chiu approximation) the confinement phase transition also is a chiral phase transition. The only difference is that in the confined phase the results for $B(0)$ are about 10% larger than the corresponding results for the bare vertex approximation.

As the results for A and B also the results for the polarization scalar Π are very similar to the corresponding results that have been obtained for the bare vertex approximation. This especially entails that the polarization scalar is qualitatively different in the two phases (cf. fig. 2.3). More precisely: for $N > N_{crit}$ one finds that $\Pi(x) \to \infty$ for $x \to 0$ whereas $\Pi(0)$ is constant for $N < N_{crit}$. Eq. (2.11) then implies that this qualitatively different IR behaviour corresponds to a logarithmically confining potential for $N < N_{crit}$ and to a non-confining potential for $N > N_{crit}$. However, there are small quantitative differences as compared to the bare vertex approximation: for the Ball–Chiu approximation $\Pi(0)$ is found $\approx 5\%$ smaller in the confined phase.

The results for A, B and Π are thus all very similar to the corresponding results for the bare vertex approximation that have been discussed in section 2.4. Therefore it is obvious that also the results for the Fourier transform (2.53) of the propagator are very similar as compared to those results that have been presented in section 2.4. There is thus no evidence that the quark propagator in the confined phase does violate positivity. This has been shown for both truncation schemes: for the bare vertex approximation as well as for the Ball–Chiu ansatz.

Chapter 3

Basic Concepts of QCD

This introductory chapter is to be understood as a brief reminder on some of the more basic concepts of Quantum Chromodynamics (QCD). The main objective being the discussion of the fundamental symmetries of QCD. The subsequent chapters rely on the terminology and the notation that is introduced here. For a more thorough discussion of these basic concepts of QCD and of the formalism see, e.g. [MP78] for a review and [PS95] for a recent introductory textbook.

3.1 The QCD Lagrangian

The theory of strong interactions, QCD is a renormalizable gauge field theory which describes the interactions of coloured quarks and gluons and as such it belongs to the Standard model. A quark is characterized by its flavour and by its colour and the quark fields form the fundamental representation of $SU(3)_c$. The gluon fields, on the other hand, build up the adjoint representation of $SU(3)_c$.

The Lagrangian describing the interactions of quarks and gluons is

$$L_{QCD} = -\frac{1}{4}F^a_{\mu\nu}F^{a\mu\nu} + i\sum_q \bar{\psi}^i_q \gamma^\mu \left[D_\mu\right]_{ij} \psi^j_q - \sum_q m_q \bar{\psi}^i_q \psi_{qi} \tag{3.1}$$

where the definition of the field strength tensor

$$F^a_{\mu\nu} = \partial_\mu A^a_\nu - \partial_\nu A^a_\mu + g_s f_{abc} A^b_\mu A^c_\nu \tag{3.2}$$

and of the covariant derivative

$$\left[D_\mu\right]_{ij} = \delta_{ij}\partial_\mu - ig_s \sum_a \frac{\lambda^a_{ij}}{2} A^a_\mu \tag{3.3}$$

have been used. The strength of all interactions is given by one coupling constant which is denoted by g_s. The f_{abc} are the structure constants of the $SU(3)$ algebra which are related to the generators λ^a according to $[\lambda^a, \lambda^b] = 2if^{abc}\lambda^c$. The quark fields are represented by the 4-component Dirac spinors ψ^i_q where indices i and q refer to colour and flavour respectively. The 8 different gluon fields are denoted by A^a_μ.

3.2 Symmetries of the QCD Lagrangian

The Lagrangian (3.1) can be shown to be invariant under local gauge transformations

$$A_\mu(x) \to U(x)A_\mu(x)U^{-1}(x) + \frac{i}{g_s}U(x)\partial_\mu U^{-1}(x) \tag{3.4}$$

$$\psi_q \to U(x)\psi_q \tag{3.5}$$

where the local $SU(3)_c$ gauge transformation U is defined as

$$U(x) = exp\left(i\theta_a(x)\lambda^a/2\right) . \tag{3.6}$$

In order to fix the gauge one uses the Faddeev–Popov procedure for the path-integral. This procedure is well known [FP67] and in covariant gauges it effectively leads to the addition of two terms to the Lagrangian (3.1):

$$L_{QCD} \to L_{QCD} + L_{GF} + L_{FP} \tag{3.7}$$

with

$$L_{GF} = B^a\partial^\mu A^a_\mu + \frac{\alpha}{2}B^aB^a \quad \text{and} \tag{3.8}$$

$$L_{FP} = i\bar{c}^a\partial^\mu D_\mu c^a . \tag{3.9}$$

The gauge fixing has introduced the gauge parameter α, the auxiliary field B (Nakanishi-Lautrup field) and especially the field c. This last field adds the kinetic term of a scalar field to the Lagrangian, however, it is a Grassmann–valued field which obeys Fermi-statistics and it thus explicitely violates the spin-statistics theorem for physical particles. The quanta of this field are known as *Fadeev-Popov ghosts* [FP67] or simply ghosts.

The complete Langrangian (3.7) therefore contains the classical part L_{QCD} which is invariant under local gauge transformations (3.4). Besides this classical part it contains the gauge fixing terms which can be shown to be not invariant under (3.4). However, the full Lagrangian still has a symmetry which might be viewed as the quantum version of the local gauge symmetry. This new symmetry has been found by Becchi, Rouet and Stora and is called *BRS-symmetry* [BRS75], [BRS76]. In order to define this symmetry one conveniently starts by replacing the (classical) local gauge parameter $\theta^a(x)$ by

$$\theta^a(x) \to \lambda c^a(x) \tag{3.10}$$

where λ is a Grassmann-valued constant. Using this definition one then derives the variation of the fields under the thus modified 'gauge transformation'. The result is:

$$\delta_B\psi(x) = igc(x)\psi(x) , \tag{3.11}$$

$$\delta_B A_\mu(x) = \partial_\mu c(x) + ig\left[c(x), A_\mu(x)\right] , \tag{3.12}$$

$$\delta_B c(x) = igc^2(x) , \tag{3.13}$$

$$\delta_B\bar{c}(x) = iB(x) \quad \text{and} \tag{3.14}$$

$$\delta_B B(x) = 0 \tag{3.15}$$

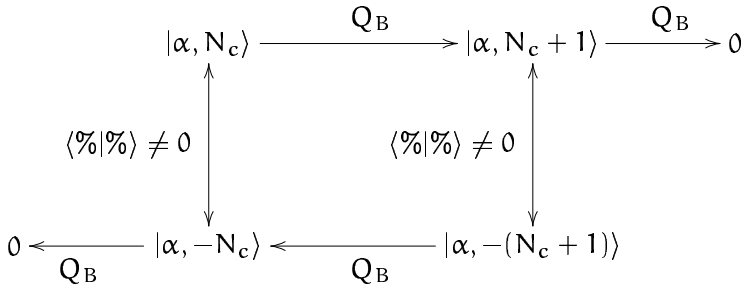

Figure 3.1: Pictorial representation of the BRS-quartet.

where all colour indices have been suppressed[1]. The mapping $\psi \rightarrow \delta_B \psi$ etc. defines the BRS-operator δ_B which, when applied to a field, gives its variation under the BRS-transformation. Looking only at the classical part L_{QCD} of the total Lagrangian the BRS-transformation is nothing but a local gauge transformation, i.e. $\delta_B L_{QCD} = 0$. The (global) BRS-invariance of the full Lagrangian is therefore expressed by the fact that $\delta_B \big(L_{GF} + L_{FP}\big) = 0$, which in turn can be taken as the most general definition of any gauge-fixing term.

The effect of the BRS-operator δ_B on the fields can equally be represented by

$$\big[i\lambda Q_B, \psi\big] = \lambda \delta_B \psi \tag{3.16}$$

and correspondingly for the other fields. This defines the BRS-charge Q_B which is the conserved charge of the Noether current that corresponds to the BRS-symmetry.

Aside from the BRS-symmetry there is yet another symmetry of the full Lagrangian (3.7). It is expressed by the scaling relations

$$c^a(x) \rightarrow exp(\rho) c^a(x) \quad \text{and} \quad \overline{c}^a(x) \rightarrow exp(-\rho) \overline{c}^a(x) \tag{3.17}$$

where ρ is a real number. This symmetry leads (via the Noether theorem) to its own conserved charge: the ghost charge Q_c.

These two charges Q_B and Q_c and their (anti-)commutation relations form the BRS-algebra

$$Q_B^2 = 0\,, \quad \big[iQ_c, Q_B\big] = Q_B\,, \quad \text{and} \quad \big[Q_c, Q_c\big] = 0 \tag{3.18}$$

which gives rise to the *BRS-quartets.* The algebra (3.18) has representations in the space of asymptotic fields. Because of the nil-potency of Q_B it follows that there are only singlets and dublets with respect to Q_B; these will be called BRS-singlets and BRS-dublets in the following. If an asymptotic state is denoted by $|\alpha, N_c\rangle$ (where N_c is the eigenvalue of iQ_c

[1] For a more detailed discussion of the BRS symmetry the reader is referred to [KO79], [NO90] and [Kug97] whereas a detailed account of the applications of the BRS symmetry to the Dyson-Schwinger formalism can be found in [AvS00]

and α collectively denotes all other degrees of freedom) then a BRS-singlet is characterized by

$$Q_B|\alpha, N_c\rangle = 0 \qquad \text{(BRS-singlet)} \tag{3.19}$$

whereas a BRS-dublet is a state that does not satisfy (3.19) and correspondingly fulfils

$$Q_B|\alpha, N_c\rangle = |\alpha, N_c + 1\rangle \ . \qquad \text{(BRS-dublet)} \tag{3.20}$$

Because of $Q_B^2 = 0$ this new state on the left hand side of (3.20) is again a BRS-singlet. The states that can be written in the form $Q_B|\alpha, N_c\rangle$ can never give rise to poles in any Greens function because they have zero norm. In order that the dublet states can give a contribution to Greens functions there must be another state which allows for a nonzero scalar product with the dublet state. The BRS-algebra then dictates that this state has the opposite ghost number N_c. This associated dublet state will then, of course satisfy itself a relation of the form (3.20) such that the two associated dublet states together with their corresponding 'daughter'-states form a BRS-quartet.

3.3 Asymptotic Freedom and Running Coupling

The principle of *asymptotic freedom* expresses the fact that the renormalized QCD coupling constant is small only at high energies. This is the reason why only in this momentum regime it is possible that high precision test can be performed. The running coupling constant of QCD $\alpha_s = g_s^2/(4\pi)$ can be calculated in perturbation theory for large renormalization points; one finds

$$\alpha_s(\mu) = \frac{4\pi}{\beta_0 \ln(\mu^2/\Lambda^2)}\left(1 - \frac{2\beta_1}{\beta_0^2}\frac{\ln\big(\ln(\mu^2/\Lambda^2)\big)}{\ln\big(\ln(\mu^2/\Lambda^2)\big)} + \dots\right) . \tag{3.21}$$

Hereby the constants β_i are the coefficients of the Callan-Symanzik β function which determines the renormalization scale dependence of the running coupling α_s according to

$$\mu\frac{\partial\alpha_s}{\partial\mu} = -\frac{\beta_0}{2\pi}\alpha_s^2 - \frac{\beta_1}{4\pi^2}\alpha_s^3 - \frac{\beta_2}{64\pi^3}\alpha_s^4 - \dots \tag{3.22}$$

with

$$\beta_0 = 11 - \frac{2}{3}N_f \ , \tag{3.23}$$

$$\beta_1 = 51 - \frac{19}{3}N_f \quad \text{and} \tag{3.24}$$

$$\beta_2 = 2857 - \frac{5033}{9}N_f + \frac{325}{27}N_f^2 \ . \tag{3.25}$$

This behaviour of the QCD coupling constant (being large in the infrared and being small in the ultraviolet) is the reason for the distinction between nonperturbative and perturbative physics. While the latter is well understood since the early days of QCD (see e.g.

[MP78]) it is only during the last decade that the nonperturbative aspects of QCD can be investigated.

There are various different methods to investigate the nonperturbative momentum realm. Among them are e.g. lattice simulations [Kar96], [Neg97], the field strength approach [SRAL90], [Qua99], Dyson-Schwinger studies [RW94], [AvS00] and various topological methods [TJZW85], [Nas91]. Most of the studies up to now consider pure Yang-Mills theory or QCD in the quenched approximation, i.e. neglecting the effects of dynamic quarks.

The running coupling (3.21) has been obtained as solution of (3.22). In solving this differential equation for α_s a constant of integration is necessarily introduced. This constant, which has been introduced on a formal level, is the one fundamental constant of QCD that has to be deduced from experiment. For this constant one could use the value of α_s at a special scale μ, however, it corresponds to the convention to introduce the dimensionful parameter Λ. The definition of Λ is (in a sense) arbitrary. But usually it is defined using the parameterization (3.21) for the running coupling α_s. The value of Λ can be determined by comparing (3.21) to the results of experiments which yield e.g. $\alpha_s(M_Z)$. This method does of course depend on the order to which the perturbative expansion (3.21) is known; the present state of the art gives $\Lambda \approx 200 - 360$ MeV [C$^+$98] (This value for Λ refers to the $\overline{MS}$-regularisation scheme). Here an error of about 15 MeV due to the finite order of the perturbative expansion (3.21) is included.

3.4 Confinement

The *confinement* phenomenon expresses the fact that all physical states that are observed are colour $SU(3)$ singlets. Thus the only states that can be found in the physical spectrum are bound states of quarks and gluons. For quarks these are just the combinations $\bar{\psi}^A_\alpha \psi^B_\alpha$, $\psi^A_\alpha \psi^B_\beta \psi^C_\gamma \epsilon^{\alpha\beta\gamma}$ and $\bar{\psi}^A_\alpha \bar{\psi}^B_\beta \bar{\psi}^C_\gamma \epsilon^{\alpha\beta\gamma}$ which correspond to mesons, baryons and anti-baryons. The colour singlet combination of gluon fields are just the glueballs.

Confinement states that the fundamental excitations of QCD (quarks and gluons) cannot be observed albeit they mediate the interaction. Despite the huge efforts and the impressive developments (see e.g. [BP95b], [BP97], [vB98] and [Isg00]) confinement for QCD has not been proven up to now; i.e. it still has the status of a conjecture. Various mechanisms have been proposed in order to explain colour confinement; the most promising ones are shortly discussed in the following.

The most elementary picture of the confinement mechanism builds on the idea of a *flux-tube*. In QED with abelian photons the force between e^+ and e^- is an attractive Coulomb law. The fields spread out to infinity since the photon field does not couple to itself. This is different for QCD: the nonabelian nature of the gluon fields implies that it couples to itself. This may imply that the energy minimising configuration between a quark and an anti-quark is a tube of coloured flux. Such a gluon field configuration would then have a potential energy which is a linearly rising function of the distance between the two quarks, i.e. the quarks would be confined because the energy required to separate them would be infinite.

The flux-tube picture can be put on a more fundamental basis via an analogy to super-

conductivity which has been first proposed by Mandelstam [Man76] and 't Hooft [tH82]. Assume that a (hypothetic) pair of magnetic charges (monopoles) has been placed in a regular type-II superconductor. Then the magnetic field between these two charges is squeezed into a narrow tube due to the Meissner effect. As explained above this would then cause a linear rising potential between the magnetic monopoles thus leading to permanently confined magnetic charges. This analogy suggests that the QCD vacuum might behave like a type-II colour superconductor. However, since in QCD the colour-*electric* charges (i.e. quarks and gluons) are confined the QCD vacuum would have to be identified with a *dual* colour superconductor where 'electric' and 'magnetic' are interchanged with respect to a normal superconductor.

Another picture of confinement is known as *infrared slavery*. It essentially rests on the behaviour of the running coupling α_s as implied by the renormalization group properties of QCD. These necessitate that α_s vanishes for large momenta. The behaviour of α_s for small momenta can only be calculated using genuinely nonperturbative techniques. One might argue that the large momentum behaviour of α_s is also valid for smaller momenta, i.e. α_s might be monotonically rising in the infrared, thus leading to a divergence for $q^2 \to 0$. This would then correspond to an infinite force which prevents colour singlets to break up into coloured fragments.

On a more formal level one might argue that confinement should have a definite influence on the Greens functions of QCD, especially on the 2–particle correlations, the propagators. This is motivated by the way physical (asymptotic) particles are identified in the framework of a standard quantum field theory: as the poles of the 2–particle correlators for real time-like momenta, the position of the pole giving the mass of the corresponding excitation. However, if the propagator has no pole on the real axis then one could interpret this as confinement signature since the particle obviously cannot go on its mass-shell and thus cannot be found in the asymptotic spectrum. However, if the propagator has no pole on the real axis then it must either have complex poles or it must have an essential singularity somewhere or it must be zero. The first alternative (complex poles) has been found to be realized in the confined phase of QED_3 [Mar95], [Mar96]. This is also the approach that is followed in various bound state calculations within the Bethe-Salpeter formalism [SB51] and especially within the covariant diquark-quark model. The applications of this model to kaon photoproduction and the implications on the qualitative features will be discussed in chapter 7.

Another scenario which is supported by growing evidence is the idea that confinement in QCD might be related to *violation of positivity*. The mechanism bears some resemblance to QED in linear covariant gauges: there one finds that one has the (physical) transverse photons but besides one cannot avoid introducing (unphysical) longitudinal and scalar photons. The Gupta–Bleuler condition then defines the appropriate projection condition which separates the physical subspace of the total state space. The work of Nakanishi and Ojima [KO79] shows that in QCD the physical subspace is defined by the condition

$$Q_B|\alpha, N_c\rangle = 0 \; . \tag{3.26}$$

This implies that the physical subspace contains BRS-singlet as well as BRS-quartet states. However, only the daughter–states of the BRS-quartet are included, see (3.20). This re-

sults in a semi-definite physical subspace whereas the metric of a complete BRS-quartet is indefinite, i.e. contains negative norm states which are projected out by the condition (3.26). To summarize: in the physical subspace the quartet states do appear as zero norm states only, phrased differently: some of the quartet states are in the physical subspace but the probability to observe them is zero. This is called the *quartet mechanism.* This classification of states suggests a confinement criterion which is based on positivity: since the physical subspace contains only the BRS-singlets and the daughter–states one might check for violations of positivity. This would then allow to conclude that the corresponding states belong to the negative norm part of the BRS-quartet and do thus not belong to the physical subspace. Whereas the Gupta–Bleuler condition in QED did project out only the longitudinal and the scalar photons the projection (3.26) is assumed to project out all quarks and gluon excitations. This positivity violation scenario with its link to the BRS-quartet mechanism will be shown to nicely explain the results of the coupled system of DSEs that will be discussed.

3.5 A Note on Euclidean Quantum Field Theory

This sections aims at being a brief reminder on the basic axioms of Euclidean Quantum field theories and on the relation of such an approach to the standard Garding-Wightman Quantum field theory. Hereby the *Schwinger functions* (which will be simply called Greens functions in the following) are introduced and defined; the most fundamental of these Schwinger functions, the propagators of gluons, ghosts and quarks being the main focus of the subsequent chapters. The *reconstruction theorem*, that is shortly mentioned, is the basic justification of the present approach.

Quantum field theories can be described in terms of infinite hierarchies of functions. There are different but equivalent hierarchies, like the Wightman functions [Wig56] and the Schwinger functions [Sch59] to mention only two possibilities. This section focuses on the definition of the Schwinger functions and Osterwalder-Schrader reflection positivity, see Haags book [Haa96] for details.

The Wightman functions[2] $w^n(x_1, \ldots, x_n)$ are defined as vacuum expectation values of products of field operators:

$$w^n(x_1, \ldots, x_n) := \langle \Omega | \Phi(x_1) \cdots \Phi(x_n) | \Omega \rangle \tag{3.27}$$

and formally these w^n are tempered distributions over $\mathbb{R}^{4n}$. The set of functions $\{w^n\}$ has to satisfy the Wightman axioms in order to ensure that the $\{w^n\}$ correspond to a standard Garding-Wightman QFT and the additional constraint

$$\langle \Omega | A^* A | \Omega \rangle \geq 0 \text{ for all } A = \sum_n \int \prod_k d^4 x_k \, f^n(x_1, \ldots, x_n) \Phi(x_1) \cdots \Phi(x_n) \tag{3.28}$$

makes sure that the metric of the Hilbert space is positive semidefinite. It has been proven [Wig56] that the hierarchy of functions $\{w^n\}$ contains the information that is necessary to

[2] The term 'function' is used in a broad sense, it includes distributions.

reconstruct the Hilbert space and to deduce the action of

$$\phi(f) := \int d^4x\, \Phi(x) f(x) \tag{3.29}$$

in this space, where f is a test function. This is known as the reconstruction theorem for the Wightman functions.

The Schwinger functions $S^n(x_1, \dots, x_n)$ are defined as the Wightman functions for imaginary times:

$$S^n(x_1, \dots, x_n) := w^n(-ix_1^4, \vec{x}_1, \dots, -ix_n^4, \vec{x}_n) \tag{3.30}$$

and they are the Euclidean pendant of the usual Green's functions. As there are two hierarchies of functions, $\{w^n\}$ and $\{S^n\}$ the question arises whether it is possible to translate the two descriptions into one another. This is answered by the Osterwalder-Schrader axioms [OS73],[OS75] which may be called the axioms of Euclidean QFT. These axioms are the conditions on the hierarchy $\{S^n\}$ which guaranty that their analytic continuation leads to distributions in Minkowski space satisfying the Wightman axioms and the reconstruction theorem.

The Osterwalder-Schrader reflection positivity is the Euclidean counterpart of the positivity constraint (3.28) and it is defined as follows:

$$\sum_{n+m} S^{n+m}\big(\Theta[f_n \otimes f_m]\big) \geq 0 \tag{3.31}$$

for all test functions $f_n, f_m \in \mathcal{S}_+(\mathbb{R}^{4n})$ where the tensor product $f_n \otimes f_m$ is understood as

$$[f_n \otimes f_m](x_1, \dots, x_n, y_1, \dots, y_m) := f_n(x_1, \dots, x_n) \cdot f_m(y_1, \dots, y_m) \tag{3.32}$$

and the Θ-operation is defined as

$$\Theta f_n(x_1, \dots, x_n) := \bar{f}_n(\theta x_1, \dots, \theta x_n) \text{ with } \theta x = \theta(x^4, \vec{x}) := (-x^4, \vec{x}) \tag{3.33}$$

If the hierarchy $\{S^n\}$ does satisfy Osterwalder-Schrader reflection positivity then the corresponding Hilbert space will have a positive semidefinite metric. This equivalence of reflection positivity and of the positivity of the corresponding metric is utilized in section 6.5 where it is studied whether the gluon- and quark propagators do violate reflection positivity.

Chapter 4

DSEs for Gluons and Ghosts

In this section we discuss the coupled system of Dyson-Schwinger equations (DSEs) for the gluon-, ghost-, and quark-propagators. Hereby the main objective is to introduce the formal framework; the solutions are discussed in chapter 6. Having introduced the DSEs for Landau gauge QCD the subtraction scheme is examined. Following this the nonperturbative running coupling in this approach is identified and some of the major consequences of this identification are discussed. The leading order infrared analysis will yield the infrared limit of the gluon- and ghost renormalization functions; this can then be used to deduce the infrared behaviour of the nonperturbative running coupling. This chapter ends with the introduction of a scale invariant representation of the DSEs.

4.1 DSEs of Landau Gauge QCD

In this section we present the coupled system of DSEs for the gluon-, ghost and quark propagators. The derivation of these DSEs rests on the fundamental symmetries of QCD, especially on the BRS symmetry of the Lagrangian (3.7). Since this derivation of the DSEs as well as the construction of the vertices has been discussed in great detail in [vS98] and [AvS00] it adds to the conciseness of the present work if the reader is referred to these publications. In this section we give a short summary of the discussion and present the DSEs for later reference.

The full coupled system of DSEs for the gluon-, ghost and quark propagators is shown in fig. 4.1. The 3-gluon vertex, the gluon-ghost vertex and the gluon-quark vertex that appear in these DSEs are the solutions of their own DSEs. These DSEs for the vertices then contain even higher Green's function. This hierarchy of DSEs is an infinite systems of coupled equations for the Green's functions of QCD. An exact solution to this system of equations is known to contain all information that can be extracted from a local quantum field theory [Haa96] (See also the discussion in section 3.5 which relates the Minkowski-space Green's functions to the Euclidean-space Green's functions.). However, an exact solution is not feasible and therefore a truncation scheme has to be specified which renders the solution possible. This truncation scheme must reflect the basic symmetries of QCD as expressed by the Slavnov-Taylor identities (STIs). Therefore it is advantageous to specify a consistent

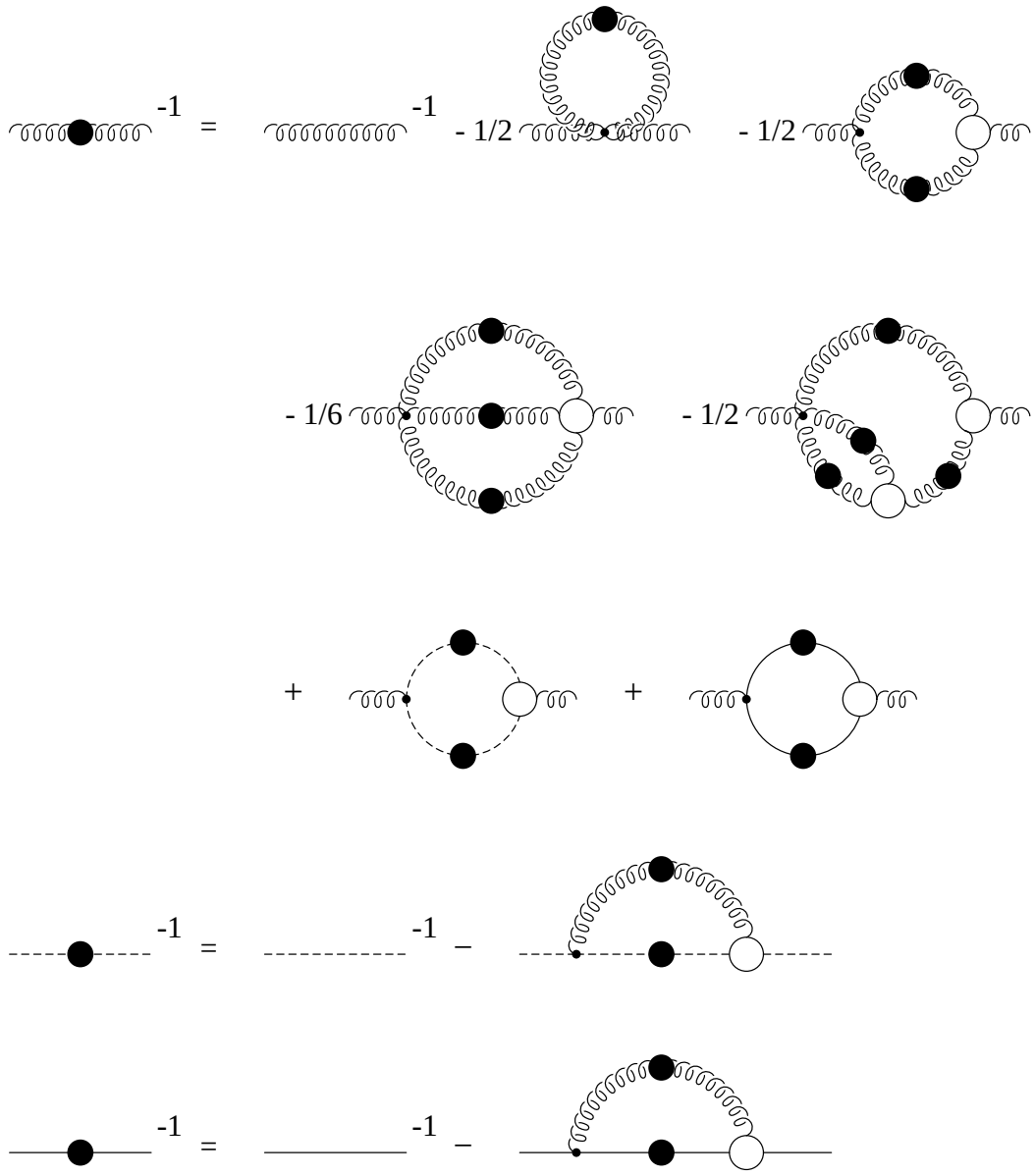

Figure 4.1: Diagrammatical representation of the DSEs for the gluon-, ghost- and quark propagators in Landau gauge QCD. The upmost equation represents the DSE for the gluon-propagator (4.1). The equation in the middle and at the bottom of the figure depict the DSE for the ghost- (4.2) and quark propagators (4.3) respectively. The two-loop contributions to the gluon DSEs are neglected according to the truncation scheme that is discussed in the main text.

truncation scheme for these STIs *and* for the DSEs. The approximate (or truncated) STIs are then solved to obtain the vertices which are used in the DSEs. This is the procedure that is developed and applied in [vSHA97],[vSHA98] and which is reviewed in great detail in [AvS00].

The truncation scheme that is used in the present approach is guided by the prescription that all two-loop contributions (like e.g. the two-loop contributions to the gluon DSE) are neglected. This truncation scheme is applied to the derivation of the STIs as well as to the DSEs.

The exact DSE for the gluon propagator D which is depicted in the upper line of fig. 4.1 is explicitely given by

$$\begin{aligned} D^{-1}_{\mu\nu}(k) = Z_3[D^0]^{-1}_{\mu\nu}(k) - g^2 N_c \tilde{Z}_1 \int \frac{d^4q}{(2\pi)^4} i q_\mu D_G(p) D_G(q) G_\nu(p,q) \\ - g^2 Z_{1F} N_f \frac{1}{2} \int \frac{d^4q}{(2\pi)^4} \mathrm{tr}\left[\gamma_\mu S(p) \Gamma_\nu(p,q) S(q)\right] \\ + g^2 N_c Z_1 \frac{1}{2} \int \frac{d^4q}{(2\pi)^4} \Gamma^0_{\mu\rho\alpha}(k,-q,p) D_{\alpha\beta}(q) D_{\rho\sigma}(p) \Gamma_{\beta\sigma\nu}(-q,p,-k) \end{aligned} \quad (4.1)$$

where $p = k + p$ and D^0 and Γ^0 are the bare gluon propagator and the bare 3-gluon vertex. D_G and S are the full propagators of ghosts and quarks respectively and Γ, G are the corresponding fully dressed 3-point vertex functions.

The DSE for the ghost propagator D_G in Landau gauge is represented by the second line in fig. 4.1. Without any truncations and in full generality it is given by

$$D_G^{-1}(k) = -\tilde{Z}_3 k^2 + g^2 N_c \tilde{Z}_1 \int \frac{d^4q}{(2\pi)^4} i k_\mu D_G(q) G_\nu(q,k) D_{\mu\nu}(k-q) \,. \quad (4.2)$$

Finally, for the exact DSE for the quark propagator S (which is shown in the bottom line of fig. 4.1) one obtains

$$\begin{aligned} S^{-1}(k) = Z_2\left(-i\not{k} + Z_m m_0\right) \\ + g^2 Z_{1F} C_f \int \frac{d^4q}{(2\pi)^4} \gamma_\mu S(q) \Gamma_\nu(q,k) D_{\mu\nu}(k-q) \,. \end{aligned} \quad (4.3)$$

The renormalization constants relate the renormalized quantities with the corresponding unrenormalized propagators, masses and coupling constants. The field renormalization constants are defined by the relations

$$Z_2 S = S^0 \,, \quad \tilde{Z}_3 D_G = D^0_G \,, \quad Z_3 D_{\mu\nu} = D^0_{\mu\nu} \quad (4.4)$$

and the multiplicative renormalization of the mass m and the coupling g is formally defined by the relations

$$Z_g g = g^0 \quad \text{and} \quad Z_m m = m^0 \,. \quad (4.5)$$

The remaining renormalization constants are tied to the renormalizations constants that have been introduced thus far according to the Landau gauge relations

$$Z_1 = Z_g Z_3^{3/2} , \quad \tilde{Z}_1 = Z_g Z_3^{1/2} \tilde{Z}_3 \quad \text{and} \quad Z_{1F} = Z_g Z_2 Z_3^{1/2} . \tag{4.6}$$

The nonperturbative contributions to the gluon-, ghost and quark propagators in covariant gauges are represented by the deviation of the renormalization functions Z, G, A and B from their corresponding perturbative limits. The renormalization function Z for the gluon is defined via the relation

$$D_{\mu\nu}(k) = \left(\delta_{\mu\nu} - \frac{k_\mu k_\nu}{k^2}\right) \frac{Z(k^2)}{k^2} + \xi \frac{k_\mu k_\nu}{k^4} \tag{4.7}$$

and the corresponding renormalization function for the ghost according to the definition

$$D_G(k) = -\frac{G(k^2)}{k^2} . \tag{4.8}$$

The renormalization functions A and B for the quark propagator

$$S^{-1}(k) = -i\not{k} A(k^2) + B(k^2) \tag{4.9}$$

are usually called the vectorial and the scalar self-energy respectively.

The set of equations (4.1), (4.2) and (4.3) is not a closed system of equations as yet since the vertices satisfy their own DSEs. In order to arrive at a closed set of equations one has to impose a truncation scheme which maintains the symmetries of the theory and which allows to construct the 3-point vertices. The symmetries are expressed by the STIs [Tay71] which in turn are a consequence of the gauge- and BRS invariance of the theory. However, these identities in general cannot constrain the vertex completely; much like in QED where the Ward-Takahashi identity determines only the longitudinal part of the full vertex but leaves the transversal part unconstrained. Other requirements like multiplicative renormalizability, absence of kinematical singularities and the correct perturbative limit have to be used to further constrain the vertex ansatz. The truncation scheme is specified by the guiding principle that any two-loop contributions to the DSEs itself as well as to the STIs are neglected. The truncation scheme and the construction of the vertices is developed in [vSHA98] and reviewed in great detail in [AvS00]. In the following the thus constructed vertices are merely presented and the interested reader is referred to the cited publications.

The 3-gluon vertex is defined according to

$$\Gamma^{abc}_{\mu\nu\rho}(p,q,k) = g f^{abc} (2\pi)^4 \delta^4(p+q+k) \Gamma_{\mu\nu\rho}(p,q,k) =$$

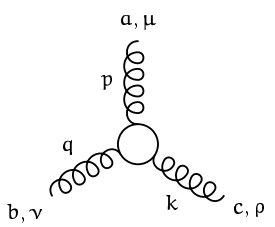

where all three momenta are assumed to point outwards. The result that is derived in [AvS00] explicitely reads

$$\Gamma_{\mu\nu\rho}(p,q,k) = -A_+\delta_{\mu\nu}i(p-q)_\rho - A_-\delta_{\mu\nu}i(p+q)_\rho \\ -2\frac{A_-}{p^2-q^2}(\delta_{\mu\nu}pq - p_\nu q_\mu)(p-q)_\rho + \text{cyclic perm.} \quad (4.10)$$

where

$$A_\pm(p,q^2,k^2) = \frac{G(k^2)}{2}\left(\frac{G(q^2)}{G(p^2)Z(p^2)} \pm \frac{G(p^2)}{G(q^2)Z(q^2)}\right). \quad (4.11)$$

The gluon ghost vertex is constructed in a similar manner as the 3-gluon vertex. As for the 3-gluon vertex we refer the reader to [vS98] and [AvS00] where the derivation of the vertex is discussed in detail. Here we simply give the definition for later reference:

$$G_\mu^{abc}(p,q,k) = (2\pi)^4\delta^4(p+q-k)gf^{abc}iq_\nu\tilde{G}_{\mu\nu}(q,k) =$$

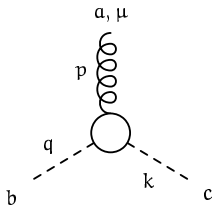

where all momenta point outwards and the remaining 'reduced vertex' $\tilde{G}_{\mu\nu}$ is defined as

$$\tilde{G}_{\mu\nu}(q,k) = \delta_{\mu\nu}\frac{G(p^2)}{G(q^2)} + \left(\frac{G(p^2)}{G(k^2)} - 1\right)\frac{k_\mu q_\nu}{q^2}. \quad (4.12)$$

The quark-gluon vertex is constructed according to the Ball-Chiu [BC80a] prescription and its transverse part is set equal to the Curtis-Pennington [CP90] ansatz. This resulting vertex ansatz is discussed in detail in section 2.3 where it is used to describe the electron-photon coupling in QED_3 . The difference between the Curtis-Pennington vertex as it is used in e.g. in QED_3 and the quark-gluon vertex in Landau gauge QCD is dictated by the corresponding STI (5.5) which at the present truncation level yields

$$\Gamma_\mu^a(p,q) = -gt^aG(k^2)\left(\Gamma_\mu^L(p,q) + \Gamma_\mu^T(p,q)\right) =$$

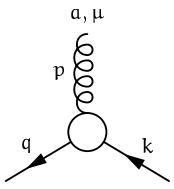

where Γ_μ^L and Γ_μ^T denote the longitudinal (Ball–Chiu [BC80a], [BC80b]) part and the transverse (Curtis–Pennington [CP90]) part of the vertex respectively (see section 2.3 for the definitions).

4.2 Subtraction Scheme

In the preceding section the formal framework of the Landau gauge DSEs has been introduced. The results of the vertex construction have been presented such that the DSEs for the gluon-, ghost- and quark propagators do now form a closed set of equations. Starting with the ghost DSE (4.2) and the gluon-ghost vertex as defined in the last section the unrenormalized ghost DSE can be written in the form (expressed in terms of renormalized quantities)

$$\frac{1}{G(k^2)} = \tilde{Z}_3 - g^2 N_c \int \frac{d^4q}{(2\pi)^4} \left[kP(p)q\right] \frac{Z(p^2)G(q^2)}{k^2 p^2 q^2} \left(\frac{G(p^2)}{G(q^2)} + \frac{G(p^2)}{G(k^2)} - 1 \right) \tag{4.13}$$

where $p = k - q$ and where it has been used that $\tilde{Z}_1 = 1$ [Tay71]. Here and in the following the definition

$$P(p) = \delta_{\mu\nu} - \frac{p_\mu p_\nu}{p^2} \tag{4.14}$$

is used.

As has been mentioned already: in order to be able to perform the infrared analysis it is necessary to use a one-dimensional approximation for the renormalization functions of the gluon and the ghost. The approximation we use rests on the the following assumptions: for $q^2 > k^2$ one assumes that the functions Z and G are slowly varying with respect to their arguments thus that it is allowed to replace $G(p^2) \sim G(k^2) \to G(q^2)$. If all momenta are large, i.e. in the perturbative limit, this assumption is well justified because of the logarithmic momentum dependence of the renormalization functions for large momenta. More precisely: this assumption guarantees the correct leading ultraviolet behaviour of the renormalization functions of the gluon and the ghost.

It is anticipated that the DSEs for the gluon and the ghost will contain infrared divergent terms. Therefore it would be inappropriate to use the same prescription also for the case that $q^2 < k^2$. Here it is more appropriate to employ an angle approximation preserving the limit $q^2 \to 0$ of the integrands. This is achieved in using: $G(p^2) \to G(k^2)$ and $Z(p^2) \to Z(k^2)$.

Using this angle-approximation the DSE for the ghost (4.13) becomes

$$\frac{1}{G(k^2)} = \tilde{Z}_3 - \frac{g^2}{16\pi^2} \frac{3N_c}{4} \left(\frac{1}{2} Z(k^2) G(k^2) + \int_{k^2}^{\Lambda^2} \frac{dq^2}{q^2} Z(q^2) G(q^2) \right) . \tag{4.15}$$

In order to eliminate the dependence on the cutoff Λ we can subtract the ghost DSE (4.13) at the renormalization point μ^2. This gives

$$\begin{aligned} \frac{1}{G(k^2)} - \frac{1}{G(\mu^2)} = \frac{g^2}{16\pi^2} \frac{3N_c}{4} \Bigg(& \frac{1}{2} Z(\mu^2) G(\mu^2) - \frac{1}{2} Z(k^2) G(k^2) \\ & + \int_0^{k^2} \frac{dq^2}{q^2} Z(q^2) G(q^2) - \int_0^{\mu^2} \frac{dq^2}{q^2} Z(q^2) G(q^2) \Bigg) . \end{aligned} \tag{4.16}$$

This is the renormalized ghost DSE in its explicit subtracted form; there is no cutoff dependence left but the equation does depend on the renormalization point μ^2. To make the following discussion more lucid it is advantageous to streamline the notation. The k-dependent terms on the right hand side of (4.15) will be denoted by

$$\Sigma_G(k^2) = \frac{g^2}{16\pi^2}\frac{3N_c}{4}\left(-\frac{1}{2}Z(k^2)G(k^2) + \int_0^{k^2}\frac{dq^2}{q^2}Z(q^2)G(q^2)\right) \tag{4.17}$$

such that the ghost DSE in its subtracted form (4.15) now reads

$$\frac{1}{G(k^2)} = \Sigma_G(k^2) + \left[\frac{1}{G(\mu^2)} - \Sigma_G(\mu^2)\right] \tag{4.18}$$

or in yet more condensed notation

$$\frac{1}{G(k^2)} = \Sigma_G(k^2) + c(\mu^2) \tag{4.19}$$

where c is a constant with respect to k^2 but does, of course, depend on the renormalization point. Please note, that c is not to be confused with $\tilde{Z}_3$, the latter being UV divergent whereas c does not depend on the UV cutoff. Every value of c gives a solution to the ghost DSE and corresponds to a renormalization point. Up to now the value of c is completely unconstrained, $c = 0$ being only one possibility.

It is important to note, that in principle, it is not possible, to split (4.18) up into two equations, one containing only the k-dependent terms and the other only the μ-dependent terms. In doing so one would have to face the ambiguity of introducing an arbitrary constant according to

$$\frac{1}{G(k^2)} - \Sigma_G(k^2) = \frac{1}{G(\mu^2)} - \Sigma_G(\mu^2) \tag{4.20}$$

which (without further constraints) cannot be distinguished from

$$\frac{1}{G(k^2)} - \Sigma_G(k^2) + d = \frac{1}{G(\mu^2)} - \Sigma_G(\mu^2) + d \tag{4.21}$$

where d is some arbitrary constant. This explicitely shows, that, in general, there is now way back from the subtracted equation in the form (4.18) to a variant of the unsubtracted equation which would contain only the k or only the μ dependent terms. The reason being that in going form (4.15) to (4.15) one has lost all information on the constant terms.

The DSE for the gluon, while being more complicated, can be treated in the same way as the DSE for the ghost. Without any approximations and with the vertices discussed in

section 4.1 the DSE for gluon explicitely reads

$$\begin{aligned}\frac{1}{Z(k^2)} = Z_3 - Z_1\frac{g^2N_c}{6}\int\frac{d^4q}{(2\pi)^4}\Bigg(&N_1(p^2,q^2,k^2)\frac{Z(p^2)G(p^2)Z(q^2)G(q^2)}{Z(k^2)G(k^2)}\\ &+N_2(p^2,q^2,k^2)\left[\frac{Z(p^2)G(p^2)}{G(q^2)}+\frac{Z(q^2)G(q^2)}{G(p^2)}\right]\Bigg)\frac{G(k^2)}{k^2p^2q^2}\\ &+\frac{g^2N_c}{3}\int\frac{d^4q}{(2\pi)^4}\Bigg(\left[qR(k)q\right]\left[G(k^2)G(p^2)-G(q^2)G(p^2)\right]\\ &-\left[qR(k)p\right]G(k^2)G(q^2)\Bigg)\frac{1}{k^2p^2q^2}-g^2Z_{1F}\frac{N_f}{2}\Pi(k^2)\end{aligned}\tag{4.22}$$

where the auxiliary functions N_1 and N_2 are defined as follows:

$$\begin{aligned}N_1(x,y,z) = &\frac{29}{4}x+\frac{1}{4}\frac{x^2}{y}+\frac{29}{4}y+\frac{1}{4}\frac{y^2}{x}+\frac{(9x^2+50xy+9y^2)z}{4xy}\\ &-\frac{9(x+y)z^2}{4xy}-\frac{z^3}{4xy}+\frac{24x^2-10xy+y^2}{2(z-x)}+\frac{24y^2-10xy+x^2}{2(z-y)}\end{aligned}\tag{4.23}$$

and

$$\begin{aligned}N_2(x,y,z) = &\frac{5x^3+41x^2y+5xy^2-3y^3}{4x(y-x)}+\frac{x^2-10xy+24y^2}{2(y-z)}\\ &+\frac{x^3+9x^2y-9xy^2-y^3}{xz}+\frac{(2x^2+11xy-3y^2)z}{2x(x-y)}+\frac{(x+y)z^2}{4x(y-x)}\,.\end{aligned}\tag{4.24}$$

Furthermore the polarization scalar of the quark loop is denoted by $\Pi(k^2)$. For the following discussion we will set $N_f = 0$, the details and the modifications concerning the quark loop will be discussed in chapter 5.

Using the same angular approximation that we used for the ghost DSE we obtain

$$\begin{aligned}\frac{1}{Z(k^2)} = Z_3 + Z_1\frac{g^2N_c}{48\pi^2}\Bigg(&\int_0^{k^2}\frac{dq^2}{k^2}\left[\frac{7}{2}\frac{q^4}{k^4}-\frac{17}{2}\frac{q^2}{k^2}-\frac{9}{8}\right]Z(q^2)G(q^2)\\ &+\int_{k^2}^{\Lambda^2}\frac{dq^2}{q^2}\left[\frac{7}{8}\frac{k^2}{q^2}-7\right]Z(q^2)G(q^2)\Bigg)\\ &+\frac{g^2N_c}{48\pi^2}\left(\frac{3}{2}G(k^2)\int_0^{k^2}\frac{dq^2}{q^2}\frac{q^2}{k^2}G(q^2)-\frac{1}{3}G^2(k^2)+\frac{1}{2}\int_{k^2}^{\Lambda^2}\frac{dq^2}{q^2}G^2(q^2)\right).\end{aligned}\tag{4.25}$$

In order to eliminate the cutoff dependence we subtract the equation at the renormalization point μ. For the following discussion it therefore suffices to look at the cutoff dependent terms of (4.25), which (after subtraction and up to constant factors) are:

$$\begin{aligned}&\left(\int_{k^2}^{\Lambda^2}\frac{dq^2}{q^2}\left[\frac{7}{8}\frac{k^2}{q^2}-7\right]ZG-(k\to\mu)\right) =\\ &\qquad\left(\frac{7}{8}k^2\int_{k^2}^{\Lambda^2}\frac{dq^2}{q^4}ZG-7\int_0^{k^2}\frac{dq^2}{q^2}ZG-(k\to\mu)\right).\end{aligned}\tag{4.26}$$

For the contribution

$$\left(\int_{k^2}^{\Lambda^2} \frac{dq^2}{q^2} G^2(q^2) - (k \to \mu)\right) = \int_{k^2}^{\mu^2} \frac{dq^2}{q^2} G^2(q^2) \tag{4.27}$$

it is necessary to be a bit more careful since the integrand is highly singular in the limit $q^2 \to 0$. In a first step we can write (4.27) as:

$$\int_{k^2}^{\mu^2} \frac{dq^2}{q^2} G^2(q^2) = \lim_{\epsilon \to 0} \left(\int_{k^2}^{-\epsilon} \frac{dq^2}{q^2} G^2(q^2) + \int_{+\epsilon}^{\mu^2} \frac{dq^2}{q^2} G^2(q^2) \right) . \tag{4.28}$$

where ϵ is a small number which will be set to zero at the end. Now we can make the divergent contribution explicit:

$$\int_{k^2}^{-\epsilon} \frac{dq^2}{q^2} G^2(q^2) = \int_{k^2}^{-\epsilon} \frac{dq^2}{q^2} \left[G^2(q^2) - \frac{a^{2\delta}}{2\kappa b^2 q^{4\kappa}} \right] - \frac{a^{2\delta}}{2\kappa b^2 \epsilon^{4\kappa}} - \frac{a^{2\delta}}{2\kappa b^2 k^{4\kappa}} . \tag{4.29}$$

The divergent ϵ-dependent term has been made explicit and it is cancelled by the corresponding divergent term of the μ integral. Thus the integral on the right hand side is now IR finite and the limit $\epsilon \to 0$ may be taken (for the integral). Altogether one than has:

$$\int_{k^2}^{\mu^2} \frac{dq^2}{q^2} G^2(q^2) = \left(\int_{k^2}^{0} \frac{dq^2}{q^2} \left[G^2(q^2) - \frac{a^{2\delta}}{2\kappa b^2 q^{4\kappa}} \right] - \frac{a^{2\delta}}{2\kappa b^2 k^{4\kappa}} - (k \to \mu) \right) . \tag{4.30}$$

Putting everything together we can write the renormalized gluon DSE in its subtracted form as

$$\frac{1}{Z(k^2)} - \frac{1}{Z(\mu^2)} = \Sigma_Z(k^2) - \Sigma_Z(\mu^2) \tag{4.31}$$

where the definition

$$\begin{aligned} \Sigma_Z(k^2) = Z_1 \frac{g^2 N_c}{48\pi^2} \Bigg(& \int_0^{k^2} \frac{dq^2}{k^2} \left[\frac{7}{2} \frac{q^4}{k^4} - \frac{17}{2} \frac{q^2}{k^2} - \frac{9}{8} + 7 \frac{k^2}{q^2} \right] Z(q^2) G(q^2) \\ & + \frac{7}{8} k^2 \int_{k^2}^{\Lambda^2} \frac{dq^2}{q^4} ZG \Bigg) + \frac{g^2 N_c}{48\pi^2} \Bigg(\frac{3}{2} G(k^2) \int_0^{k^2} \frac{dq^2}{q^2} \frac{q^2}{k^2} G(q^2) \\ & - \frac{1}{3} G^2(k^2) - \int_{k^2}^{0} \frac{dq^2}{q^2} \left[G^2(q^2) - \frac{a^{2\delta}}{2\kappa b^2 q^{4\kappa}} \right] - \frac{a^{2\delta}}{2\kappa b^2 k^{4\kappa}} \Bigg) \end{aligned} \tag{4.32}$$

has been introduced.

Again it should be noted that it is, in general, not possible to split the DSE in its subtracted form (4.31) up into two parts; one containing only the k-dependence and the other containing only the μ-dependent terms. In doing so one could again introduce an arbitrary constant, compare the discussion for the ghost and eq. (4.21). Separating out the

k-dependent part and solving this equation is *not* wrong; however, it does correspond to the (additional) constraint:

$$\frac{1}{Z(\mu^2)} - \Sigma_Z(\mu^2) = 0 \tag{4.33}$$

which selects one solution of a one parameter family of solutions.

It seems to be more justified to solve the DSE in its explicitely subtracted form without separating the k and the μ dependent terms into two separate equations. Because then no additional constraint of the form (4.33) is imposed and the system of equations is retained in its most general form. There are yet other (technical) advantages if the equation is used in the full subtracted (and not again separated form). This will be detailed in the subsequent sections.

4.3 Nonperturbative Running Coupling and Renormalization

In the Landau gauge one has the identity [Tay71]

$$\tilde{Z}_1 = Z_g Z_3^{1/2} \tilde{Z}_3 = 1 \tag{4.34}$$

which implies that $g^2 Z(k^2) G^2(k^2)$ is renormalization group invariant. And since there is no other dimensionful parameter one has to conclude that $g^2 Z G^2$ is a function of the running coupling $\bar{g}$ only

$$g^2 Z(k^2) G^2(k^2) = f(\bar{g}^2(t(k), g)) \tag{4.35}$$

where $t = \frac{1}{2}\log(k^2/\mu^2)$ and $\bar{g}$ is the solution of the renormalization group equation

$$\frac{d}{dt}\bar{g}(t, g) = \beta(\bar{g}) \tag{4.36}$$

subject to the boundary condition $\bar{g}(0, g) = g$ and where β is the Callan-Symanzik β-function which is the rate of change of the renormalized coupling with respect to the renormalization point and at fixed bare coupling. If the product $g^2 Z(k^2) G^2(k^2)$ is to be identified with the renormalized running coupling then one should have that $f(\bar{g}^2) \to \bar{g}^2$ for $\bar{g}^2 \to 0$. which corresponds to

$$Z(\mu^2) G^2(\mu^2) = 1 \tag{4.37}$$

for an asymptotically large subtraction point μ, such that at the renormalization point one has

$$g^2 \underbrace{\left[Z(\mu^2) G^2(\mu^2)\right]}_{1} = \underbrace{f(\bar{g}^2(t(\mu), g))}_{\bar{g}^2(t(\mu), g)} . \tag{4.38}$$

Now we assume that $g^2 Z(k^2) G^2(k^2)$ corresponds to an observable quantity. This assumption then implies that $g^2 Z(k^2) G^2(k^2)$ should be invariant under renormalization group transformations (which correspond to finite renormalizations)

$$(g, \mu) \to (g', \mu') \tag{4.39}$$

which entails that:

$$g'^2 \underbrace{\left[Z(\mu'^2) G^2(\mu'^2)\right]}_{1} = \underbrace{f(\bar{g}^2(t(\mu'), g'))}_{\bar{g}^2(t(\mu'), g')} . \tag{4.40}$$

However, this can only be valid if $f(\bar{g}^2(t(k), g)) = \bar{g}^2$ for all k.

The preceding discussion shows that $g^2 Z(k^2) G^2(k^2)$ gives a physically sensible definition of the nonperturbative running coupling in the Landau gauge.

The perturbative subtraction scheme would suggest to use the renormalization conditions

$$Z(\mu) = G(\mu) = 1 \tag{4.41}$$

instead of (4.37). However, if one would extend this to arbitrary scales than this would imply a relation between Z and G which is inconsistent with the leading infrared behaviour of the solutions [vS98]. I.e. the two independent renormalization conditions (4.41) turn out to be to restrictive to be used in the present approach.

To summarize: the nonperturbative renormalization condition that we use is encoded in the equations

$$Z(\mu^2) = f_A(g), G(\mu^2) = f_G(g) \qquad \text{with} \qquad f_A f_G^2 = 1 \tag{4.42}$$

together with the limits $f_A, G \to 1$ for $g \to 0$.

Using this one can find an explicit solution of the Callan-Symanzik equation, which can be written in the form

$$Z(k^2) = f_A(\bar{g}(t(k), g) \cdot \exp\left(-2 \int_g^{\bar{g}(t(k), g)} dl \frac{\gamma_A(l)}{\beta(l)}\right) \quad \text{and} \tag{4.43}$$

$$G(k^2) = f_G(\bar{g}(t(k), g) \cdot \exp\left(-2 \int_g^{\bar{g}(t(k), g)} dl \frac{\gamma_G(l)}{\beta(l)}\right) \tag{4.44}$$

where $\gamma_A(g)$ and $\gamma_G(g)$ are the anomalous dimensions of gluons and ghosts respectively. The identity (4.34) translates into

$$2\gamma_G(g) + \gamma_A(g) = -\frac{1}{g}\beta(g) \tag{4.45}$$

which again tells that $g^2 Z G^2$ is indeed the nonperturbative running coupling. This equations can be formally solved using the splitting

$$\gamma_G(g) = -\big(\delta + \epsilon(g)\big)\frac{\beta(g)}{g} \quad \text{and} \tag{4.46}$$

$$\gamma_A(g) = -\big(1 - 2\delta - 2\epsilon(g)\big)\frac{\beta(g)}{g} \tag{4.47}$$

which introduced the unknown function $\epsilon(g)$ and $\delta = 9N_c/(44N_c - 8N_f)$. However, having introduced this formal solution of (4.45) we can elaborate on the solutions (4.43)

$$Z(k^2) = \left[\left(\frac{\bar{g}^2(t(k),g)}{g^2}\right)^{1-2\delta} f_A(\bar{g}(t(k),g)\right]\left[\exp\left(2\int_g^{\bar{g}(t(k),g)} dl \frac{\epsilon(l)}{\beta(l)}\right)\right]^{-2}, \quad (4.48)$$

$$G(k^2) = \left[\left(\frac{\bar{g}^2(t(k),g)}{g^2}\right)^{\delta} f_G(\bar{g}(t(k),g)\right]\left[\exp\left(2\int_g^{\bar{g}(t(k),g)} dl \frac{\epsilon(l)}{\beta(l)}\right)\right]. \quad (4.49)$$

This formal solution of the Callan-Symanzik equation especially demonstrates that the ϵ-dependent terms cancel in the product ZG^2 such that the renormalization condition (4.42) is explicitely verified.

The formal solution (4.43) motivates the ansatz

$$Z(k^2) = \left(\frac{F(x)}{F(s)}\right)^{1-2\delta} R^2(x) \quad \text{and} \quad G(k^2) = \left(\frac{F(x)}{F(s)}\right)^{\delta} \frac{1}{R(x)} \quad (4.50)$$

which defines the auxiliary functions F and R and uses the definitions $x = k^2/\sigma$ and $s = \mu^2/\sigma$ for the external momentum k and the renormalization point μ. Hereby the (RG invariant) scale $\sqrt{\sigma}$ has been introduced which is as yet undetermined. The definition (4.50) obviously implements the renormalization condition (4.42) which amounts to:

$$ZG^2 = \frac{F(x)}{F(s)} \quad \Rightarrow \quad ZG^2\Big|_{\mu^2} = 1\,. \quad (4.51)$$

The nonperturbative running coupling $\bar{g}^2$ is then proportional to F. This constant of proportionality is fixed to be β_0

$$\beta_0\bar{g}^2(t(k),g) = F(x) \quad \Rightarrow \quad \alpha_s(\mu) = \frac{g^2}{4\pi} = \frac{1}{4\pi\beta_0}F(s)\,. \quad (4.52)$$

Please note that the value of F and R is not constrained in any way by the renormalization condition (4.42) since R cancels and F does occur only as a fraction in (4.51). Phrased differently: it is simply the form of the relation between Z, G and F, R that guarantees that (4.42) is satisfied, i.e. the renormalization condition (4.42) is satisfied regardless of the functional shape or the values of F and R in the perturbative domain. This reflects the reduced number of renormalization conditions; the perturbative subtraction scheme would impose the *two* conditions (4.41) on the functions Z and G. The nonperturbative extension of this perturbative subtraction scheme imposes only *one* condition on the product ZG^2. This has to be kept in mind since this will turn out to be the key to select between a one parameter family of solutions which will be found.

4.4 Leading Order Infrared Analysis

The infrared behaviour of the gluon- and ghost renormalization functions Z and G will turn out to be the most interesting aspect of the solutions. This is because the IR behaviour of Z

and G determines the infrared behaviour of the running coupling and it will also give a close connection to the Kugo-Ojima confinement criterion [Kug95],[WA01]. In the following the leading contribution to the IR behaviour of Z and G will be derived analytically.

To this end we start with the ghost equation in the form (4.13) where the angle approximation has already been used. The left hand side of the equation does essentially depend only on the product ZG which must behave like

$$ZG(x) \sim x^{\kappa} \quad \text{for} \quad x \to 0 \tag{4.53}$$

in the deep infrared. The power κ might be zero or nonzero. However, if it is zero then one cannot avoid logarithmic singularities in (4.13) that would occur in the limit $x \to 0$. The special case that $\kappa = 0$ would imply that ZG becomes constant in the IR; in this case the ghost equation (4.13) necessitates that G becomes negative for small momenta. This, however, would then conflict with the corresponding 'wrong-statistics-sign' of the ghost propagator. Therefore one has to conclude that $\kappa = 0$ does not lead to an acceptable solution. This also gives a possible answer as to why the constant in the subtracted ghost equation (4.19) has to be zero; if it were not, then it would lead to the same conclusion that have been drawn for the case that $\kappa = 0$.

We proceed assuming that $\kappa \neq 0$ and the ghost equation (4.13) immediately tells that

$$G(x) \to \left(g^2 \gamma_0^G \left[\frac{1}{\kappa} - \frac{1}{2} \right] \right)^{-1} c^{-1} x^{-\kappa} \quad \text{and} \tag{4.54}$$

$$Z(x) \to \left(g^2 \gamma_0^G \left[\frac{1}{\kappa} - \frac{1}{2} \right] \right) \, c^2 x^{2\kappa} \tag{4.55}$$

for $x \to 0$. Hereby $\gamma_0^G = (1/(16\pi^2))(3N_c/4)$ is the leading coefficient of the anomalous dimension of the ghost field. For the reasons that have been discussed above we assume that $G(x)$ is positive for all $x > 0$ and that $Z(x)$ is positive in the infrared; the integral in (4.13) then yields the constraint that

$$0 < \kappa < 2 \, . \tag{4.56}$$

Up to now all results have been obtained using only the ghost DSE, i.e. the leading IR behaviour (4.54), (4.55) and the constraint (4.56) will remain unchanged irrespective of the contributions to the gluon DSE.

One now substitutes these results in the gluon DSE (4.25). Looking at the various contributions one finds that the ghost loop behaves like $\sim x^{-2\kappa}$ in the deep infrared whereas the gluon loop contributes $\sim x^{\kappa}$ for small momenta, i.e. the gluon loop is very subleading in the infrared. This has to be compared to the Mandelstam approximation where the ghost degrees of freedom are neglected which thus yields a completely different qualitative behaviour of the gluon self energy [HvSA98]. Substituting the leading IR behaviour (4.54), (4.55) for the functions Z and G in the gluon DSE (4.25) we find that

$$Z(x) \to g^2 \gamma_0^G \frac{9}{4} \left(\frac{3}{2} \frac{1}{2-\kappa} - \frac{1}{3} + \frac{1}{4\kappa} \right)^{-1} c^2 x^{2\kappa} \, . \tag{4.57}$$

Comparing the coefficients of the two solutions (4.57) and (4.55) one finds that

$$\left(\frac{3}{2}\frac{1}{2-\kappa}-\frac{1}{3}+\frac{1}{4\kappa}\right)=\frac{9}{4}\left(\frac{1}{\kappa}-\frac{1}{2}\right) \quad \Rightarrow \quad \kappa=\frac{61\pm\sqrt{1897}}{19}\,. \tag{4.58}$$

One of the two solutions for κ has to be discarded because of the constraint (4.56) thus giving the unique solution

$$\kappa=\frac{61-\sqrt{1897}}{19}\approx 0.92\,. \tag{4.59}$$

Please note that this result for the power κ has again be derived using only the leading IR divergence in the gluon DSE which is due to the ghost loop only. Any other term that is subleading in the infrared (i.e. that is less divergent than $x^{-2\kappa}$) cannot influence these conclusions. This will be used when the quark loop contribution to the gluon DSE is discussed in chapter 5. It is interesting to note that using bare vertices instead of the nonperturbative ones that are employed in the present approach one finds that $\kappa\approx 0.7$ [AB98b],[AB98a].

The leading infrared behaviour of Z and G which is given by (4.54), (4.55) together with the result for the power κ (4.59) determine also the IR behaviour of the running coupling:

$$g^2Z(k^2)G^2(k^2)\to\bar{g}^2(t(k),g)\to\left(\gamma_0^G\left[\frac{1}{\kappa}-\frac{1}{2}\right]\right)^{-1}=:g_c^2 \tag{4.60}$$

for $k^2\to 0$. Using the explicit value (4.59) one finds that $g_c^2\approx 119.1$ which corresponds to $\alpha_c=g_c^2/(4\pi)\approx 9.48$.

The leading order infrared analysis has been done using the DSEs for Z and G. Equally well one could have started with the corresponding equations for F and R which are related to Z and G via (4.50). However, the results can of course be directly translated and one finds:

$$F(x)\to a=\beta_0 g_c^2 \quad \text{and} \quad R(x)\to bx^\kappa \tag{4.61}$$

for $x\to 0$. This implies that the infrared limit of F depends (via β_0) on the number of flavours N_f. Since $g_c^2\approx 119.1$ one finds that the IR limit of F ranges between $a=8.29$ for $N_f=0$ and $a=5.28$ for $N_f=6$.

This leading order infrared analysis could now be extended using for $x\to 0$ the expansions

$$\begin{aligned}
F(x)&=a\sum_{l,m,n=0}^{\Sigma=N} D_{lmn}\cdot x^{m\nu+n3\kappa+l(1+2\kappa)}\\
&=a\left(1+D_{010}x^\nu+D_{100}x^{1+2\kappa}+D_{001}x^{3\kappa}+\dots\right) \quad \text{and}\\
R(x)&=x^\kappa b\sum_{l,m,n=0}^{\Sigma=N} C_{lmn}\cdot x^{m\nu+n3\kappa+l(1+2\kappa)}\\
&=x^\kappa b\left(1+C_{010}x^\nu+C_{100}x^{1+2\kappa}+C_{001}x^{3\kappa}+\dots\right)
\end{aligned} \tag{4.62}$$

for F and R. These expansion are then substituted into the gluon- and ghost DSEs; then one can compare the coefficients of the IR diverging contributions and can thus derive a system of equations for the coefficients. The solution of this system of equations then gives the power ν and the coefficients C_{lmn} and D_{lmn}. This extended infrared analysis which takes into account the leading as well as the subleading terms in the IR is necessary if the gluon equation is separated again after it has been subtracted. Because otherwise there would be a one parameter family of solutions to this separated gluon equation and the iterative procedure would yield ambiguitive results. This is linked to the fact the this extended infrared analysis unavoidably contains one *undetermined* parameter t which is *not fixed* by the system of equations for the power ν and the coefficients C_{lmn} and D_{lmn}. This is not a deficiency of the IR analysis but it simply corresponds to the fact that only one renormalization condition has been used, thus leaving a one parameter family of solutions.

In short: from a technical point of view one could say that the leading order IR analysis is necessary to allow for stable numerical results while the extended IR analysis is only necessary for the subtracted and again separated gluon equation where it effectively implements the second renormalization condition.

If the subtracted but not again separated form ((4.31) or (4.71)) of the gluon DSE is used for the calculations than this extended infrared analysis is not necessary since the condition (4.75) (see next section) is used to select one of the solutions out of the one–parameter family.

4.5 Scale Invariant Representation

In the last section the nonperturbative definition of the running coupling has been discussed. This lead to the representation (4.50) of the renormalization functions Z and G of the gluon- and the ghost-propagator respectively. The relation (4.50) defines the functions F and R and the DSEs for the gluon (4.25) and the ghost (4.15) can of course be rephrased in terms of F and R. But this section will not just give the corresponding translations of the equations in section 4.2; the results of the discussion concerning the nonperturbative running coupling, the renormalization and the infrared (IR) analysis will allow to elaborate on this.

Using (4.50) one obtains for the ghost equation (4.15)

$$\frac{R(x)}{F^{\delta}(x)} = \tilde{Z}_3 - \delta\left(\frac{1}{2}R(x)F^{1-\delta}(x) + \int_x^L \frac{dy}{y}R(y)F^{1-\delta}(y)\right) \tag{4.63}$$

where L and x the cutoff and the external momentum in units of the scale σ. In order to obtain this equation it has been used that

$$\begin{aligned}\frac{g^2}{16\pi^2}\frac{3}{4}N_c F(s)^{-1} &= \left(\frac{\beta_0 N_c}{48\pi^2}g^2\right)F(s)^{-1}\frac{9}{44-8N_f/N_c} \\ &= \frac{9}{44-8N_f/N_c} \\ &= \delta\end{aligned} \tag{4.64}$$

with $\beta_0 = 11 - 2N_f/N_c$ and . We can now again subtract the DSE (4.63) at the renormalization point $s = \mu^2/\sigma$ in order to eliminate the cutoff dependence. This yields

$$\frac{R(x)}{F^\delta(x)} - \frac{R(s)}{F^\delta(s)} = \bar{\Sigma}_G(x) - \bar{\Sigma}_G(s) \tag{4.65}$$

where the abbreviation

$$\bar{\Sigma}_G(x) = \left(-\frac{1}{2} R(x) F^{1-\delta}(x) + \int_0^x \frac{dy}{y} R(y) F^{1-\delta}(y) \right) \tag{4.66}$$

has been used. (The bar over Σ is meant to distinguish (4.17) and (4.66).)

The infrared analysis yields that F and R behave in the IR according to

$$F \to a \quad \text{and} \quad R \to b x^\kappa \,. \tag{4.67}$$

Using this analytically known IR behaviour we can determine the IR limit of $\bar{\Sigma}_G(x)$ and find that

$$\bar{\Sigma}_G(x) \to 0 \quad \text{for} \quad x \to 0 \tag{4.68}$$

as it must be the case if G is IR divergent. However, this entails some immediate consequences for the renormalization of the ghost DSE. The preliminary analysis in section 4.2 lead to the conclusion that, in principle, there is an (arbitrary) constant in the ghost equation (compare (4.19)). There it has been discussed that in general there is no reason to set this constant equal to zero; even more: it might be impossible to set this constant consistently equal to zero. However, the IR analysis tells that $c(\mu^2) = 0$ for $\mu^2 = 0$, i.e. it is completely legitimate to use $c = 0$ in the ghost equation and it corresponds to the renormalization point $\mu^2 = 0$. (See also the discussion in section 4.4 where it has been argued that c is zero because otherwise log-terms would appear in the ghost equation which would then lead to inconsistencies.) The IR divergent behaviour of the ghost propagator is a direct consequence of $c = 0$. On the other hand, the Kugo–Ojima confinement criterion [Kug95] is linked to the the basic fact that the ghost propagator is IR enhanced (as compared to a simple pole). This strongly suggests that $c = 0$ is the only consistent possibility which is also supported by the work [WA01].

One can now use the definition of F and R (4.50) to rewrite the gluon DSE in terms of these functions. The pendant of equation (4.25) is

$$\begin{aligned}
\frac{F^{1-2\delta}(s)}{R^2(x)F^{1-2\delta}(x)} = Z_3 + Z_1 \frac{g^2}{16\pi^2}\frac{N_c}{3} \Bigg(& \int_0^x \frac{dy}{x} \Big(\frac{7}{2}\frac{y^2}{x^2} - \frac{17}{2}\frac{y}{x} - \frac{9}{8}\Big) R(y) \Big(\frac{F(x)}{F(s)}\Big)^{1-\delta} \\
& + \int_x^L \frac{dy}{y} \Big(\frac{7}{8}\frac{x}{y} - 7\Big) R(y) \Big(\frac{F(x)}{F(s)}\Big)^{1-\delta} \Bigg) \\
+ \frac{g^2}{16\pi^2}\frac{N_c}{3} \Bigg(& \frac{3}{2} \Bigg(\frac{F^\delta(x)}{R(x)} \int_0^x \frac{dy}{x}\frac{y}{x} \frac{F^\delta(y)F^\delta(x)}{R(y)R(x)} - \frac{1}{3}\frac{F^{2\delta}(x)}{R^2(x)} + \frac{1}{2}\int_x^L \frac{dy}{y} \frac{F^{2\delta}(y)}{F^{2\delta}(s)R^2(y}} \Bigg) \,.
\end{aligned} \tag{4.69}$$

The renormalization constant Z_1 multiplies the contributions of the 3-gluon-vertex. The correct scaling behaviour for Z_3 would be $Z_3 = (F(s)/F(L))^{1-2\delta}$. Using the scaling behaviour of $\tilde{Z}_3 = (F(s)/F(L))^{\delta}$ this then would imply (via the STI $Z_1 = Z_3/\tilde{Z}_3$) that $Z_1 = (F(s)/F(L))^{1-3\delta}$ thus violating $Z_1 = 1$. However, this would introduce additional scale and cutoff dependence in the gluon DSE. And especially the cutoff dependence leads to ultraviolet diverging contributions from the the 3-gluon loop if $1 - 3\delta > 0$. This would be the case for $N_f < 7$ and this divergence could not be absorbed in any way.

Therefore, in the present scheme it is not possible to impose both at the same time: the Landau gauge identity $Z_1 = Z_3/\tilde{Z}_3$ and the correct leading log behaviour which is known from perturbation theory. Therefore it seems that the STI $Z_1 = Z_3/\tilde{Z}_3$ has to be abandoned in the present approach.(It can be shown that it does not lead to consistent alternatives to abandon the correct anomalous dimensions [vS98].)

While it is in principle possible to use $Z_1 = 1$ this would not yield the correct perturbative behaviour of the renormalization functions while it would not alter the IR behaviour of the solutions. In order to reproduce the correct short-distance behaviour one has to retain the scale dependence of Z_3. A reasonable resolution to the conflicting constraints on the scale and the cutoff-dependence can be obtained by setting

$$Z_1 = \left(\frac{F(s)}{F(y)}\right)^{1-3\delta} \tag{4.70}$$

where y is the loop momentum in units of the scale σ.

Having discussed this additional problem we can now proceed and can again subtract the equation at the renormalization point $s = \mu^2/\sigma$ which eliminates all pure constants in the equation. However, the gluon equation does contain one term where the cutoff-dependence cannot be eliminated since it does depend on the external scale. Using manipulations which are quite similar to those that lead from (4.25) to (4.31) we find

$$\frac{1}{R^2(x)F^{1-2\delta}(x)} - \frac{1}{R^2(s)F^{1-2\delta}(s)} = \bar{\Sigma}(x) - \bar{\Sigma}(s) \tag{4.71}$$

where $\bar{\Sigma}(x)$ is defined as

$$\begin{aligned}\bar{\Sigma}(x) = \frac{1}{11}\Bigg[&\int_0^x \frac{dy}{x}\Big(\frac{7}{2}\frac{y^2}{x^2} - \frac{17}{2}\frac{y}{x} - \frac{9}{8} + 7\frac{x}{y}\Big)R(y)F^{2\delta}(y) \\ &+ x\frac{7}{8}\int_x^L \frac{dy}{y^2}R(y)F^{2\delta}(y)\Bigg] + \frac{1}{11}\Bigg[\frac{3}{2}\left(\frac{F^{\delta}(x)}{R(x)}\int_0^x \frac{dy}{x}\frac{y}{x}\frac{F^{\delta}(y)}{R(y)}\right) \\ &- \frac{1}{3}\left(\frac{F^{2\delta}(x)}{R^2(x)}\right) - \left(\frac{1}{2}\int_0^x \frac{dy}{y}\Big(\frac{F^{2\delta}(y)}{R^2(y} - \frac{a^{2\delta}}{b^2y^{2\kappa}}\Big) + \frac{1}{4\kappa}\frac{a^{2\delta}}{b^2x2\kappa}\right)\Bigg] .\end{aligned} \tag{4.72}$$

The only formal cutoff dependence that remains is contained in the term

$$x\frac{7}{8}\int_x^L \frac{dy}{y^2}R(y)F^{2\delta}(y) \tag{4.73}$$

and it cannot be absorbed using a subtractive scheme since it is multiplied by the external scale x. Terms of this kind can in principle only be renormalized using multiplicative renormalizability. However, please note that this term is finite in the limit $L \to \infty$ and therefore there is no need to renormalize it.

It has already been discussed that the equation in the subtracted form (4.71) cannot be separated again into two equations, see the discussion in section 4.2. For the ghost equation it could be argued that the constant that consists of all the μ-dependent terms can be set to zero which in that case corresponds to the renormalization point $\mu = 0$. The reason for this being that $\bar{\Sigma}_G$ goes to 0 in the infrared. This is different for the gluon DSE. The latter contains the ghost-loop contributions which go like $x^{-2\kappa}$ and thus are highly divergent in the IR. This entails that one can neither conclude nor exclude that

$$\frac{1}{R^2(s)F^{1-2\delta}(s)} - \bar{\Sigma}(s) = 0 \tag{4.74}$$

is a consistent possibility.

The value of

$$\frac{1}{R^2(s)F^{1-2\delta}(s)} = \text{const.} \tag{4.75}$$

is not fixed by the DSE and has to be supplemented as an additional constraint which effectively incorporates the second renormalization condition (besides $ZG^2(\mu) = 1$). Without this second constraint the subtracted equations would allow for a one parameter family of solutions, the parameter being the value of (4.75).

Chapter 5

Dynamical Quarks

This chapter centers on the quark DSE and on the quark loop contribution to the gluon DSE. First the quark DSE is discussed and the projection onto the scalar and vectorial self-energies is done. It is the thus obtained form of the quark DSE that is used to calculate the numerical solutions that are presented in the chapter 6. Following this the quark loop contribution to the gluon DSE is examined. Here the discussion will emphasize the infrared behaviour of the quark loop and especially its renormalization will be discussed in detail. This chapter thus presents all formal ingredients (besides those that have been introduced in section 4.1) that are then used to obtain the results that will be presented in chapter 6.

5.1 The Quark Dyson-Schwinger Equation

The DSE for the quark propagator is given by

$$S^{-1}(p) = Z_2 S_0^{-1}(p) + g^2 Z_{1F} \frac{4}{3} \int \frac{d^4k}{(2\pi)^4} \gamma_\mu S(k) \Gamma_\nu(k,p) D^{\mu\nu}(p-k) \; . \tag{5.1}$$

Here and in the following S denotes the full fermion propagator which in its most general form can be written (for Euclidean momenta)

$$S^{-1}(p) = -i\not{p} A(p^2) + B(p^2) \tag{5.2}$$

thereby introducing the two scalar functions A and B which are usually called the vectorial and the scalar self-energy respectively. S_0 denotes the bare quark propagator which is obtained from (5.2) by setting $A = 1$ and $B = m_0$.

The full gluon propagator (in Landau gauge) is denoted by

$$D^{\mu\nu}(p) = \left(\delta^{\mu\nu} - \frac{p^\mu p^\mu}{p^2}\right) \frac{Z(p^2)}{p^2} \tag{5.3}$$

$$= \left(\delta^{\mu\nu} - \frac{p^\mu p^\mu}{p^2}\right) \frac{R^2(x)}{p^2} \left(\frac{F(x)}{F(s)}\right)^{1-2\delta} \tag{5.4}$$

where x and s denote the external scale p^2 and the renormalization point μ^2 in units of the scale σ. The parameterization of the gluon renormalization function Z in terms of F and R has been made explicit for later convenience.

In section 4.1 it has been discussed that the present truncation scheme amounts to a simplified STI which has to be used to solve for the quark-gluon vertex. To the extent that the quark-ghost scattering kernel is neglected this identity reads

$$G^{-1}(p^2)k^\mu\Gamma_\mu(p,q) = iS^{-1}(p^2) - iS^{-1}(q^2) \tag{5.5}$$

where the essential difference to the Abelian Ward-Takahashi identity (WTI) is the additional factor $G^{-1}(p^2)$ on the left hand side. However, this additional factor does not change the way one solves the WTI (see the detailed discussion in section 2.3) and the solution correspondingly reads

$$\Gamma_\mu(p,q) = G(k^2)\left(\Gamma_\mu^L + \Gamma_\mu^T\right) = \frac{1}{R(y)}\left(\frac{F(x)}{F(s)}\right)^\delta\left(\Gamma_\mu^L + \Gamma_\mu^T\right). \tag{5.6}$$

Hereby the contributions Γ^L and Γ^T refer to the longitudinal (Ball-Chiu [BC80a], [BC80b]) and transverse (Curtis-Pennington [CP90]) part of the full vertex as specified in (2.32) and in (2.37) respectively. The F, R-dependence has been made explicit in (5.6) for later convenience.

It is to be noted that the longitudinal contribution Γ^L (i.e. the Ball-Chiu part of the vertex) alone would give rise to logarithmic divergences in the quark DSE. These would then have to be absorbed in Z_2 thus leading to $Z_2 \neq 1$. The transverse CP–contribution assures that these logarithmic divergences are cancelled thus giving $Z_2 \to 1$. This has been shown for the case of QED_4. For the present truncation scheme this implies that the ghost factor G has to multiply the BC and the CP part in the same way.

From the identity $Z_{1F} = \tilde{Z}_3^{-1}$ and from the scaling behaviour of $\tilde{Z}_3$ we find that in Landau gauge one would have

$$Z_{1F} = \left(\frac{F(L)}{F(s)}\right)^\delta \to 0 \quad \text{for} \quad L \to \infty \tag{5.7}$$

where L and s denote again the UV cutoff and the renormalization point in units of the scale σ. This cutoff dependence of the vertex renormalization constant would make the self-energy contributions to the quark propagator equal to zero in the limit that $L \to \infty$.

This is very much the same problem that has already been encountered for the renormalization constant Z_1; there we also found that the cutoff dependence of Z_1 could not be cancelled in any way. Therefore it seems necessary to use the same prescription as for Z_1 or more precisely:

$$Z_{1F} = \left(\frac{F(y)}{F(s)}\right)^\delta \tag{5.8}$$

where y denotes the loop momentum in units of σ. At present this has the status of an additional prescription which is necessary at the current level of truncation.

Using this prescription for Z_1 one can write the quark DSE in the form

$$S^{-1}(p) = Z_2 S_0^{-1}(p) + Z_{1F}\frac{4}{3\beta_0}\int\frac{d^4k}{(2\pi)^4}\gamma_\mu S(k)\left(\Gamma^L_\mu + \Gamma^T_\mu\right) \left(\delta^{\mu\nu} - \frac{q^\mu q^\mu}{q^2}\right)\frac{F(q^2/\sigma)R(q^2/\sigma)}{q^2} \quad (5.9)$$

with $q = p - k$ and where the relation $g^2(s) = F(s)/\beta_0$ has been used.

For the numerical solution it is advantageous to first transform the quark DSE in the form (5.1) to a coupled system of equations for the self-energies A and B which have been defined in (5.2). This yields the following system of equations:

$$\begin{aligned} A(p^2) = Z_2 + Z_{1F}\frac{4}{3\beta_0}\int\frac{d^4q}{(2\pi)^4}\frac{F(k^2/\sigma)R(k^2/\sigma)}{k^2(q^2A^2(q^2)+B^2(q^2)}& \\ \left(\frac{1}{2}\left[3(p^2+q^2)\langle p,q\rangle - 2p^2q^2(1+2z^2)\right]\frac{1}{k^2}\big(A(p^2)+A(q^2)\big)A(q^2)\right.& \\ - \big[p^2q^2(p^2+q^2)\big)\frac{1}{k^2}\Delta A(p,q)A(q^2) - 2\big[p^2q^2\big)\frac{1}{k^2}\Delta B(p,q)B(q^2)& \\ \left. + \frac{3}{2}\langle q,p\rangle\Omega(p,q)(A(p^2)-A(q^2))A(q^2)\right)\,, \quad (5.10)& \end{aligned}$$

$$\begin{aligned} B(p^2) = Z_2Z_m m + Z_2\frac{4}{3\beta_0}\int\frac{d^4q}{(2\pi)^4}\frac{F(k^2/\sigma)R(k^2/\sigma)}{k^2(q^2A^2(q^2)+B^2(q^2)}& \\ \left(\frac{3}{2}(A(p^2)+A(q^2))B(q^2) + 2\big(p^2q^2-\langle p,q\rangle^2\big)\frac{1}{k^2}\Delta A(p,q)B(q^2)\right.& \\ - 2\big(p^2q^2-\langle p,q\rangle^2\big)\frac{1}{k^2}\Delta B(p,q)A(q^2)& \\ \left. + \frac{3}{2}\Omega(p,q)(A(p^2)-A(q^2))A(q^2)\right)\,. \quad (5.11)& \end{aligned}$$

For the gluon- and the ghost DSE a specific one-dimensional approximation has been used to investigate the behaviour of the renormalization functions Z and G in the deep infrared. Note that the one-dimensional approximation is necessary in order to allow for the analytic infrared analysis. The specific angle approximation that has been used has been explicitely constructed to maintain the behaviour for infrared as well as for ultraviolet momenta. It turns out that the quark DSE is different. The equation for A is assumed to be the most interesting of the two self-energies A and B of the quark. This is because B is in a sense fixed by the pattern of chiral-symmetry breaking. Therefore one could argue that any confinement signature has to be found in A. Using the same procedure as for the gluon- and ghost DSE one would employ a one-dimensional approximation for the gluon renormalization function Z and for any nonperturbative ingredient that might enter due to the vertex. However, one finds that any one dimensional approximation that neglects the

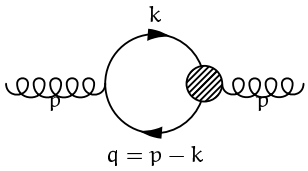

Figure 5.1: Momentum Routing for the quark-loop contribution to the gluon DSE.

angular dependence will result in $A(p^2) = 1$ for all momenta p^2. I.e. in the quark equation all information on the value of

$$\lim_{p^2 \to 0} \left(A(p^2) - 1 \right) \tag{5.12}$$

is contained in the angular dependence of $Z(q^2)$ as it enters the DSE for A due to its dependence on the gluon propagator. While the infrared limit of A is therefore not known analytically the results to be presented later (see chapter 6) will show that A becomes constant in the infrared. Any possible divergence (e.g. of A in the IR) would definitely spoil the stable numerical solution that is found. Therefore one can conclude that in the present truncation scheme A becomes constant in the infrared. The results that are discussed in chapter 6 also show that B becomes constant in the infrared.

5.2 Quark-Loop Contribution to the Gluon DSE

Up to now the effect of the quark-loop in the DSE for the gluon propagator has been neglected. In this and the following sections the quark loop and especially its renormalization are discussed in detail. The qualitative influence on the results for the gluon- and ghost renormalization functions is discussed. To this end the infrared limit of the quark loop is derived and put into relation with the renormalization scheme.

The contribution of the quark-loop to the DSE for the gluon propagator $D^{-1}_{\mu\nu}$ is depicted in fig. 5.1 and it given by

$$-g^2 Z_{1F} \frac{N_f}{2} \Pi_{\mu\nu}(p) \tag{5.13}$$

where Z_{1F} is the vertex renormalization constant and N_f is the number of quark flavours. The polarization is explicitely defined as

$$\Pi_{\mu\nu} = -g^2 T_F \int \frac{d^4k}{(2\pi)^4} \mathrm{tr}\left(\gamma_\mu S(k) \Gamma_\nu(k,q) S(q) \right) \tag{5.14}$$

where $q = p - k$. The colour matrix δ^{ab} has been factored out and T_F is the colour trace. The vertex Γ_ν is the full quark-gluon vertex in Landau gauge. As such it is the solution of its

own STI, see the discussion in section 4.1 and in the preceding section. The solution of the approximate STI which neglects the quark-ghost scattering kernel gives (5.6). In the present approach we neglect the subleading contributions of the vertex and retain only its dominant structure. For QED_3 it has been explicitely verified that the subleading components of (5.6) do change the results by less than 5% (even in the vicinity of the phase transition). Since the results for the quark propagator (those for QED_3 and those that will be presented in chapter 6) are very similar in the sense that A and B become both constant in the infrared it can be safely assumed that the contribution of the subleading components will be of the order of 5% or less also for the case of QCD. In this approximation the vertex explicitely reads

$$\Gamma_\nu(k,q) = \frac{G(p)}{2}\big(A(k)+A(q)\big)\gamma_\nu \ . \tag{5.15}$$

This vertex contains the multiplicative ghost-factor G which enters via the solution of the approximate STI (5.5) and which is the primary difference between the quark-gluon vertex in Landau-gauge QCD and the electron-photon vertex in QED. Besides being the dominant contribution to the vertex, the approximate form (5.15) also has the correct perturbative limit.

As has been discussed in section 4.1; the gluon renormalization function Z is extracted by applying the projector

$$R^{\mu\nu} = \delta^{\mu\nu} - 4\frac{k^\mu k^\nu}{k^2} \tag{5.16}$$

to the gluon DSE for the inverse propagator $D^{-1}_{\mu\nu}$. In order to derive the quark-loop contribution to the DSE for the renormalization function Z we have to apply the same projector the polarization (5.14). This yields:

$$R^{\mu\nu}(k)D^{Gluon}_{\mu\nu}(k) = 3k^2/Z(k^2) \qquad \text{and} \tag{5.17}$$

$$R^{\mu\nu}(k)\Pi\mu\nu(k) = R^{\mu\nu}(k)\Big(k^2\delta_{\mu\nu} - k_\mu k_\nu\Big)\Pi(k) = 3k^2\Pi(k) \tag{5.18}$$

where the polarization scalar Π is defined as:

$$\Pi(p) = -\frac{1}{3p^2}\int\frac{d^4k}{(2\pi)^4}R^{\mu\nu}(p)\mathrm{tr}\big(\gamma_\mu S(k)\big[\frac{G(p)}{2}\big(A(k)+A(q)\big)\gamma_\nu\big]S(q)\big) \ . \tag{5.19}$$

Now we can write the full gluon DSE for the gluon renormalization function Z with the quark-loop contribution included:

$$\begin{aligned}\frac{1}{Z(k^2)} = Z_3 + Z_1\frac{g^2N_c}{48\pi^2}\Bigg(&\int_0^{k^2}\frac{dq^2}{k^2}\left[\frac{7}{2}\frac{q^4}{k^4} - \frac{17}{2}\frac{q^2}{k^2} - \frac{9}{8}\right]Z(q^2)G(q^2) \\ &+ \int_{k^2}^{\Lambda^2}\frac{dq^2}{q^2}\left[\frac{7}{8}\frac{k^2}{q^2} - 7\right]Z(q^2)G(q^2)\Bigg) \\ + \frac{g^2N_c}{48\pi^2}\Bigg(&\frac{3}{2}G(k^2)\int_0^{k^2}\frac{dq^2}{q^2}\frac{q^2}{k^2}G(q^2) - \frac{1}{3}G^2(k^2) + \frac{1}{2}\int_{k^2}^{\Lambda^2}\frac{dq^2}{q^2}G^2(q^2)\Bigg) \\ &- g^2Z_{1F}\frac{N_f}{2}\Pi(p) \ .\end{aligned} \tag{5.20}$$

This form of the gluon DSE relies on the the angle-approximation (see section 4.1) which is used for everything but the quark-loop contribution. In this form the equation still contains the renormalization constant Z_1 and the prescription (4.70) has been used in order to obtain the correct scaling behaviour.

The gluon DSE (5.20) can now be translated into an equation for F, R using the relation (4.50). This equation can then be subtracted at the renormalization point μ^2 to give the extended form of (4.71) which does now also contain the quark-loop contribution

$$\frac{1}{R^2(x)F^{1-2\delta}(x)} - \frac{1}{R^2(s)F^{1-2\delta}(s)} = \left(\bar{\Sigma}(x) - g^2 Z_{1F} F^{1-2\delta}(s)\frac{N_f}{2}\Pi(p)\right) - \left(\bar{\Sigma}(s) - g^2 Z_{1F} F^{1-2\delta}(s)\frac{N_f}{2}\Pi(p)\right) \quad (5.21)$$

where $\bar{\Sigma}$ is defined in (4.72). In this subtraction step all cutoff dependence should have been cancelled and only cutoff independent terms should remain. However, one has to keep in mind that a subtractive renormalization scheme will only work if all cutoff dependent terms appear as pure constants (independent of the external scale x). We will investigate whether this is the case for the quark-loop.

In the following sections we will discuss the renormalization of the quark loop. It will turn out that its infrared behaviour cannot be disentangled from the renormalization prescription that is used. Therefore it is advantageous and necessary to first derive the behaviour of the quark loop in the deep infrared. To this end we need a more explicit expression of the polarization scalar Π.

In order to find a more explicit expression of the polarization scalar (5.19) one has to evaluate the trace and the projection;

$$R^{\mu\nu}(p)\mathrm{tr}\big(\gamma_\mu[\not{k}A(k)^2 + B(k)^2]\gamma_\nu[\not{q}A(q)^2 + B(q)^2]\big) = 4\big(-2k^2 - 6\langle p,k\rangle + \frac{8}{p^2}\langle p,k\rangle^2\big)A(k)A(q) \quad (5.22)$$

using this we obtain:

$$\Pi(p) = \frac{1}{3p^2}2G(p)\frac{4\pi}{(2\pi)^4}\int dk^2\, k^2 \sigma_\nu(k) I(p,k) \quad (5.23)$$

with the angular integral

$$I(p,k) = \int_{-1}^{+1} dz\, \sqrt{1-z^2}\big(A(k) + A(q)\big)\sigma_\nu(q)\big(k^2 + 3pkz - 4k^2z^2\big) \quad (5.24)$$

and the abbreviation

$$\sigma_\nu(k) = \frac{A(k)}{k^2A^2(k^2) + B^2(k^2)}\ . \quad (5.25)$$

Hereby we used the definition that $z = \cos(\theta)$ where θ is the angle between the Euclidean four vectors p and k.

5.3 Infrared Behaviour of the Quark Loop

The analytic infrared analysis of the coupled system of DSEs for the gluon- and ghost-propagator (see section 4.4) revealed important information on the solutions. First it was found that the nonperturbative running coupling does have an infrared fixed point. This IR behaviour of the running coupling has been found using only the leading IR behaviour of the gluon- and ghost renormalization functions Z and G. Therefore it is of course interesting to see whether this leading IR behaviour of the renormalization functions (and thus the IR fixed point of the running coupling) is changed qualitatively by the inclusion of the quark-loop. For the gluon–ghost system it has been found that the leading contribution in the IR comes from the ghost-loop in the gluon DSE and that it behaves like $x^{-2\kappa}$ with $\kappa \approx 0.92$. This gives rise to the next question: Does the inclusion of the quark loop change the value of κ?

In order to answer these questions we have to find an analytic expression for the IR behaviour of the quark loop. Assuming that $p^2 \to 0$ we can simplify the angular integral (5.24) since in this limit

$$A(q) \approx A(q_>) \quad \text{and} \quad \sigma_v(q) \approx \frac{1}{A(q_>)} \frac{1}{q^2 + M^2(q_>)} \tag{5.26}$$

with the abbreviation $q_> = \max(p^2, k^2)$. (Here we assumed that A and B will become constant in the deep infrared; an assumption that will be shown to be justified once the complete numerical solution has been discussed.) Using these approximate expressions for A and σ_v we can evaluate the angular integral (5.24) and find

$$\begin{aligned} I(p,k) = \frac{A(k) + A(q_>)}{A(q_>)} \frac{\pi}{2pk} \Bigg(& k^2 \big[\alpha - \sqrt{\alpha^2 - 1}\big] \\ & - 4k^2 \alpha \big[\alpha^2 - \frac{1}{2} - \alpha\sqrt{\alpha^2 - 1}\big] + 3pk \big[\alpha^2 - \frac{1}{2} - \alpha\sqrt{\alpha^2 - 1}\big] \Bigg) \end{aligned} \tag{5.27}$$

where

$$\alpha = \frac{p^2 + k^2 + M^2(q_>)}{2pk} \tag{5.28}$$

Since we consider the limit that $p^2 \to 0$ it follows that α is very large (anticipating that $M^2(q_>) > 0$). This allows to expand the result (5.27) in powers of $1/\alpha$. Using the expansions (for $\alpha \gg 1$)

$$\alpha - \sqrt{\alpha^2 - 1} = \frac{1}{2\alpha} + \frac{1}{8\alpha^3} + \frac{1}{16\alpha^5} + \dots \tag{5.29}$$

$$\alpha^2 - \frac{1}{2} - \alpha\sqrt{\alpha^2 - 1} = \frac{1}{8\alpha^2} + \frac{1}{16\alpha^4} + \dots \tag{5.30}$$

one finds that the leading power of the first and the second contribution to (5.27) cancels. The result of this expansion can then be expanded in powers of p^2 and thus yields the infrared behaviour of the quark loop.

Putting everything together one finds that the polarization scalar (5.23) behaves in the deep infrared like

$$\Pi(p) \to G(p)\frac{1}{4\pi^2}\left(\Pi_0 + \Pi_1 \cdot p^2\right) \quad \text{for} \quad p^2 \to 0 \tag{5.31}$$

with

$$\Pi_0 = \frac{2}{3}\int_0^{\Lambda^2} dk^2 \frac{k^4 \sigma_v(k)}{(k^2 + M^2(k^2))^2}\left[\frac{3}{2} - \frac{k^2}{k^2 + M^2(k^2)}\right] \tag{5.32}$$

$$\Pi_1 = \int_0^{\Lambda^2} dk^2 \frac{k^6 \sigma_v(k)}{(k^2 + M^2(k^2))^4}\frac{A(k) + A(q_>)}{A(q_>)}\left[1 - \frac{k^2}{k^2 + M^2(k^2)}\right] \tag{5.33}$$

This shows that the quark loop in the gluon DSE behaves in the deep infrared like the ghost renormalization function G which entered the quark loop via the quark-gluon vertex. The IR behaviour of the quark loop is thus a consequence of the approximate STI that gave this vertex. For $N_f = 0$ it has been found (see section 4.4) that the ghost renormalization function G behaves like $x^{-\kappa}$ in the infrared. For the gluon DSE that immediately implies that the ghost loop ($\sim x^{-2\kappa}$) is still the dominant contribution in the infrared. In short: the quark loop is subleading in the infrared.

The conclusions concerning the leading IR behaviour of the gluon- and ghost renormalization functions Z and G that have been drawn in section 4.4 rely only on the leading IR divergent contribution; i.e. on the fact that the ghost loop is the dominant contribution in the infrared. Since this is not altered by the inclusion of the quark loop we find the result that also for $N_f > 0$ one has in Landau gauge

$$Z \to x^{2\kappa} \quad \text{and} \quad G \to x^{-\kappa} \tag{5.34}$$

for small momenta. I.e. also with quarks included we find that the ghost propagator G is infrared enhanced (as compared to the perturbative simple pole) and the gluon renormalization function Z is infrared vanishing, leading to an IR suppressed gluon propagator.

The infrared analysis in section 4.4 showed that also the value κ does depend only on the leading IR divergence in the gluon DSE. This immediately implies that the value of κ is not altered by the inclusion of the quark loop. I.e. also for $N_f > 0$ one still has that $\kappa \approx 0.92$. This result together with (5.34) says that the leading IR behaviour of the gluon- and the ghost renormalization functions Z and G is not affected in any way by the inclusion of the quark loop in the gluon equation.

This leading IR behaviour of Z and G then immediately implies that the nonperturbative running coupling

$$g^2 Z G^2 = \frac{1}{4\pi\beta_0} F \tag{5.35}$$

has an infrared fixed point also for $N_f > 0$. The infrared analysis in section 4.4 showed that the IR limit of F depends on N_f corresponding to

$$F(x) \to a(N_f) \quad \text{with} \quad \frac{a(N_f > 0)}{\beta_0(N_f > 0)} = \frac{a(N_f = 0)}{\beta_0(N_f = 0)} \tag{5.36}$$

and this result does again rely solely on the leading IR divergence in the gluon DSE; i.e. on the fact that the ghost loop is dominant in the infrared. Since this remains valid after the inclusion of the quark loop we find that even the value of the IR fixed point is not altered by the quark loop, it does not depend on the number of quark flavours N_f.

In summary: for $N_f > 0$ we found that the leading IR behaviour of the gluon- and the ghost propagator is not different from the case $N_f = 0$. This highlights the importance of ghosts; the ghost-loop gives the leading contribution in the infrared and thus results in an IR vanishing gluon propagator and an IR enhanced ghost propagator. This in turn already ensures that the Kugo-Ojima confinement criterion [Kug95],[WA01] is satisfied. This conclusion does therefore rest solely on the ghosts and is not altered by the quark loop.

5.4 Renormalization of the Quark Loop

The present section centers on the renormalization of the quark–loop contribution to the gluon DSE. First we will discuss the general aspects and constraints that have to be taken into account. Following this two possibilities for the renormalization of the quark–loop are examined.

In section 5.3 the infrared behaviour of the quark loop has been derived. We found that it behaves like

$$\Pi(p) \to G(p)\frac{1}{4\pi^2}\left(\Pi_0 + \Pi_1 \cdot p^2\right) \tag{5.37}$$

in the infrared where the coefficients Π_0 and Π_1 are given in (5.32) and (5.33). Looking at the UV behaviour of these coefficients we found that Π_0 is logarithmically divergent whereas Π_1 is convergent.

This is one of the reasons why the quark loop is different. The gluonic and the ghost contributions to the gluon DSE are either UV finite or do appear as additive constants in the gluon DSE. This is different for the quark loop; its leading contribution in the infrared is

$$\sim G(p) \cdot \Pi_0 \tag{5.38}$$

which explicitely depends on the external scale p. Neglecting the quark loop all divergencies could be accounted for using a subtractive renormalization scheme. But a subtractive scheme can, of course, only handle additive constants. If the divergent contribution do depend on the external scale than in principle one has to resume to another renormalization scheme.

This also emphasises another difficulty: the renormalization of the quark loop *cannot be disentangled* from its infrared behaviour. Every renormalization scheme that might be used has to account for the log-divergence of the coefficient Π_0 that multiplies the ghost renormalization function G thus influencing the IR behaviour of the quark loop. This has to be kept in mind since usually it is assumed that the infrared behaviour is essentially independent of the UV contributions. This is not true for the quark loop.

The perturbative one–loop scaling of the renormalization constant Z_3 is known to be (see e.g. [Mut87])

$$Z_3 = 1 + \frac{g^2}{16\pi^2}\left(\frac{N_c}{3}(7-\frac{1}{2}) - \frac{4}{3}\frac{N_f}{2}\right)\ln(\frac{\Lambda^2}{\mu^2}) \tag{5.39}$$

And this especially implies that the quark–loop should contribute the logarithmic divergence

$$-\frac{g^2}{16\pi^2}\frac{4}{3}\frac{N_f}{2}\ln(\frac{\Lambda^2}{\mu^2}) \tag{5.40}$$

to Z_3 in the gluon DSE. This has to be compared to the (logarithmically divergent) contribution of the quark–loop to the gluon DSE (5.20); one finds[1]

$$-[(G(p)Z_{1F}]\frac{g^2}{16\pi^2}\frac{4}{3}\frac{N_f}{2}\ln(\frac{\Lambda^2}{\mu^2})\ . \tag{5.41}$$

The quark–loop has the additional factor $[(G(p)Z_{1F}]$ which introduces additional (and unexpected) scale and cutoff dependence as compared to (5.40). Furthermore the ghost renormalization factor $G(p)$ depends on the external scale; this dependence cannot be accounted for and it obviously does not correspond to the expected 1-loop scaling (5.40).

However, in order to correctly reproduce the anomalous dimension of the gluon one would expect that the quark–loop contributes a log-divergence of the form

$$\sim \log(L)^{1-2\delta} \tag{5.42}$$

where $L = \Lambda^2/\mu^2$. This is not satisfied for the quark–loop contribution in (5.20) and it will be shown in the following that the same renormalization prescription that has been used for the quark DSE has to be used for the quark–loop in the gluon DSE in order to resolve this problem. Note that a quite similar problem has already been encountered in the gluon DSE; there the cutoff dependence of the renormalization constant could not be accounted for while its scale dependence was necessary to give the correct overall scale dependence.

In the gluon–ghost system the prescription

$$G(p) = \left(\frac{F(x)}{F(s)}\right)^{\delta}\frac{1}{R(x)} \to \begin{cases} \left(\frac{F(y)}{F(s)}\right)^{\delta}\frac{1}{R(y)} & \text{for } y > x \\ \left(\frac{F(x)}{F(s)}\right)^{\delta}\frac{1}{R(x)} & \text{for } x \leq y \end{cases} \tag{5.43}$$

(where y is the loop momentum) had to be used in order to obtain the correct anomalous dimensions. In order to be consistent with this approximation it is mandatory to employ the same prescription for the quark–loop. This then leads to a modified polarization scalar which can be conveniently written in the way

$$\Pi(p) = \Pi_<(p) + \Pi_>(p) \tag{5.44}$$

[1] Using the known perturbative limits $A(p^2) \to 1$ and $B(p^2) \to m_0$ for $p^2 \to \infty$ one finds for the angle integral (5.24) the limit: $I(p,k) \to (\pi/2)p^2/k^2$ for $k^2 \to \infty$.

where the two contributions $\Pi_<$ and $\Pi_>$ are defined according to

$$\Pi_<(p) = \frac{1}{3p^2} G(p) \frac{8\pi}{(2\pi)^4} \int_0^{p^2} dk^2\, k^2 \sigma_v(k) I(p,k) \;, \tag{5.45}$$

$$\Pi_>(p) = \frac{1}{3p^2} \frac{8\pi}{(2\pi)^4} \int_{p^2}^{\Lambda^2} dk^2\, k^2 \sigma_v(k) I(p,k) G(k) \tag{5.46}$$

and where the angle integral $I(p,k)$ is defined in (5.24). However, a word of caution is in order here. The infrared limit of the quark–loop in the original form was

$$\Pi(p) \to G(p) \frac{1}{4\pi^2} \cdot \Pi_0 \quad \text{for} \quad p^2 \to 0 \tag{5.47}$$

where Π_0 turned out to be logarithmically UV-divergent. This infrared behaviour of the quark–loop has been changed due to the prescription (5.43) which had to be used in order to stay consistent with the gluon–ghost system. The infrared limit of $\Pi_<$ and $\Pi_>$ can be calculated and one finds

$$\Pi_<(p) \to \frac{a^{2\delta}}{3B^2(0)b} \frac{1}{x^\kappa} \left(\frac{1}{2M^2(0)} x^3 + \mathcal{O}(x^4) \right) \quad \sim \quad x^{3-\kappa} \;, \tag{5.48}$$

$$\Pi_>(p) \to \frac{2}{3} \int_0^{\Lambda^2} dk^2 \frac{k^4 \sigma_v(k)}{(k^2 + M^2(k^2))^2} \left[\frac{3}{2} - \frac{k^2}{k^2 + M^2(k^2)} \right] G(k) \tag{5.49}$$

for $p^2 \to 0$. In order to calculate the IR limit of $\Pi_<$ it has been assumed that $B(0)$ and $M(0)$ are nonzero (which will be shown to be satisfied, see chapter 6). This result shows that $\Pi_<$ vanishes for $p^2 \to 0$ while $\Pi_>$ becomes constant in the infrared. And from the discussion up to now it is obvious that this constant is logarithmically divergent.

Having discussed the general aspects we will now examine two possibilities to renormalize the quark–loop. In order to facilitate the following discussion it is advantageous to make the scale dependence of the quark–loop contribution explicit. The ghost renormalization function G contributes $F(s)^{-\delta}$ to the overall scale dependence of the quark–loop and the relation $g^2 = F(s)/\beta_0$ allows to replace the coupling constant. However, if the gluon DSE is to be used in the scale invariant representation in the subtracted form (cf. eq (4.71))

$$\frac{1}{R^2(x) F^{1-2\delta}(x)} - \frac{1}{R^2(s) F^{1-2\delta}(s)} = \bar{\Sigma}(x) - \bar{\Sigma}(s) \tag{5.50}$$

one has to divide by the factor $F^{1-2\delta}(s)$ that in the beginning appears on the left hand side (cf. eq (4.50)). Taking this into account the full scale and cutoff dependence of the quark–loop contribution is

$$-F^\delta(s) Z_{1F} \frac{1}{16\pi^2 \beta_0} \frac{4}{3} \frac{N_f}{2} \ln^{1-\delta}\left(\frac{\Lambda^2}{\mu^2}\right) \;. \tag{5.51}$$

Hereby the prescription (5.43) has been used and the corresponding polarization scalar is therefore defined by (5.44) ($\Pi_<$ and $\Pi_>$ are defined by (5.45) and (5.46)). Two possibilities to renormalize the quark–loop are now examined.

1. In a first attempt one could multiplicatively renormalize the quark–loop contribution to the gluon DSE. In this case it would be necessary to specify the renormalization constant Z_{1F} such that the scale as well as the cutoff dependence of the quark–loop is cancelled multiplicatively. As far as the scale dependence is concerned there is no other possibility than to assume that $Z_{1F} \sim F(s)^{-\delta}$ (cf. eq (5.51)). The constant of proportionality has to be used to cancel the logarithmic divergence of $\Pi_>(0)$ where $\Pi_<$ and $\Pi_>$ are now defined by (5.45) and (5.46) since the prescription (5.55) is not used in this case. The quark–loop has been shown to become constant in the infrared, see eqs (5.48) and (5.49). This constant can be separated into two parts:

$$\lim_{p^2\to 0} \Pi_>(p) = c_0 + c_1 \cdot \log(L)^{1-\delta} \tag{5.52}$$

In a minimal subtraction scheme one would subtract the $\log(L)$ contribution thus leaving the finite constant c_0 such that the renormalized quark loop has the UV-finite infrared limit

$$\lim_{p^2\to 0} \left(\Pi_<(p) + \Pi_>(p) \right) \to c_0 \tag{5.53}$$

Together with the enforced scale dependence this leads to the definition

$$Z_{1F} = \frac{c_0/c_1 \cdot \log(L)^{\delta-1}}{F(s)^\delta} \tag{5.54}$$

for the vertex renormalization constant Z_{1F}. This defines the multiplicative renormalization scheme. However, since we will use the gluon DSE in the subtracted (and not again separated) form it is not necessary to rely on this multiplicative renormalization scheme. The corresponding subtractive renormalization scheme is discussed in the following.

2. In the quark equation the additional prescription

$$Z_{1F} \to \left(\frac{F(y)}{F(s)} \right)^\delta \tag{5.55}$$

(where y is the loop momentum) has been used in order to correctly reproduce the anomalous dimensions. For consistency this should be also used in the quark–loop. As compared to (5.45) and (5.46) this gives

$$\Pi_<(p) = \frac{1}{3p^2} G(p) \frac{8\pi}{(2\pi)^4} \int_0^{p^2} dk^2\, k^2 \sigma_v(k) I(p,k) \left(\frac{F(y)}{F(s)} \right)^\delta \tag{5.56}$$

$$\Pi_>(p) = \frac{1}{3p^2} \frac{8\pi}{(2\pi)^4} \int_{p^2}^{\Lambda^2} dk^2\, k^2 \sigma_v(k) I(p,k) G(k) \left(\frac{F(y)}{F(s)} \right)^\delta . \tag{5.57}$$

Comparing with (5.51) one finds that the scale dependence that is introduced by (5.55) in (5.51) cancels the remaining scale dependence of the quark–loop. Furthermore, the additional factor $F(y)^\delta$ implies that the quark–loop now contributes a logarithmic divergence of the form

$$\sim \log(L)^{1-2\delta} \tag{5.58}$$

which corresponds the correct anomalous dimension of the gluon. To shortly summarize: the prescription (5.55) leads to the correct cutoff and scale dependence of the quark–loop contribution to the gluon DSE. In the present renormalization scheme (i.e. if (5.43) together with (5.55) is used) the UV divergence of the quark–loop appears as an additive constant. Therefore all cutoff dependence is cancelled and the full gluon equation is renormalized if the gluon DSE is used in the subtracted form (5.21).

If one would use the gluon DSE in the subtracted and again separated form one would have to explicitely subtract the divergent constant according to

$$\Big(\Pi_<(p)+\Pi_>(p)\Big)-\Big(\Pi_<(\mu)+\Pi_>(\mu)\Big)= \\ \Big(\Pi_<(p)+\Pi_>(p)-\Pi_>(0)\Big)-\Big(\Pi_<(\mu)+\Pi_>(\mu)-\Pi_>(0)\Big)\,. \quad (5.59)$$

The quark–loop contribution to the gluon DSE would then be

$$-\frac{N_f}{2}\Big(\Pi_<(p)+\Pi_>(p)-\Pi_>(0)\Big) \quad (5.60)$$

where $\Pi_<$ and $\Pi_>$ are defined in (5.56) and (5.57) respectively. However, since any constant could have been introduced this is ambiguitive as has been repeatedly mentioned.

The subtractive renormalization scheme (2.) is used for all calculations where the gluon DSE has been used in the subtracted form (4.71). This applies to all results for the gluon-, ghost- and quark propagators.

Chapter 6

Results for Gluons, Ghosts and Quarks

This chapter focuses on the numerical results that are obtained as solutions to the full, coupled system of DSEs for the gluon-, ghost- and quark propagators. The solution that is presented here is an ab initio solution of the coupled system subject to the truncations that have been discussed. The main objective is therefore not to reproduce all experimentally known quantities to high accuracy but to learn about the more qualitative features of the solutions for the propagators; chiral symmetry breaking and positivity being the primary concerns.

First the accuracy of the present approach is discussed. The gluon DSE in its subtracted and separated form ((4.31) subject to (4.33)) and in the subtracted form (4.31) are compared and the influence of the infrared analysis and of the renormalization scheme on the results is investigated.

Following this the results for the quenched approximation (i.e. neglecting the effects of the quark field fluctuations) are discussed. Finally the results for the full, unquenched system of DSEs are presented. These results are then compared to recent lattice results and the (non-)positivity of the corresponding spectral densities is examined.

6.1 Accuracy of the Approach

This section centers on the inherent accuracy of the present approach as far as the results for the propagators and for quantities like the pion decay constant are concerned.

Depending on whether the gluon DSE is used in its subtracted form (4.31) or in its subtracted and again separated form ((4.31) subject to (4.33)) this accuracy is limited because of different technical reasons. Using the gluon DSE in the subtracted and again separated form ((4.31) subject to (4.33)) one has to fix the value of the parameter t which determines the infrared behaviour of gluon- and ghost renormalization functions. If the gluon DSE is used in the form (4.31) than the value of (4.75) has to be fixed.

The physical boundary condition that the system of DSEs has to satisfy as well as the analytically known infrared limit of the solutions will be utilized to constrain these formal

t	$R(L)$	$\sqrt{\sigma}$/MeV	$f_\pi/\sqrt{\sigma}$	f_π/MeV	$-\langle q\bar{q}\rangle^{1/3}$/MeV
-3	0.891	189.3	0.0800	15.2	63.9
-2	0.903	229.7	0.0875	20.1	80.5
-1	0.916	283.9	0.0956	27.1	102.9
0	0.930	359.5	0.1043	37.5	133.8
+1	0.946	469.7	0.1137	53.4	178.4
+2	0.964	639.5	0.1239	79.2	242.5
+3	0.985	920.1	0.1349	124.1	302.2

Table 6.1: Results for $N_f = 0$ using the subtracted and separated gluon DSE ((4.31) subject to (4.33)), for different values of the IR parameter t. The corresponding plots of F, R and of the effective coupling FR are shown in fig. 6.1.

parameters as much as possible.

The following discussion relies on the system of DSEs for gluons, ghosts and quarks in the quenched approximation. First the results for the gluon DSE in the form ((4.31) subject to (4.33)) are discussed and the corresponding results for the subtracted but not separated form (4.31) are presented in the second part of this section.

For the gluon DSE in the subtracted and separated form ((4.31) subject to (4.33)) it is necessary to use the subleading orders of the infrared expansion which has been discussed in section 4.4. This infrared analysis refers to the parameter t which is not fixed in any way. However, the value of t is quite important as far as the strength of chiral symmetry breaking in the fermion equation is concerned. In table 6.1 the results for $N_f = 0$ and for $-3 \leq t \leq +3$ are listed. On a technical level it is interesting to note that the value of R at the cutoff does depend on the value of t, as can be seen in the first column of table 6.1. This value of R at the cutoff is important because perturbation theory corresponds to the limit

$$R(x) \to 1 \qquad \text{and} \qquad F(x) \to \frac{1}{\log(x)} \tag{6.1}$$

for asymptotically large x. Therefore, in general R at the numerical UV cutoff L should be as close to 1 as possible. This is because the difference of $R(L) - 1$ measures the extent to which the perturbative regime of the solutions has been reached at the cutoff.

Table 6.1 also shows the results for the pion decay constant and the chiral condensate. These have been calculated using the Pagels-Stokar approximation [PS79] for the pion decay constant

$$f_\pi^2 = \frac{N_c}{4\pi^2} \int dq^2 q^2 M^2(q^2) \frac{1 + q^2 \left(M'(q^2)\right)^2}{\left(q^2 + M^2(q^2)\right)^2} \tag{6.2}$$

and the corresponding chiral limit approximation for the condensate:

$$\langle q\bar{q}\rangle = -\frac{N_c}{4\pi^2} \int dq^2 \frac{q^2}{A(q^2)} \frac{M(q^2)}{q^2 + M^2(q^2)} \tag{6.3}$$

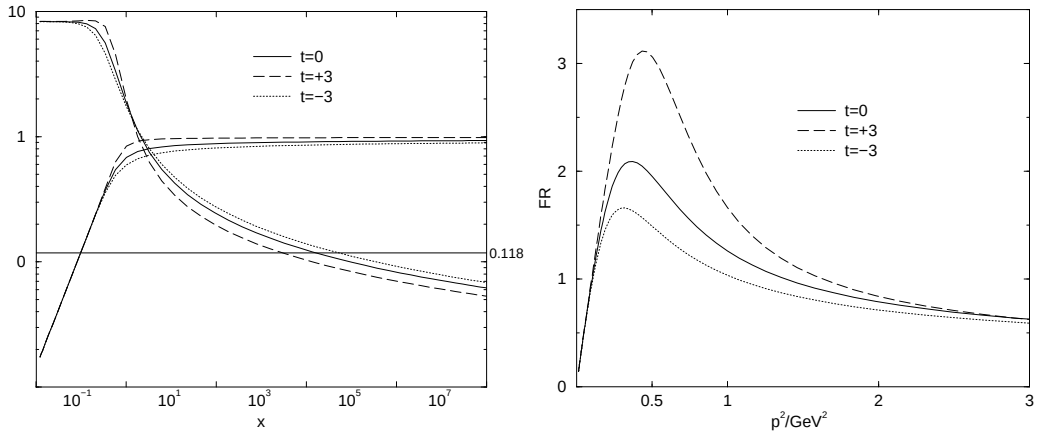

Figure 6.1: Results for the subtracted and separated system of equations for $N_f = 0$. *Left panel:* The functions F and R for $t = -3, 0, +3$. *Right panel:* The effective coupling $(F \cdot R)$ for $t = -3, 0, +3$. The corresponding results for the pion decay constant f_π and for the chiral condensate $\langle q\bar{q}\rangle$ are listed in table 6.1.

where the definition of the mass function $M(x) = B(x)/A(x)$ has been used and where M' denotes the derivative of M [1]. The chiral condensate $\langle q\bar{q}\rangle$ has a contribution from the bare propagator if the bare current quark mass m_0 is nonvanishing. This contribution has to be subtracted; however, this is a delicate issue since it is necessary to know the scaling behaviour of the mass function not only in the perturbative domain but also for intermediate and small momenta. It has been found that the result for the quark condensate does depend quite strongly on the assumed scaling behaviour of the bare mass. Therefore it seems to be more trustworthy to use the relation (6.3) only in the chiral limit $m_0 = 0$ where the bare contribution to $\langle q\bar{q}\rangle$ vanishes.

Note that the results for the pion decay constant and for the chiral condensate do depend on t quite drastically. However, if one compares the results for the pion decay constant before and after multiplication with the scale σ than one sees, that this strong dependence is mostly due to the pronounced t dependence of the IR scale σ. The reason can be seen by looking at the left panel of figure 6.1. The function F is essentially (up to a constant factor) the nonperturbative running coupling. And the scale σ is determined using the value of the running coupling at the mass of the Z boson:

$$\alpha_s\Big|_{M_Z} = \frac{1}{4\pi\beta_0} F\left(\frac{M_Z^2}{\sigma}\right) \stackrel{!}{=} 0.118\,. \tag{6.4}$$

The left panel of figure 6.1 clearly shows that the t-variation has a strong influence on the point where F crosses 0.118. (The constant factor that distinguished F and the strong coupling (6.4) doesn't change this qualitatively.) Figure 6.1 thus makes completely obvious why the scale σ has such a strong dependence on the parameter t. The figure also shows

[1] See [RW94] for a derivation and a discussion of the relations (6.2) and (6.3)

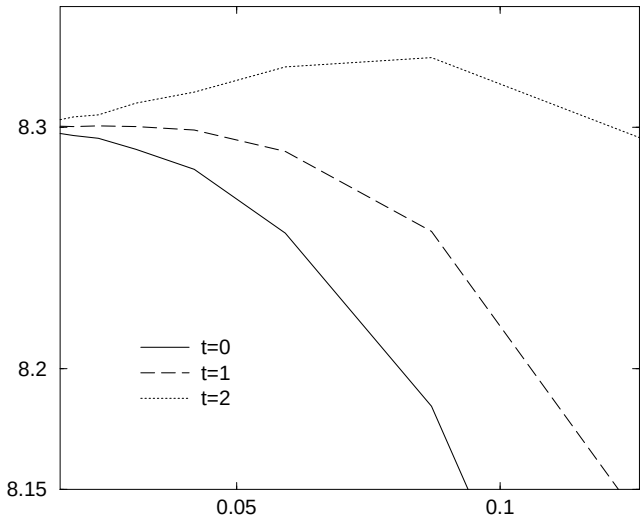

Figure 6.2: F for small momenta for different values of the IR parameter t.

t	$R(L)$	$R(L=10^8)-R(10^3)$
-3	0.891068	0.0526
0	0.930478	0.0341
+3	0.985035	0.0085
+3.2	0.989766	0.0064
+3.4	0.994708	0.0042
+3.6	0.999942	0.0019
+3.8	1.005290	-0.0005

Table 6.2: Variation of $R(x)$ for large momenta with respect to the parameter t.

that the large momentum region is not very well suited to this method to determine the value of σ, since a small change in F might lead to a quite substantial change of σ.

The change of the scale σ is the main reason for the t-dependence of the pion decay constant f_π and the chiral condensate $\langle q\bar{q}\rangle$. However, it is not only the scale that changes it is also the effective interaction $(F \cdot R)$ that enters the fermion DSE and which determines the strength of chiral symmetry breaking. The corresponding results for $(F \cdot R)$ and for $t = -3, 0, +3$ are shown in the right panel of figure 6.1. This shows that the effective interaction for $t = +3$ has a larger peak value and is also broader than the effective interaction for the case $t = 0, -3$.

To sum up: there are two reasons for the t-dependence of the order parameters f_π and $\langle q\bar{q}\rangle$; one reason is the change of the IR scale σ the other is the change of the effective interaction $(F \cdot R)$ which essentially determines the strength of the chiral symmetry breaking in the quark DSE. These two effects combine to yield the total t-dependence of f_π/MeV and of $-\langle q\bar{q}\rangle^{1/3}$/MeV in table 6.1.

The t-dependence, while seemingly small for the renormalization functions Z, G or F, R, leads to an amplified t-dependence of the results for the pion-decay constant and the chiral condensate (see table 6.1). Obviously one has to fix this dependence on t by an independent constraint. This constraint is dictated by the system of DSEs: it is given by the analytically known and physically motivated behaviour of the solutions for very small and very large momenta. In the infrared F must become constant and for very large momenta the functions F and R should approach their corresponding perturbative limits as closely as possible.

The infrared limit of F for 3 different values of t is shown in fig. 6.2. Given that F must become constant in the infrared (and assuming that the momenta that are shown are small enough) one has to conclude that values above $t = 2$ do not correspond to the analytically known IR behaviour of F (There is yet another reason: F is proportional to the nonperturbative running coupling and should therefore be a strictly decreasing function.). This effectively gives an upper bound to the range of allowed t-values. The second constraint refers to the perturbative limit, i.e. the behaviour of R and F for very large momenta. The degree to which the perturbative limit of R is reached at the cutoff is demonstrated in table 6.2. These results favour larger values of t. The two constraints together limit the range of allowed t-values to a very narrow interval which then determines the accuracy of the obtained solutions for the renormalization functions.

In the first part of the present section the t-dependence of the results of the gluon DSE in the subtracted and separated form ((4.31) subject to (4.33)) have been discussed. In the second part of this section the corresponding investigations for the gluon DSE in the form (4.31) are discussed. The results do not depend on t, however, they do depend on the value of

$$\frac{\beta_0}{F^{1-2\delta}R^2} \tag{6.5}$$

at the subtraction point. This is examined in the following

To test the numerical procedure and the accuracy of the routines one should examine first how precisely a specific value of (6.5) is reproduced by the final solution of the subtracted equation. The results that are listed in table 6.3 show: above $\beta_0/(R^2(1)F^{1-2\delta}(1)) = 8$ the renormalization condition is reproduced with very good accuracy. The right column gives the corresponding values of $R(L)$ which must depend on the renormalization condition that has been used for (6.5). Please note that the renormalization condition

$$ZG^2(\mu) = 1 \tag{6.6}$$

is not affected in any way by this choice of the value of (6.5). This is because the equations are solved for the functions F and R which parameterise the renormalization functions Z and G according to

$$Z(k^2) = \left(\frac{F(x)}{F(s)}\right)^{1-2\delta} R^2(x) \qquad G(k^2) = \left(\frac{F(x)}{F(s)}\right)^{\delta} \frac{1}{R(x)} \tag{6.7}$$

with $x = k^2/\sigma$ and $s = \mu^2/\sigma$. Using these representations of Z and G one finds

$$ZG^2(x) = \frac{F(x)}{F(s)} \tag{6.8}$$

$\beta_0/(R^2(s)F^{1-2\delta}(s))$	$\beta_0/(R^2(x)F^{1-2\delta}(x))\big\|_{x=s}$	$R(L)$
5	5.8570	1.0806
8	7.9999	1.0173
9	9.0000	1.0029
10	9.9999	0.9903
11	10.9998	0.9791
12	12.0002	0.9689
13	13.0000	0.9594
14	13.9999	0.9506
15	14.9999	0.9423
20	19.9997	0.9063
30	30.0003	0.8495

Table 6.3: The left column gives the value of (6.5) at the renormalization point $s = 1$. The middle and the right column list the results using these renormalization condition and renormalization point. The results have been obtained using only quite moderate numerical efforts and a very moderate convergence criterion.

thus that the renormalization condition (6.6) is satisfied for any pair of functions F, R. Especially the value of R at the cutoff is not fixed in any way by the renormalization condition (6.6). However, in order to reproduce perturbation theory one would like to find the limits

$$R \to 1 \qquad \text{and} \qquad F \to 1/\log(x)\ . \tag{6.9}$$

To conclude: If only the renormalization condition (6.6) is imposed, the system of equations for F, R is not sufficiently constrained, i.e. there is a one parameter family of solutions where the value of (4.75) is the parameter, see the discussion in section 4.4. This parameter effectively implements the second renormalization condition and is chosen to guaranty that F, R have the correct limits in the perturbative region.

Having thus verified that the solutions consistently reproduce the imposed renormalization condition we now proceed with further tests of the accuracy. A mandatory physical condition is that the results must not depend on the renormalization point s. Let us assume that one does impose the condition

$$\frac{\beta_0}{R^2(s)F^{1-2\delta}(s)} = 12 \tag{6.10}$$

at $s = 1$. This corresponds to the values which are shown in table 6.4. One can now use each pair of values which is listed in table 6.4 as renormalization condition. Each of these pairs should be equally suited to reproduce the whole table. However, due to numerical instabilities it is not the whole range of momenta (from 0 to the UV cutoff) where the results are independent of the subtraction point s. The calculations show that the results for F and R are each independent of the renormalization point s with a relative accuracy of less than 10^{-4} if $1 \leq s \leq 5 \cdot 10^3$. Outside this interval the accuracy of the renormalization point independence decreases.

x	$\frac{\beta_0}{R^2(x)F^{1-2\delta}(x)}$
0.1583E-1	6377.3642
1.0	12.0002
0.11753E+2	23.0962
0.18370E+3	33.0757
0.15697E+4	39.4292
0.13243E+5	45.0527

Table 6.4: The momentum $x = p^2/\sigma$ and the value of $\beta_0/(R^2(x)F^{1-2\delta}(x))$ if the renormalization condition (6.10) is used.

*	$R(L)$	$\sqrt{\sigma}$/MeV	$f_\pi/\sqrt{\sigma}$	f_π/MeV	$-\langle q\bar{q}\rangle^{1/3}$/MeV
22.0	0.914	274.1	0.0942	25.8	98.9
21.0	0.923	319.3	0.0999	31.9	117.4
20.0	0.933	378.1	0.1061	40.1	141.4
19.0	0.945	456.6	0.1127	51.5	173.0
18.0	0.957	566.6	0.1199	68.0	215.8
17.0	0.972	732.3	0.1282	93.8	272.9

Table 6.5: Results for the subtracted but not separated equation, for $N_f = 0$. The leftmost column gives the value of $\beta_0/(F^{1-2\delta}R^2)$ at the subtraction point. The results for the pion decay constant f_π and for the chiral condensate $\langle q\bar{q}\rangle$ have been calculated using (6.2) and (6.3) respectively.

Having verified the numerical accuracy and stability of the subtraction procedure one can now investigate the dependence of the strength of chiral symmetry breaking on the constraint (6.5).

The results in table 6.5 show a similar dependence on the value of (6.5) as the results in table 6.1 show on the value of the parameter t. The IR scale σ does again depend quite strongly on the value of (6.5) at the subtraction point and it varies in accord with the value of R at the cutoff. This change of the scale σ together with the change in the effective interaction again combines to yield the total change of the pion decay constant f_π and the chiral condensate $\langle q\bar{q}\rangle$, see table 6.5.

The value of R at the cutoff increases as the value of (6.5) is decreased. And since the same arguments as for the gluon DSE in the subtracted and separated form apply one has to conclude that the perturbative limit of R (and of F) favours small values of (6.5).

But as for the gluon equation in the subtracted and separated form it is not only the variation of R at the cutoff that has to be taken into account; it is also the behaviour of F in the infrared that has to be compared. In our approach F is (up to constant factors) just the nonperturbative running coupling, compare (6.4) and the running coupling should be a strictly decreasing function of the renormalization point. Figure 6.3 shows that F has a bump in the infrared if $\beta_0/(F^{1-2\delta}R^2)$ is chosen to be below a certain critical value, which

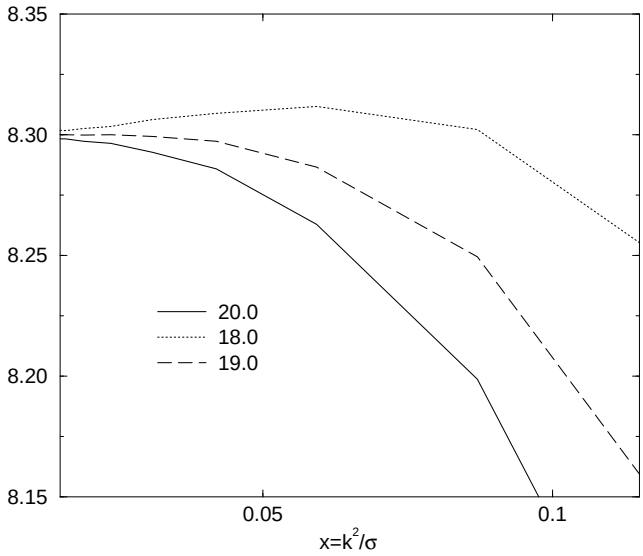

Figure 6.3: Behaviour of $F(x)$ for $x \to 0$ and for different values of $\beta_0/(F^{1-2\delta}R^2)$ at the subtraction point, using the gluon DSE in its subtracted form (6.5).

in turn does of course depend on the subtraction point. I.e. for the subtraction point $x = \mu^2/\sigma = 3.286$ that has been used to calculate the results in table 6.5 and in figure 6.3 the renormalization condition has to satisfy

$$\frac{\beta_0}{F^{1-2\delta}R^2} > 18 \tag{6.11}$$

This gives a lower bound on the range of allowed values for (6.5). Comparing this to the results in table 6.5 one has to conclude that the pion decay constant is not larger than ≈ 68MeV.

To summarize: In principle one would like to have that R at the cut-off is as close to 1 as possible, because then the solutions extend far into the perturbative region. However, the coupled system of DSEs and especially the identification of the nonperturbative running coupling enforce another constraint: the coupling should be a strictly decreasing function, because otherwise the corresponding β function would be double-valued. This constraint effectively limits the range of allowed values for (6.5) as it limits the range of allowed values for the IR parameter t. The two constraints together, i.e. the known behaviour of the solutions in the infrared and in the ultraviolet effectively constrain the range of allowed values for (6.5) to a narrow interval. The width of this interval then determines the overall accuracy of all the results. This is because the infrared scale σ is determined by matching the value of the nonperturbative running coupling to the known value of α_s at the mass of the Z-boson. Any inaccuracy in F will thus lead to a much amplified inaccuracy in the scale σ which is then inherited by all further results.

It remains to compare the two approaches with regard to the mutual consistency of the

results. As a first step one solves the system of DSEs for the gluon and the ghost using the gluon DSE in its subtracted and separated form ((4.31) subject to (4.33)). This gives the functions F and R for all momenta. In a second step one can now take these results for F and R (that have been obtained using the gluon DSE in the *subtracted and separated* form) and calculate the value of

$$\frac{\beta_0}{F^{1-2\delta}R^2} \tag{6.12}$$

at some arbitrary subtraction point s. This can then be used as input for the second approach where the gluon equation in the subtracted (and *not separated*) form (4.31) is used. The results that are obtained in this way using the two approaches do agree to very high accuracy (relative difference $< 10^{-4}$ whereby the numerical effort has still been quite modest). Note that this does *not* imply that the constant in the gluon DSE is zero; the two equations can be compared only for the case that the constant *is* zero, however, it might be nonzero in general.

In the following we will use the gluon DSE in the subtracted but not separated form (4.31) exclusively.

6.2 Quenched Approximation

The coupled system of gluon- and ghost DSEs in the quenched approximation has been extensively studied first by v. Smekal, Hauck and Alkofer [vSHA97, vSHA98, vS98, AvS00] and using bare vertices by Atkinson and Bloch [AB98b, AB98a]. This can be extended by adding the quark DSE to the gluon-ghost system while still neglecting the quark loop. In this quenched approximation the quarks do not couple back to the gluons and ghosts, however, the results for the gluons and ghosts determine the results for the quarks. The results for this quenched approximation are presented in this section.

The results for the gluon- and ghost renormalization functions are shown in the left panel of fig. 6.4 using the parameterization (4.50) which defines the functions F and R. As implied by the analytic infrared analysis the numerical solution for F shows that it becomes constant in the infrared and that R behaves like $R \sim x^\kappa$ for small x. Using the relations (4.50) this implies that the gluon renormalization function Z is infrared vanishing whereas the ghost renormalization function G is infrared diverging. This is in complete accordance with the analytically obtained infrared behaviour which is

$$Z \sim x^{2\kappa} \quad \text{and} \quad G \sim x^{-\kappa} \tag{6.13}$$

for $x \to 0$ and with $\kappa \approx 0.92$ (see section 4.4). The infrared behaviour of F does especially reflect the analytically obtained result that the nonperturbative running coupling (4.52) has an infrared fixed point at about 9.48.

The corresponding results for the vectorial self-energy A and the mass function $M = B/A$ are shown in the right panel of fig. 6.4. The mass function M is strongly enhanced and thus clearly shows that the solution corresponds to broken chiral symmetry. This is also expressed by the low energy constants like the pion decay constant f_π and the chiral condensate $\langle q\bar{q}\rangle$.

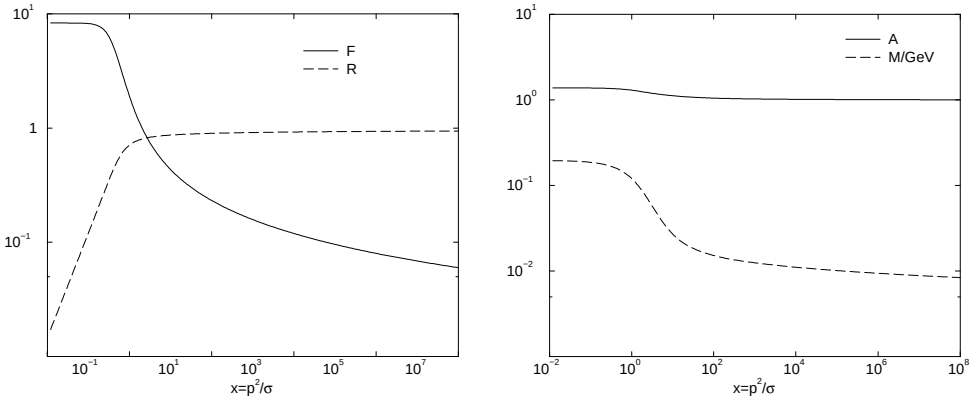

Figure 6.4: Results for the quenched approximation for one light quark ($m_0 = 1$ MeV); *Left panel:* Results for the functions F and R that are related to the gluon- and ghost renormalization functions Z and G via (4.50). *Right panel:* Results for the vectorial self-energy A and the mass function $M = B/A$ where A and B are related to the full quark propagator via (5.2).

The numerical solutions that have been found for the quenched approximation yield (using (6.2) and (6.3)):

$$f_\pi \approx 51 MeV \quad \text{and} \quad -\langle q\bar{q}\rangle \approx \left(168 MeV\right)^3 \tag{6.14}$$

where the quark condensate $\langle q\bar{q}\rangle$ has been calculated in the chiral limit such that there is no bare contribution which would have to be subtracted otherwise. The numerical values given here do of course depend on the scale σ that is determined by matching the nonperturbative running coupling (4.52) at the mass of the Z-boson to the experimentally known value:

$$\alpha_s\Big|_{M_Z} = \frac{1}{4\pi\beta_0} F\left(\frac{M_Z^2}{\sigma}\right) \stackrel{!}{=} 0.118 \tag{6.15}$$

The problems that arise due to this matching procedure have been discussed in the previous section. These technical problems imply that even small inaccuracies (be they numerical or due to the finite accuracy subtraction) will inevitably change the scale by an amount which is large enough to change e.g. f_π by about 5%.

The left panel of fig. 6.4 also shows the vectorial self energy A. The results show that A is slightly enhanced for small momenta and that it becomes constant in the infrared at about ≈ 1.35. Aside from this infrared limit A does not display any other qualitative feature.

6.3 Dynamical Quarks

Some of the qualitative features of the inclusion of the quark loop have already been discussed in the preceding sections. There it has been shown that the quark loop contribution

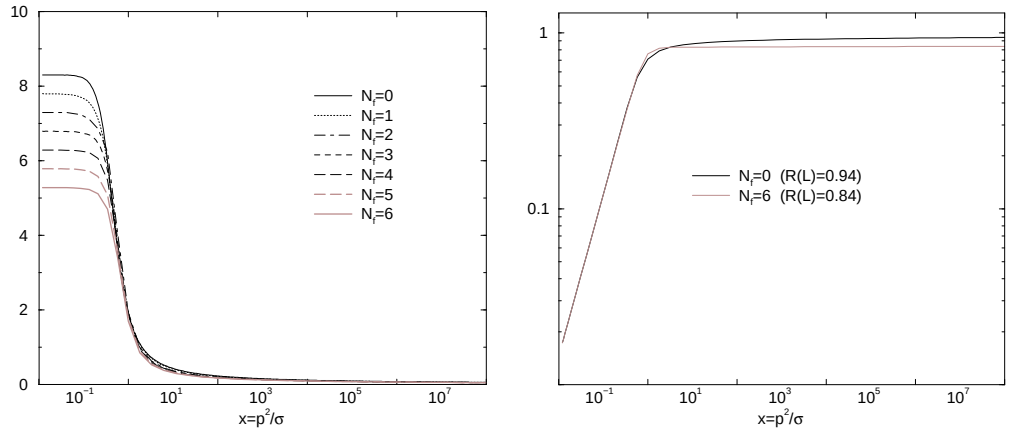

Figure 6.5: Numerical results for F, R for different numbers of flavours, for the full, unquenched calculation. *Left Panel:* Results for F for $N_f = 0, 1, 2, 3, 4, 5, 6$. (See also table 6.6 for the IR limits of F) *Right Panel:* Results for R for $N_f = 0, 6$; the results for $N_f = 1, 2, 3, 4, 5$ evolve continuously from the ($N_f = 0$)-result to the ($N_f = 6$)-result. (See also table 6.7 for the value of R at the cutoff) The functions F and R are related to the gluon- and ghost renormalization functions Z and G via (4.50) and the results for Z and G are shown in fig. 6.6.

N_f	0	1	2	3	4	5	6
$\lim_{x\to 0} F(x)$	8.2988	7.7958	7.2929	6.7899	6.2869	5.7839	5.2810

Table 6.6: Analytically derived values for the infrared limit a of $F \to a$ for $x \to 0$. These values are reflected in the numerical solution which is shown in the left panel of fig. 6.5.

to the gluon DSE is subleading in the infrared as compared to the ghost loop. This has been shown to imply that the leading infrared behaviour of the gluon- and ghost renormalization functions remains unchanged as compared to the quenched approximation. This is reflected by the solutions for F, R and for the case that $N_f > 0$ which are shown in fig. 6.5 The left panel of fig. 6.5 shows the numerical results for F for different numbers of flavours. For these calculations a corresponding number of light flavours has been chosen; i.e. $N_f = 3$ corresponds to three light flavours each having a bare quark mass of 1 MeV. The results show that the inclusion of the quark loop does not change the results for F on a qualitative level. It is only the infrared limit $F \to a$ for $x \to 0$ that depends on the number of flavours: a being smaller for larger N_f. This N_f-dependence is evident in the numerical solution that is shown in the left panel of fig. 6.5 as well as in table 6.6 which gives the analytically derived values for a as they have been obtained from the analytic infrared analysis in section 4.4.

The right panel of fig. 6.5 shows the solutions for R that correspond to the solutions for F which are shown in the left panel of the same figure for the two exemplary cases $N_f = 0$

N_f	0	1	2	3	4	5	6
$R(\Lambda^2/\sigma)$	0.944	0.941	0.934	0.923	0.904	0.869	0.841

Table 6.7: Numerical results for the value of R at the cutoff for different N_f. The solutions for $R(x)$ for $N_f = 0$ and $N_f = 6$ are shown in the right panel of fig. 6.5.

N_f	0	1	2	3	4	5	6
σ	440	397	349	307	228	144	83

Table 6.8: Results for the infrared scale σ for $N_f = 0, 1, 2, 3, 4, 5, 6$.

and $N_f = 6$. The solutions for $N_f = 1, 2, 3, 4, 5, 6$ evolve smoothly from the $N_f = 0$ result to the result for $N_f = 6$ and the corresponding values of R at the cutoff are listed in table 6.7 for all N_f. The solutions are qualitatively very similar, however, the behaviour of R for large momenta does depend on the number of flavours N_f; more precisely: R is generally somewhat smaller for large momenta if the number of flavours is increased (see table 6.7). This does not conflict with the perturbative limit which implies that F and R behave like

$$F(x) \to \frac{1}{\log(x)} \qquad \text{and} \qquad R(x) \to 1 \tag{6.16}$$

The different values of R at the cutoff correspond to different values of the scale σ; these are listed in table 6.8. These results show that a smaller value of the IR scale σ corresponds to a smaller value of R at the cutoff. This correlation has to be expected since if calculated back to physical units $p^2 = x\sigma$ one has effectively a smaller cutoff (in physical units). Since R is a monotonically increasing function this scale dependence then implies that a smaller scale σ will correspond to a smaller value $R(L)$. However, the results show that this is not the only influence; the difference between the numerical results for R are not exhausted in the different values of R at the cutoff. The slope of the two solutions that are shown in the right panel of fig. 6.5 is different. Looking closer at the results one finds that the slope of R for large momenta is the smaller the larger the number of flavours is. There are thus two effects: first there is a scale dependence which effectively gives smaller values of R for large momenta and secondly the slope of R for large momenta becomes smaller if the number of flavours is increased.

However, a word of caution is in order here; in section 6.1 it has been discussed that the determination of the scale σ has an inherent inaccuracy. This accuracy of σ gives the upper bound for the accuracy of all further results and it effectively amounts to an overall accuracy of $\pm 5\%$ for the results that are listed in table 6.8.

The results for F and R directly translate into results for the renormalization functions for gluons and ghosts, Z and G and into corresponding results for the nonperturbative running coupling α_s as defined in (4.52). The results for the renormalization functions are shown in fig. 6.6 and they are related to the results for F and R via the definitions (4.50). These results show that Z and G do not change qualitatively due to the inclusion of the quark loop. The gluon renormalization function Z is infrared vanishing for all N_f whereas the

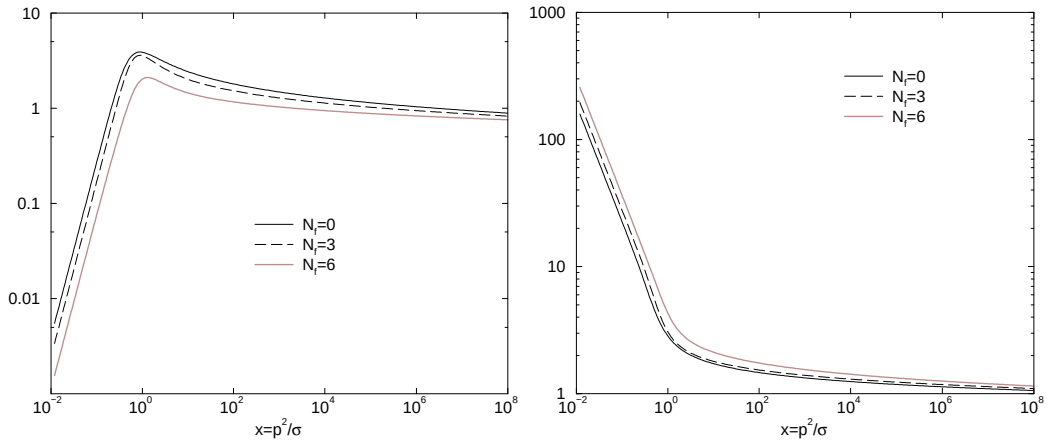

Figure 6.6: Numerical results for the gluon and ghost renormalization functions Z and G for $N_f = 0, 3, 6$. The results for $N_f = 1, 2, 4, 5$ evolve smoothly between the results that are shown. The corresponding results for F and R (which are related to Z and G via (4.50)) are shown in fig. 6.5.

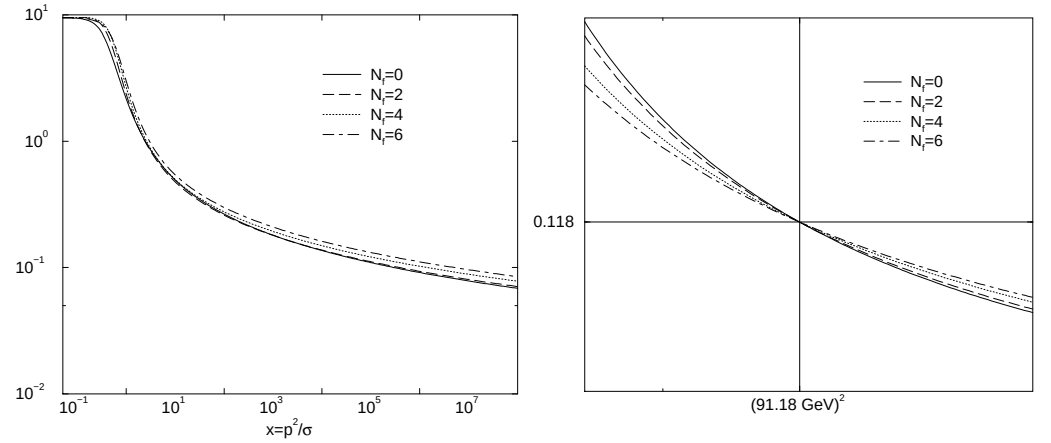

Figure 6.7: Numerical results for the non–perturbative running coupling α_s (defined in (4.52)) for $N_f = 0, 2, 4, 6$. *Left panel:* Results for α_s plotted over the momentum p^2 in units of σ. *Right panel:* Results for α_s in the vicinity of the renormalization point $\mu^2 = M_Z^2 = (91.187\mathrm{GeV})^2$ plotted over the momentum p^2 in units of GeV.

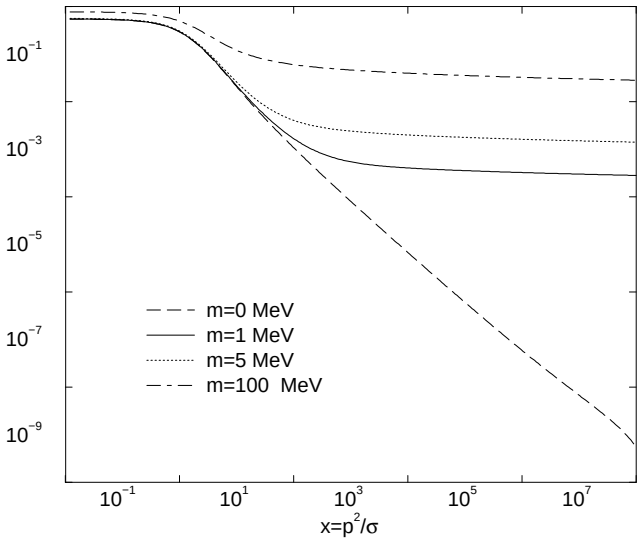

m_0/MeV	$M(0)$/MeV
0	191
1	193
5	198
10	209
100	332

Figure 6.8: Numerical results for the mass function $M(x) = B(x)/A(x)$, for the full, unquenched system using $N_f = 1$ and for different current quark masses m_0. *Left Panel:* Plots of $M(x)$ for $m_0 = 0, 1, 5, 100 MeV$. *Right Panel:* Values of $M(0)$ for $m_0 = 0, 1, 5, 10, 100 MeV$.

ghost renormalization function G is infrared diverging for all N_f thus leading to an infrared enhanced ghost propagator.

The results for α_s for different numbers of flavours are shown in fig. 6.7. The plots show that the (N_f)-dependence of the infrared limit of F is exactly cancelled by the $1/\beta_0$ factor that is the contained in the definition (4.52). This leads to an infrared fixed point of the running coupling α_s which is independent of the number of flavours N_f. For large momenta the running coupling decreases more slowly for larger numbers of flavours. This behaviour is shown in more detail in the right panel of fig. 6.7 which shows the results for α_s in the vicinity of the renormalization point $\mu^2 = M_Z^2$ and in physical units.

The results for the quark propagator are encoded in the vectorial self-energy A and the mass function $M = B/A$ where A and B are defined according to (5.2).

The mass function $M(x) = B(x)/A(x)$ is shown in the left panel of fig. 6.8 for $N_f = 1$ and different values of the current quark mass. It is evident that the mass function is strongly enhanced in the infrared which implies that the chiral symmetry is broken. Aside from this enhancement in the infrared the mass function does not show any unexpected qualitative features or any deviation from its strictly decreasing behaviour. However, the chiral limit solution (m_0=0) is clearly distinguished from the $m_0 > 0$ solutions by its different UV

N_f	0	1	2	3	4	5	6
f_π/MeV	51	47	43	40	35	29	23
$-\langle q\bar{q}\rangle^{1/3}/MeV$	168	157	145	134	122	110	96

Table 6.9: Results for the pion decay constant f_π and for the chiral condensate $\langle q\bar{q}\rangle$ for $N_f = 0,1,2,3,4,5,6$. The results for f_π have been calculated using $m_0 = 1MeV$ for all flavours which implies that for $N_f \geq 3$ the screening effect of the quarks is overestimated. The pion decay constant has been calculated using the Pagels-Stokar approximation (6.2). and the results for $\langle q\bar{q}\rangle$ have been calculated in the chiral limit $m_0 = 0$ using the relation (6.3).

scaling. From the renormalization group equation this is expected to be

$$M(x) \to -\frac{4\pi^2 d_M}{3} \frac{\big(\log(s)\big)^{d_M}}{\big(\log(x)\big)^{1-d_M}} \frac{\langle q\bar{q}\rangle_{\mu^2}}{x} \quad \text{for} \quad m_0 = 0\,, \tag{6.17}$$

$$M(x) \to \left(\frac{\log(s)}{\log(x)}\right)^{d_M} m_0 \qquad \text{for} \quad m_0 > 0 \tag{6.18}$$

for $x \to \infty$ where $x = p^2/\sigma$, $s = \mu^2/\sigma$ and $d_M = 12/(33 - 2N_f)$, the main difference being the additional $1/x$ for the case that $m_0 = 0$. This asymptotic behaviour is found in complete agreement with the numerical results that are shown in the left panel of fig. 6.8. The infrared limit of the mass function $M(x) = B(x)/A(x)$ is shown in the right panel of fig. 6.8. Also these results clearly demonstrate that the solution of the full coupled system does correspond to broken chiral symmetry. However, the results for M also show that chiral symmetry breaking is to weak; the values of $M(0)$ being only about $60\% - 70\%$ of the phenomenologically expected values.

The mass function does not show any qualitative (N_f)-dependence; the only difference being that the overall size of B and thus of the mass function M decreases as the number of flavours increases. This screening effect is clearly shown in table 6.9 where the results for the pion decay constant f_π and for the chiral condensate $\langle q\bar{q}\rangle$ are listed for different numbers of flavours. These results can be directly compared to the values that are used in recent phenomenological studies: $f_\pi \approx 92.6MeV$ (see [C$^+$98]) and $\langle q\bar{q}\rangle \approx (236MeV)^3$ (see [AJ88], [AJ90] and [RM90]). For $N_f = 0$ the numerical result is about 60% of the experimentally known value and for $N_f = 6$ the pion decay constant has about half the value that it has for $N_f = 0$. This is in complete accord with the (N_f)-dependence of the mass function and of the chiral condensate which all scale with N_f like the pion decay constant. The reason for this common (N_f)-dependence of all these quantities that measure the strength of chiral symmetry breaking essentially is that they all inherit the (N_f)-dependence of the infrared scale σ.

In table 6.10 the dependence of the results for the pion decay constant f_π (using the Pagels-Stokar approximation (6.2)) on the current quark mass m_0 is given for $N_f = 1$. These results allow to estimate the mass dependence of the results for f_π in table 6.9 where the N_f dependence of the results is the main issue.

m_0/MeV	0	1	2	5
f_π/MeV	46	47	50	66

Table 6.10: Results for the pion decay constant f_π for different current quark masses and for $N_f = 1$. The pion decay constant has been calculated using the Pagels-Stokar approximation (6.2).

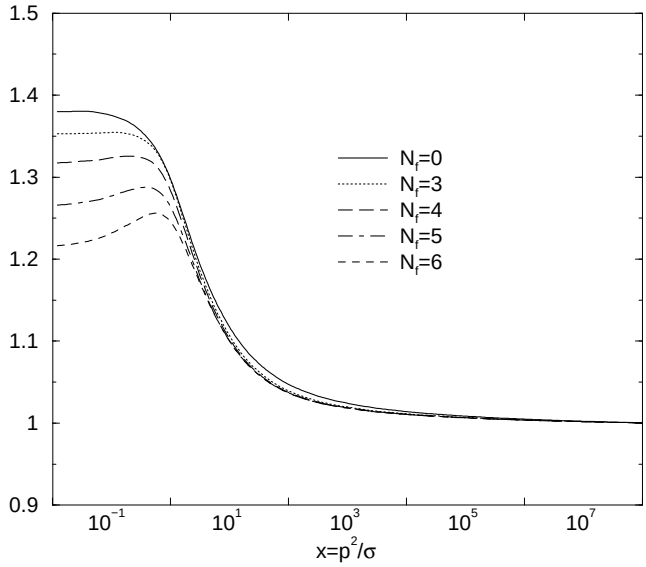

Figure 6.9: Results for the vectorial self-energy A of the quark which is related to the full quark propagator via (5.2). The corresponding results for other N_f interpolate smoothly between the results that are shown in the figure.

Again, a word of caution is in order here. As has been noted before: the results for the pion decay constant f_π and for the chiral condensate $\langle q\bar{q}\rangle$ can only be as accurate as the results for the infrared scale σ. This has been discussed repeatedly in the preceeding sections and it also applies to the results shown in table 6.9. The upshot is that the results in table 6.9 are to be considered accurate up to $\pm 5\%$

The results for the vectorial self-energy A are shown in fig. 6.9. Here it is more interesting to look at the (N_f)-dependence since A is essentially independent of the quark mass. The numerical results for $N_f = 0, 3, 6$ are shown in fig. 6.9 and the corresponding results for $N_f = 1, 2, 4, 5$ interpolate smoothly between the curves that are shown in fig. 6.9. There is no dramatic difference between the results for the quenched approximation and the the results for $N_f \geq 1, 2$. However, as can be seen in fig. 6.9 the infrared limit of A displays a non-negligible dependence on N_f which becomes more pronounced as the number of flavours is increased. Whereas the qualitative features remain unchanged the value of $A(0)$ as well as the size of the bump significantly depends on N_f; the bump at intermediate

momenta is more pronounced for large N_f. This bump therefore is an interference effect which is largely amplified in the full, unquenched case.

In this section the results for the full, unquenched system of DSEs for the gluon-, ghost- and quark propagators have been presented and discussed. The results have been presented for $0 \leq N_f \leq 6$ and for various values of the bare quark masses. The results for the quark propagators have been used to calculate the pion decay constant and the chiral condensate which have been compared to the phenomenologically accepted values.

The results for the gluon- and ghost renormalization functions are qualitatively very similar to the results that have been obtained in the quenched approximation, the main difference being the infrared limit of F. The results for the quark self-energies B and A do depend on the number of flavours N_f. The strength of chiral symmetry breaking becomes smaller as N_f is increased; this is, e.g., expressed by the decrease of the pion decay constant. The effective interaction in the quark subsystem which is the reason for chiral symmetry breaking is essentially $F(x)R(x)$. For very small x this effective coupling is very close to zero since $R \sim x^\kappa$ for small x. The effective coupling $F(x)R(x)$ therefore is essentially independent of the IR limit of F (which is multiplied by x^κ). This is accompanied by the observation that it is mainly the behaviour of R at intermediate and large momenta which determines the overall strength of the effective coupling.

Whereas the scalar self-energy B remains qualitatively unchanged as the number of flavours is altered, the vectorial self-energy A depends more fundamentally on N_f. As the number of flavours is increased the bump at intermediate energies becomes significantly enlarged. This bump therefore is an interference effect which is due to the inclusion of the quark loop in the gluon equation.

6.4 Comparison to Lattice Results

In the last section the numerical results for the full unquenched system of DSEs have been presented. In the present section these results will be compared to recent lattice results[2].

In fig. 6.10 the DSE–results for the gluon- and ghost renormalization functions Z and G are compared to corresponding lattice results. The left panel of fig. 6.10 shows a comparison of the numerical results for $N_f = 0$ for $Z(x)$ to the lattice results that have been reported in [LSW98]. The overall agreement between the DSE results for Z and the corresponding lattice results of [LSW98] is satisfactory. The only quantitative difference being the size and the shape of the bump in Z for small momenta. The lattice results and thus the comparison are valid for $N_f = 0$ only. However, since the results for the gluon renormalization function Z do depend only weakly on the number of flavours the agreement between the lattice results and the DSE results for $N_f > 0$ would be similar (compare right panel of fig. 6.10).

The agreement between the results for the ghost renormalization function G and the corresponding lattice results (right panel of fig. 6.10) is even more striking; the results are in very good agreement. As far as the (N_f)-dependence is concerned the same remarks as

[2] Also the results that have been reported in [Lan01] qualitatively support the behaviour of Z and G shown in fig. 6.10.

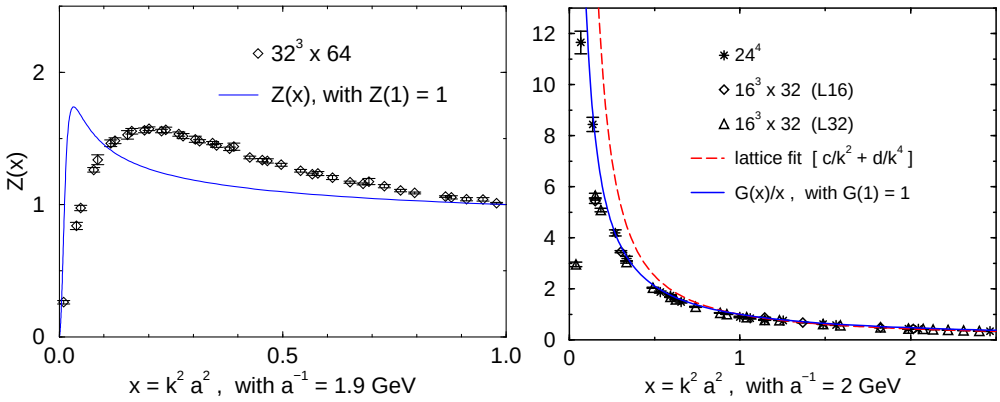

Figure 6.10: Comparison of the DSE-results for the renormalization functions Z and G with corresponding results from lattice calculations. *Left Panel:* Results for Z, the lattice results have been taken from [LSW98]. *Right Panel:* Results for G, the lattice results have been taken from [SS96].

for Z apply: the dependence on the number of flavours would be to small as to alter these conclusions (see right panel of fig. 6.6). However, the comparison is only valid for $N_f = 0$.

The numerical results for the quark propagator $Z = 1/A$ are compared in fig. 6.11 to recent lattice results for the quark propagator in Landau gauge [SW01]. These have been calculated using an improved Sheikholeslami-Wohlert quark action with tree-level mean-field improved coefficients. For the present purpose the most interesting set of results in the right panel is the renormalized quark propagator S_R which is marked by crosses $\times$. The results look qualitatively quite similar except the fact the the infrared behaviour of the lattice results seems to be slightly different than the IR behaviour of the Dyson-Schwinger results. The DSEs give a $Z = 1/A$ that becomes constant in the deep infrared whereas the lattice results seem to indicate that Z is a monotonically decreasing function in the infrared. The lattice results have to be compared to the case $N_f = 0$ which (as far as the results for A and thus for $Z = 1/A$ are concerned) is barely different from the results for $N_f = 1, 2$. This implies that both methods agree on the qualitative result that Z for $N_f = 0$ is a monotonically increasing function.

6.5 Positivity

In the first section the basic symmetries of QCD and especially the BRS symmetry of the QCD Lagrangian have been outlined. There it has been elucidated that positivity is a key issue in the BRS quartet mechanism. In order to identify the physical subspace of the total state space it is therefore necessary to check whether the propagators that have been calculated in solving the full coupled system of DSEs do violate the positivity constraints. This would then give rise to the compelling picture that confinement is evident in the propagators via violations of the positivity constraints which would apply to particles that appear in the

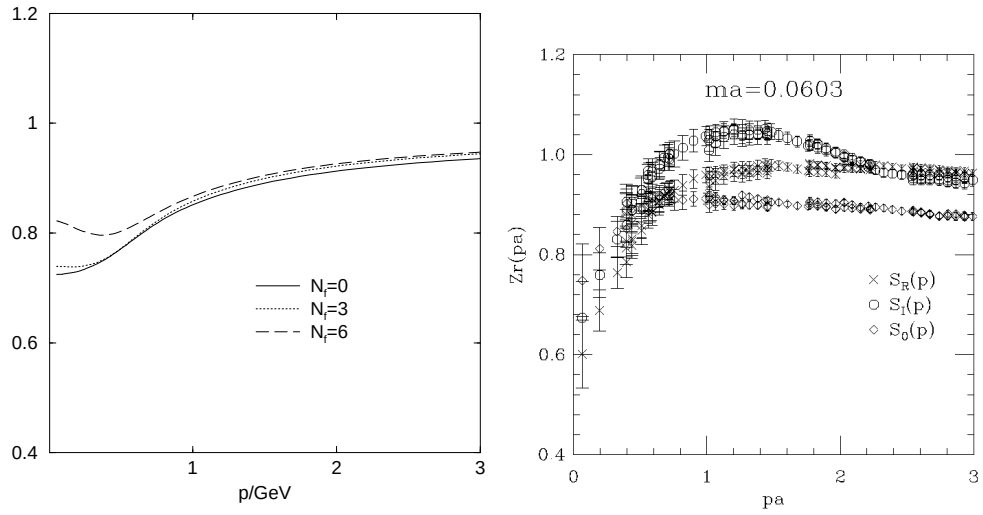

Figure 6.11: Comparison of the DSE–results for $Z = 1/A$ (*Left Panel*) and the corresponding lattice results (*Right Panel*) which have been taken from [SW01].

asymptotic spectrum of the theory.

The Dyson-Schwinger formalism is set up in Euclidean space. This implies that the thus obtained Greens functions have to to satisfy the Osterwalder-Schrader axioms ([OS73], [OS75]) which are the basic axioms for a Euclidean quantum field theory. In section 3.5 a short outline of the approach and the formalism has been given; there we especially emphasised the fact that the Euclidean pendant of the positivity constraint is Osterwalder-Schrader reflection positivity.

For the most basic case, for the propagator, reflection positivity can be written as:

$$\int d^4x d^4y \bar{f}(-x_0, \vec{x}) D(x-y) f(y_0, \vec{y}) \geq 0 \tag{6.19}$$

where f is a complex valued test function with support in $\{(x_0, \vec{x}) | x_0 > 0\}$. This special case of Osterwalder-Schrader reflection positivity can be shown to be a necessary as well as sufficient condition for the existence of a Källen-Lehmann representation [AvS00]. Therefore it is sufficient to find a counter example by suitably choosing the test function f which is completely unconstrained.

After a three dimensional Fourier transformation the condition (6.19) becomes

$$\int_0^\infty dr ds \bar{f}(r) \tilde{D}(-(r+s), \vec{p}) f(t) \geq 0 \tag{6.20}$$

where

$$\tilde{D}(x_0, \vec{p}) = \int d^3x D(x_0, \vec{x}) exp(i\vec{p}\vec{x}) \geq 0 \tag{6.21}$$

and f denotes from here on the Fourier transform of the test function f in (6.19).

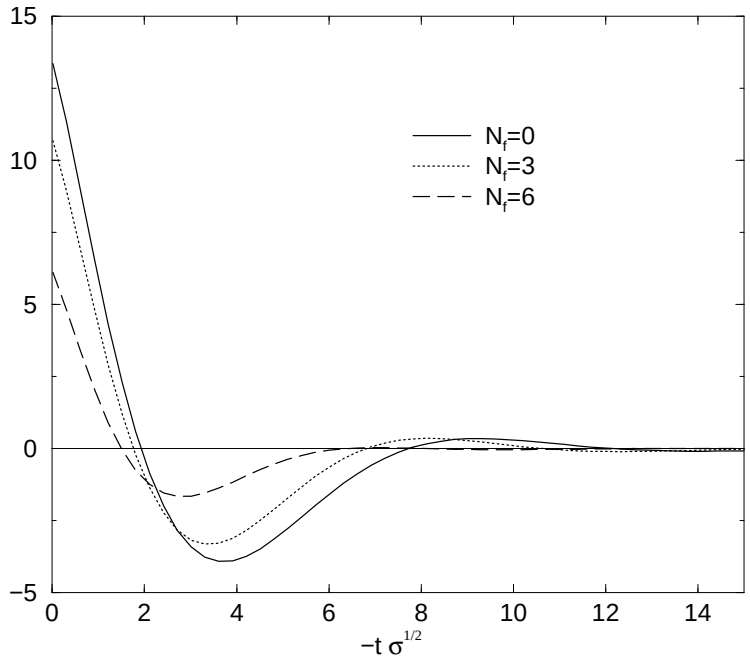

Figure 6.12: Results for the Fourier Transform (6.22) for $N_f = 0, 3, 6$. For other N_f the results interpolate smoothly between the values that are shown in the figure. The absolute value $\vec{p}^2$ has been set to 0.

Obviously it suffices to look at the Fourier transform (6.21). If this Fourier transform of the propagator is found to be negative within an interval then one can always choose the test function f in a way that only this specific interval contributes to the integral in (6.19) thus resulting in a violation of the condition (6.19).

First we will look at the positivity condition (6.21) for the gluon propagator. Two of the integrations can be trivially performed leaving the one dimensional integral

$$\tilde{D}(t, \vec{p}^2) = \int dp_0 \frac{Z(p_0^2 + \vec{p}^2)}{p_0^2 + \vec{p}^2} exp(ip_0 t) \geq 0 \tag{6.22}$$

Please note that $\vec{p}^2$ has the status of a parameter in this case: in order to conclude that positivity is violated it suffices to show that $D(t, \vec{p}^2)$ is negative for a finite interval of $\vec{p}^2$-values.

The result is shown in fig. 6.12 It is clearly visible that the Fourier transform (6.22) is negative within an interval $2 \leq t \leq 6$ (This feature has been explicitely verified to persist for $0 \leq \vec{p}^2 \leq 10$). This unambiguously demonstrates that the gluon propagator does violate reflection positivity. This implies that the gluon propagator of the corresponding Garding–Wightmann field theory does not have a Källen-Lehmann representation with positive definite spectral density, i.e. the gluon propagator that has been found corresponds to gluonic excitations which cannot be found in the asymptotic spectrum. This result had

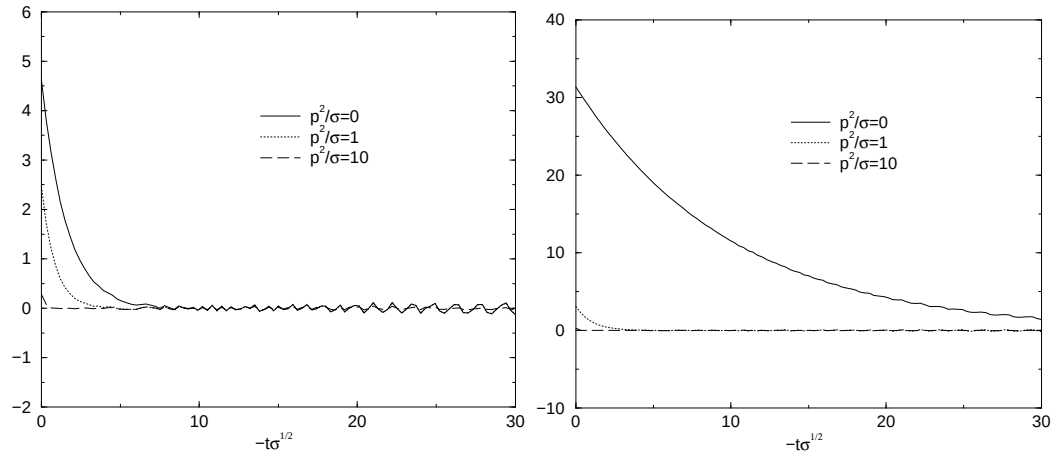

Figure 6.13: *Left Panel:* Results for the Fourier transform (6.23), testing positivity for the full quark propagator. *Right Panel:* Fourier transform (6.23) for the bare propagator, i.e. for $A = 1$ and $B = m_0$. The results in the left panel show an oscillatory behaviour for large values of $-t\sigma^{1/2}$ which is, however, simply due to the limited numerical accuracy. This cannot be interpreted as violation of positivity.

already been found for the quenched approximation, neglecting the influence of the quark loop. These results show that the quark loop somewhat alters the extent to which (6.22) is negative; however, the qualitative feature that the Fourier transform of the gluon propagator is negative within a finite interval remains valid for $0 \leq N_f \leq 6$.

One would expect that the quark propagator behaves similarly; i.e. the quark propagator should violate positivity much like the gluon propagator. The corresponding Fourier transform for the quark propagator is

$$\tilde{S}(t, \vec{p}^2) = \int dp_0 \sigma_v(p_0^2 + \vec{p}^2) exp(ip_0 t) \geq 0 \tag{6.23}$$

with

$$\sigma_v(q^2) = \frac{A(q^2)}{q^2 A^2(q^2) + B^2(q^2)} \, . \tag{6.24}$$

The numerical results are shown in fig. 6.13. The left panel shows the results for the full propagator using the relation (6.23) and for comparison the right panel shows the results for the bare propagator, i.e. for the case that $A = 1$ and $B = m_0$. For both cases, i.e. for the full as well as for the bare propagator the results are purely positive. The oscillatory behaviour of the results for large values of $-t\sigma^{1/2}$ is simply due to the limited accuracy. - These oscillations flatten out as the numerical effort is increased. Therefore one has to conclude that the results for the Fourier transform σ_v do not show any indication that positivity is violated for the quark propagator.

However, it has to be emphasised that this is not a necessary condition; it is a sufficient one. The expression (6.20) might well be negative even if the Fourier transform (6.23) is

positive since the test function f is not constrained in any way. However, if the Fourier transform (6.23) is purely positive than there seems to be no easy alternative way to test for violations of positivity (which are still possible).

Chapter 7

Phenomenological Constraints on the Quark Propagator

The preceding chapters introduce and discuss the formalism and the results for the gluon-, ghost- and quark propagators using the Dyson-Schwinger approach. This approach yields the propagators only for space-like momenta which is the relevant momentum region for typical phenomenological applications, as e.g. bound state calculations within the Bethe-Salpeter framework [SB51], [Nak69][1]. These studies usually focus on observables like the bound state mass, (space-like) form factors or magnetic moments which are all essentially determined by the space-like properties of the quark propagator and the interaction of the constituents of the bound state (see e.g. [Tan97], [AvS00]). However, it turns out that production processes with large momentum transfer like e.g. kaon photoproduction are different since in these reactions the time-like properties of the quark propagator turn out to be of primary importance. Production processes like kaon photoproduction can therefore yield phenomenological constraints on the behaviour of the quark propagator in the time-like region.

The calculation of the cross section for kaon photoproduction has been carried out within the covariant diquark-quark model for baryons [AR95], [OHAR98], [OPvS00] which is briefly reviewed in the next section. Following this different model propagators that represent different possibilities to implement confinement at the level of the propagators are introduced. Then the kinematical particularities that distinguish production processes like kaon photoproduction from typical bound state calculations are examined. Having introduced the basic concepts the main objective of the present chapter, i.e. the calculation of the cross section for kaon photoproduction, can now be approached. This then allows to constrain the behaviour of the quark propagator in the time-like region [AAF$^+$00a].

[1] These studies do probe the propagators only for *very small* time–like momenta. See the discussion in section 7.3

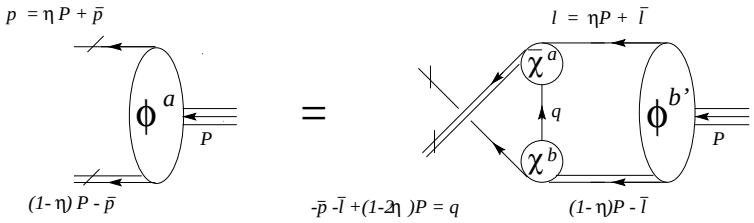

Figure 7.1: The coupled set of BSEs for the effective vertex functions ϕ^a.

7.1 Brief Review of the Diquark-Quark Model

In this section the basic concepts and the formalism of the covariant diquark–quark model is briefly recalled. Minor details and purely technical arguments that are not central to the present discussion can be found in the appendix B.3 or in [AAF+00a] and are not repeated here. A detailed discussion of the diquark–quark model can be found in [Oet00].

Starting from the Faddeev–formalism [Fad65] (see e.g. [Glö83] for a more recent introductory textbook) for three quarks and using two essential assumptions one arrives at a Bethe–Salpeter equation (BSE) that describes baryons as bound states of quarks and diquarks interacting via quark exchange. These assumptions are (i) all three–particle irreducible graphs can be omitted and (ii) the two–quark correlations can be approximated by separable correlations, the so–called *diquarks.* The present chapter is restricted to a short review of the main concepts whereas the actual derivation of the BSE for the effective baryon–diquark–quark vertex functions ϕ^a is detailed in [AAF+00a]. Using the definitions for total and relative momentum given as in figure 7.1 this integral equation reads

$$\phi^a_{i,\alpha}(\bar{p}_i, P) = \sum_{bb'} \int \frac{d^4\bar{l}}{(2\pi)^4}\, K^{ab}_{ij,\beta\alpha}(\bar{p}_i, \bar{l}, P)\; G^{\beta\beta'}_{j,bb'}(\bar{l}, P)\; \phi^{b'}_{j,\beta'}(\bar{l}, P) + (j \longleftrightarrow k)\ . \quad (7.1)$$

Here G_j describes the disconnected quark–diquark propagator

$$G^{\beta\beta'}_{j,bb'}(\bar{l}, P) = S^{\beta\beta'}_j(\eta P + \bar{l})\; D_{bb'}((1-\eta)P - \bar{l}) \;=\; S^{\beta\beta'}_j(l) D_{bb'}(P - l)\ . \quad (7.2)$$

Furthermore, the quark–diquark interaction kernel K contains (besides the propagator of the exchanged quark) the diquark amplitudes χ^a_i defined via the separability assumption

$$t_i(k_j, k_k; p_j, p_k) = \sum_{a,a'} \chi^a_i(k_j, k_k)\; D_{a,a'}(k_j + k_k)\; \bar{\chi}^{a'}_i(p_j, p_k) \quad (7.3)$$

of the quark–quark t–matrix. The kernel explicitly reads

$$\begin{aligned} K^{ab}_{ij,\beta\alpha}(\bar{p}, \bar{l}, P) &= \bar{\chi}^a_{i,\beta\gamma}(\bar{l} + \eta P, q)\; S^{\gamma\gamma'}_k(q)\; \chi^b_{j,\gamma'\alpha}(q, \bar{p} + \eta P) \\ &= \bar{\chi}^a_{i,\beta\gamma}(l, q)\; S^{\gamma\gamma'}_k(q)\; \chi^b_{j,\gamma'\alpha}(q, p)\ , \end{aligned} \quad (7.4)$$

with

$$q = (1-2\eta)P - \bar{p} - \bar{l} \;=\; P - p - l\,,$$

since $P = p_i + p_j + p_k$ and $\bar{l} = l - \eta P$. The above relations also indicate the independence of the momentum partition parameter η since the Jacobian of the transformation $\bar{l} \to l$ equals unity for fixed total momentum P.

For the solution of the BSE (7.1) one still has to choose the appropriate quantum numbers associated with baryons. One finds that the quark exchange (parameterised by the kernel K^{ab}) generates sufficient attraction to bind quarks and diquarks to baryons (see [CPB89], [Rei90] and [Bal90]). For identical quarks antisymmetrization is required when projecting onto baryon quantum numbers. Fortunately, this does not alter the algebraic form of the BSE (7.1). Rather, it simply implies that one may omit the single particle indices i on the quark propagators S_i. Only when caring about the discrete quantum numbers one has to revert to these indices since they specify the summation order over colour, flavour and Dirac–indices in (7.1). Furthermore the functional forms of the diquark propagators $D_{aa'}$ and the vertices χ_i^a do not depend on the quark labels. These independencies are already indicated in (7.2) and (7.4) as the quark labels for the momenta have been omitted.

In a self–consistent approach one would calculate the t–matrix from its own BSE. However, this is beyond the scope of the present investigation. Instead the t–matrix is modelled by diquark correlators which have an analytic structure such that no particle interpretation for the diquark exists. We will restrict ourselves to the scalar and axialvector channels as these comprise the minimal set to describe octet and decuplet baryons. Furthermore these channels are generally assumed to be the most important ones, see [RS00] and [AvS00] and references therein. The corresponding separable *ansatz* for the two–quark t–matrix reads

$$t_{\alpha\beta,\gamma\delta}(k_1,k_2;p_1,p_2) = \chi^5_{\alpha\beta}(\bar{k},P_2)\; D(P_2)\; \bar{\chi}^5_{\gamma\delta}(\bar{p},P_2) \;+ \\ \chi^\mu_{\alpha\beta}(\bar{k},P_2)\; D^{\mu\nu}(P_2)\; \bar{\chi}^\nu_{\gamma\delta}(\bar{p},P_2)\,. \quad (7.5)$$

Here we rewrite the diquark–quark vertices $\chi^{5[\mu]}$ as functions of relative, $\bar{k} = \sigma k_1 - (1-\sigma)k_2$, and total, $P_2 = k_1 + k_2 = p_1 + p_2$, momenta instead of the single quark momenta. In actual calculations, we choose for simplicity the symmetric momentum partition, i.e. $\sigma = 1/2$. Shifting the value of σ is possible, however, this complicates slightly the parameterization of diquark correlations, see the discussion below (7.12) and in [OPvS00].

The diquark propagators in the scalar and the axialvector channel are modelled as

$$D(P) \;=\; -\frac{1}{P^2 + m_{sc}^2}\, f\left(\frac{P^2}{m_{sc}^2}\right)\,, \quad (7.6)$$

$$D^{\mu\nu}(P) \;=\; -\frac{1}{P^2 + m_{ax}^2}\left(\delta^{\mu\nu} + (1-\xi)\frac{P^\mu P^\nu}{m_{ax}^2}\right) f\left(\frac{P^2}{m_{ax}^2}\right)\,. \quad (7.7)$$

Hereby the dressing function $f(P^2/m^2)$ will be chosen to cancel the singularity on the real time-like axis thus effectively implementing confinement. Different possible forms for f will be discussed in section 7.2 and used in the subsequent sections. Note that the choice

$f(P^2/m^2) = 1$ and $\xi = 0$ corresponds to the free propagators of spin–0 and spin–1 particles. In general, the dressing functions f are different in the scalar and axialvector channels as well as they are distinct from the one for the quark propagator. For simplicity, however, identical dressing functions are assumed for all propagators. As the present investigation neglects any axialvector diquark loops it is sufficient for the present purpose to use $\xi = 1$, see [OHAR98] where it has been shown that choosing $\xi = 1$ leads to almost identical results for baryon amplitudes as $\xi = 0$.

If diquark poles existed in the t matrix, the diquark–quark vertices χ and χ^μ would on-shell ($P^2 = -m^2_{sc[ax]}$) correspond to diquark Bethe–Salpeter vertex functions. These vertex functions have a finite extension in momentum space and fall off fast enough to render all integrals finite. Empirically one assumes that the corresponding scale is linked to the (inverse) proton radius. The conjugate vertex functions $\bar{\chi}$ are obtained by charge conjugation,

$$\bar{\chi}^5(p,P) = C\,\left(\chi^5(-p,-P)\right)^T\,C^T\,, \tag{7.8}$$

$$\bar{\chi}^\mu(p,P) = -C\,\left(\chi^\mu(-p,-P)\right)^T\,C^T\,, \tag{7.9}$$

where T denotes the transpose.

In the following the vertex functions are constructed explicitely. They must be antisymmetric under the interchange of the two quarks. This implies

$$\chi^{5[\mu]}_{\alpha\beta}(\bar{p},P) = -\chi^{5[\mu]}_{\beta\alpha}(-\bar{p},P)\Big|_{\sigma\leftrightarrow(1-\sigma)}\,. \tag{7.10}$$

Any two quarks within a baryon belong to the colour antitriplet representation. Thus the diquark–quark vertices are proportional to the antisymmetric tensor ϵ_{ABD}. Here A and B are the colour indices of the quarks whereas D labels the colour of the diquark. Furthermore the scalar diquark is antisymmetric while the axialvector diquark is symmetric in flavour. We maintain only the dominant components with regard to the structure in Dirac space.[2] These are the antisymmetric matrix $(\gamma^5 C)$ for the scalar diquark and the symmetric matrices $(\gamma^\mu C)$ for the axialvector diquark. Considering, for the time being, only two flavours the vertices then read[3]

$$\chi^5_{\alpha\beta}(\bar{p},P)\big|_{\sigma=1/2} = \chi^5_{\alpha\beta}(\bar{p}) = g_s(\gamma^5 C)_{\alpha\beta}\;V(\bar{p}^2)\;\frac{(\tau_2)_{ab}}{\sqrt{2}}\,\frac{\epsilon_{ABD}}{\sqrt{2}}\,, \tag{7.11}$$

$$\chi^\mu_{\alpha\beta}(\bar{p},P)\big|_{\sigma=1/2} = \chi^\mu_{\alpha\beta}(\bar{p}) = g_a(\gamma^\mu C)_{\alpha\beta}\;V(\bar{p}^2)\;\frac{(\tau_2\tau_k)_{ab}}{\sqrt{2}}\,\frac{\epsilon_{ABD}}{\sqrt{2}}\,. \tag{7.12}$$

Choosing the scalar function V to depend only on the squared relative momentum $\bar{p}^2$, these vertices are indeed antisymmetric with respect to exchange of quark labels for the partition

[2] The complete Dirac structure for the scalar diquark containing four independent tensors can be obtained by analogy from the one for pseudoscalar mesons. The complete Dirac structure for the axialvector diquark consists of twelve independent terms, four longitudinal and eight transverse ones.

[3] In the compact notation the indices α and β of $\chi_{\alpha\beta}$ not only contain the Dirac labels but also those for flavour and colour.

$\sigma = 1/2$. Otherwise a parameterization of V would depend on both $\bar{p}^2$ and $\bar{p} \cdot P$ in order to comply with antisymmetrization [OPvS00, MR97]. However, complete independence for observable quantities on σ could only be obtained by solving the BSE for the two–quark t–matrix in which case the scalar functions V could depend on the quantity $(\bar{p} \cdot P)^2$ (for $\sigma = 1/2$) which is symmetric under quark exchange. In the actual calculations we will use a multipole type ansatz

$$V(x) = V_n(x) \quad = \quad \left(\frac{\lambda_n^2}{\lambda_n^2 + x} \right)^n . \tag{7.13}$$

The overall strength of the diquark correlations given in (7.11) and (7.12) is governed by the 'diquark-quark coupling constants' g_s and g_a. They could be determined by either imposing the canonical Bethe–Salpeter norm condition [Nak69] on $\chi^{5[\mu]}$ or by the solution to the differential Ward identity for the diquark–photon vertex which is sensitive to the substructure of the diquarks [OAvS00]. For simplicity, we will fix g_s from fitting the nucleon mass. When including axialvector diquarks we will assume the ratio $g_a/g_s = 0.2$ as suggested by the results that are reported in [OAvS00]. In this manner the baryon BSE (7.1) becomes an eigenvalue problem for the coupling constants g_s and g_a.

Note that by parameterising the quark–quark t–matrix no reference to the nature of the quark–quark interaction has been made. For example, to quantitatively include pionic effects one would have to solve DSEs for the quark propagator and the BSE with explicit pion degrees of freedom. Studies within the Nambu–Jona–Lasinio model [NJL61a], [NJL61b] using diquark–quark correlations either in a soliton background [ZAWR97] or with explicit pion interaction between the quarks [Ish98] lead to a substantial gain in the binding energy. Since the coupling constant g_s is determined from the nucleon mass, those studies suggest that the inclusion of pion degrees of freedom would merely lead to a shift of this constant.

Equipped with the separable form of the two–quark correlations (see (7.5)) and the functional form of the scalar and axialvector diquark correlations in (7.11) and (7.12), it is now possible specify the effective BSE for the nucleon.

Upon attaching quark and diquark legs to the vertex functions ϕ one obtains the Bethe–Salpeter wave functions ψ. Equation (7.1) can then be rewritten as a system of equations for wave– and vertex functions:

$$\int \frac{d^4k}{(2\pi)^4} G^{-1}(p,k,P) \begin{pmatrix} \Psi^5(k,P) \\ \Psi^{\mu'}(k,P) \end{pmatrix} = 0 . \tag{7.14}$$

Here $G^{-1}(p,k,P)$ is the inverse of the quark–diquark four–point function which results from the quark exchange[4]. It is the sum of the disconnected part and the interaction kernel which contains the quark exchange,

$$\begin{aligned} G^{-1}(p,k,P) = (2\pi)^4 \, \delta^4(p-k) \, S^{-1}(p_q) \, \circ D^{-1}(p_d) \\ - \frac{1}{2} \begin{pmatrix} -\chi^5(p_2^2) \, S^T(q) \, \bar{\chi}^5(p_1^2) & \sqrt{3} \, \chi^{\mu'}(p_2^2) \, S^T(q) \, \bar{\chi}^5(p_1^2) \\ \sqrt{3} \, \chi^5(p_2^2) \, S^T(q) \, \bar{\chi}^{\mu}(p_1^2) & \chi^{\mu'}(p_2^2) \, S^T(q) \, \bar{\chi}^{\mu}(p_1^2) \end{pmatrix} \end{aligned} \tag{7.15}$$

[4]The discrete labels have been omitted to ease the notation.

where '$\circ$' denotes simple multiplications without any contractions because the thus multiplied operators act on different (di)quarks. The flavour and colour factors have been made explicit and therefore $\chi^5(p^2)$ and $\chi^\mu(p^2)$ from now on only represent the Dirac structures of the diquark–quark vertices (multiplied by the invariant function $V_n(p^2)$, cf. (7.13)). The freedom to partition the total momentum between quark and diquark introduces the parameter $\eta \in [0,1]$ with $p_q = \eta P + p$ and $p_d = (1-\eta)P - p$. The momentum of the exchanged quark is then given by $q = -p - k + (1-2\eta)P$. The relative momenta of the quarks in the diquark vertices χ and $\bar{\chi}$ are $p_2 = p + k/2 - (1-3\eta)P/2$ and $p_1 = p/2 + k - (1-3\eta)P/2$, respectively. Invariance under (four dimensional) translations implies that for every solution $\Psi(p, P; \eta_1)$ of the BSE a family of solutions exists that have the form $\Psi(p + (\eta_2 - \eta_1)P, P; \eta_2)$. Considering the BSE as a linear eigenvalue problem for the wave function Ψ in the coupling constant g_s, translation invariance requires the coupling constant eigenvalue to be independent of η once a bound–state mass $-P^2 = M^2$ is fixed. This independence is exactly what one observes in the numerical solutions of the BSE, provided the analytic form of the dressing functions, eq (7.26)–(7.28), is used. However, the η–independence is lost when substituting non–analytic propagators such as those parameterised by the dressing function f_3 which will be introduced below (see (7.29)). The reason being that Cauchy's theorem does not apply to non–analytic functions. The difference in the eigenvalues of the BSE under the variation of η can be shown to equal a contour integral in the complex p–plane. This integral vanishes only if the integrand is an analytic function. However, when choosing $d > 5$ in (7.29), the propagator resembles the free propagator in a large domain thereby mitigating the η–dependence.

Bethe-Salpeter equations have been investigated for decades; the first investigations focused on model theories like e.g. ϕ^3-theory (see the original work [Wic54], [Cut54] and the review [Nak69]) in order to study the basic characteristics of the BSE itself. Later on it became feasible to apply the BSE to more realistic models which describe mesons and baryons, see e.g. the recent reviews [RW94] and [AvS00] and references therein. It has been first discussed in ref. [Kau69] and extensively studied in [AA99] that the BSE (solved as an eigenvalue problem for the coupling constant) can yield complex solutions for the coupling constant g^2 for excited states. The origin of these unphysical solutions has been examined and it has been shown that these solutions occur only outside the domain of validity of the approximation that has been used for the kernel K. The reason being that the approximations for the kernel and for the propagators that enter the BSE have to be mutually consistent, see [AA99] for details.

The structure of the equations for the octet baryons is similar to that of the nucleon (7.14). However, the number of Dirac structures Φ^5 and Φ^μ increases due to the possible different quark–diquark flavour configurations. These equations are given in full detail in [OHAR98] and [Oet00]. Allowing for flavour symmetry breaking, that is induced by a difference between the masses of strange quark and up/down quark, discriminates vertex functions Φ^5 and Φ^μ with different diquark configurations [OHAR98]. The Λ hyperon is of particular interest for the production process $p\gamma \to K\Lambda$ to be discussed in the following. Therefore it is appropriate to more closely examine the different correlations that make up the Λ. One

finds the correlations:

$$\Phi_\Lambda \sim \left(\Phi^5_{S_1}\,, \quad \Phi^5_{S_2} \quad \text{and} \quad \Phi^\mu_A\right)\,. \tag{7.16}$$

which are distinguished by symmetry and diquark content. In the following scalar diquarks and symmetrised axialvector diquarks are denoted by square brackets $[\dots]$ and curly brackets $\{\dots\}$ respectively. Using this notation the scalar correlations S_1 and S_2 can be written in the form

$$S_1 = \{d[us] - u[ds]\}/\sqrt{2}\,, \qquad S_2 = s[ud] \tag{7.17}$$

and the axialvector correlation reads

$$A = [d\{us\} - u\{ds\}]/\sqrt{2}\,. \tag{7.18}$$

Note that broken $SU(3)$–flavour symmetry induces a component of the total antisymmetric flavour singlet $\frac{1}{\sqrt{3}}\,[[su]d + [ud]s + [ds]u]$ into wave and vertex functions. In non–relativistic quark models with $SU(6)$ symmetry such a component is forbidden by the Pauli principle. However, these flavour singlet admixtures cannot be avoided since the lower components in the baryon bi–spinors are non–vanishing. In actual calculations the singlet contributions turn out to be small [OHAR98].

The strong form factor $g_{KN\Lambda}$ enters the calculation of the cross section for kaon photoproduction. It is therefore suggestive to first discuss the basic formalism for the calculation of these form factors.

Figure 7.2 shows the dominant contributions to the strong form factors. Here the meson directly couples to one of the baryon constituents. Keeping only such direct couplings while omitting those to the exchanged quark defines the impulse approximation that is adopted here[5]. The two diagrams shown in fig. 7.2 actually correspond to a number of diagrams which differ by the type of the involved diquarks. Let us first consider the process in which the meson couples to the quark. The diquark has to be a scalar ud–diquark since this is the only overlap between the wave–function of the proton and the wave–function of the Λ. The second important contribution represents the coupling of the meson to the diquark; the diquark associated with the momenta p_+ or p_- may be scalar or axialvector.

The meson–quark vertex that enters the calculation of the diagrams shown in fig. 7.2 is the solution of a separate BSE which has been extensively studied, see [AvS00] and references therein. In the chiral limit this BSE becomes formally identical to the DSE for the scalar self energy function $B(p^2)$ when only the leading Dirac structure is considered, i.e.

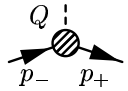

$$= \Gamma_m(p_-, p_+) = \frac{i}{2f}\gamma_5\left\{B(p_+^2) + B(p_-^2)\right\} \tag{7.19}$$

where f is the meson decay constant.

[5]Contributions to the nucleon electromagnetic form factors beyond the impulse approximation that arise from the coupling to the exchanged quark are discussed in [OAvS00], [OPvS00] and [Oet00].

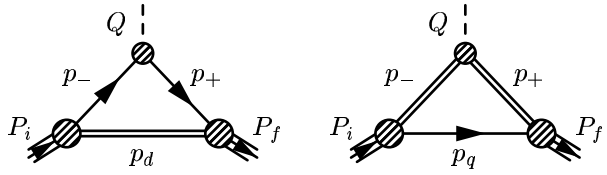

Figure 7.2: Dominant diagrams for the strong form factor $g_{KN\Lambda}$. The incoming proton carries the momentum P_i while P_f is associated with the outgoing Λ hyperon. The incoming meson carries the momentum Q and couples to the quark (*left panel*) or to the diquark (*right panel*).

The structure of the meson–diquark vertices is constrained not only by Lorentz covariance and parity but also by the Bose–statistics for the two involved diquarks. The pseudoscalar meson axialvector diquark vertex is thus parameterised as

$$\Gamma^{\rho\lambda}_{aa} = -i\frac{\kappa_{aa}}{2M}\frac{m}{f}\epsilon^{\rho\lambda\mu\nu}(p_- + p_+)^\mu Q^\nu \,. \tag{7.20}$$

Here the superscripts ρ,λ denote the Lorentz indices of the incoming and outgoing axialvector diquark, respectively and the momenta are defined as indicated in fig. 7.2. The nucleon mass M has been introduced to define the dimensionless coupling constant κ_{aa}. Furthermore m is the average of the masses of the constituent quarks in the diquarks. The corresponding ansatz for the scalar–axialvector transition reads,

$$\Gamma^{\rho}_{sa} = -\kappa_{sa}\frac{m}{f}Q^\rho \,, \tag{7.21}$$

where the definitions are those of (7.20) and κ_{sa} is again a dimensionless constant[6] specifying the overall strength of the vertex. The vertex (7.21) describes the coupling of the diquarks to the derivative of the pseudoscalar mesons. Such a construction is suggested by the chiral structure of the strong interactions that can be written as expansion in the derivatives of the Goldstone bosons, at least in the chiral limit.

Having introduced all ingredients one may now proceed and compute the diagrams in fig. 7.2. According to the Mandelstam formalism [Man55] the diagram shown in the left panel translates into an expression of the form

$$\int \frac{d^4q}{(2\pi)^4}\,\bar{\Phi}_f(q_f,P_f)S(p_+)\Gamma_m(p_-,p_+)S(p_-)\Phi_P(q,P_i)D(p_d)\,, \tag{7.22}$$

where only the general structure has been indicated, i.e. indices that are associated to the coupling and propagation of axialvector diquarks have been omitted. The conjugate vertex function, $\bar{\Phi}$ is related to the vertex function Φ according to:

$$\bar{\Phi}(p,P) = \eta_d\, C\, \Phi(-p,-P)^T\, C^T \tag{7.23}$$

[6]These coupling constants are fixed using a procedure that is detailed in [Oet00].

with $\eta_d = 1$ and $\eta_d = -1$ when the involved diquark is respectively of scalar or axialvector type. The loop momentum is denoted by q and the momenta are defined as follows

$$p_- = q + \eta P_i\,, \quad p_+ = p_- + Q = q_f + \eta P_f \quad \text{and} \quad p_d = -q + (1-\eta) P_i\,. \tag{7.24}$$

Again, $\eta \in [0,1]$ is the momentum partition parameter. The diagram in the right panel of fig. 7.2 translates into a corresponding expression where quark and diquark propagators need to be exchanged as compared to (7.22).

7.2 Confining Model Propagators

The naïve use of perturbative quark and diquark propagators leads to asymptotic states in the spectrum that would have to be interpreted as free (di)quarks[7]. Hence baryons would decay into quarks unless kinematically bound and this would contradict the confinement phenomenon. The present chapter focuses on the idea of incorporating confinement into the diquark-quark model by suitable modifications of the quark and diquark propagators. These propagators are modified by multiplicative dressing functions (as indicated in (7.6) and (7.7)) to remove the poles that would occur in the perturbative propagators at the (di)quark masses. This allows to calculate the spectrum not only of octet but also decuplet baryons [OHAR98] and (space-like) nucleon form factors [BRS00], [BRS$^+$99]. However, there would be yet other unphysical shortcomings due to the use of perturbative quark and diquark propagators: production processes with *time-like* momentum transfers of the order of 1GeV could not be described properly. Again, the free–particle poles of quarks and diquarks would cause unphysical thresholds in these processes. An appropriate modification of these propagators would not only remove the unphysical thresholds but also serve as an effective description of the strong interaction.

The dressing functions that will be specified below implement different possibilities to remove the singularities for real time-like momenta in the quark and diquark propagators. Either these singularities are absent or their contributions cancel in some way [AvS00]. The qualitative behaviour described can be encoded in the following models (which are certainly not the only possibilities) for the quark propagator in Euclidean space,

$$S^{(k)}(p) \;=\; \frac{i\not{p} - m_q}{p^2 + m_q^2}\, f_k\left(\frac{p^2}{m_q^2}\right)\,, \qquad k = 0,\ldots,3\,, \tag{7.25}$$

with

$$f_0(x) \;=\; 1 \qquad \text{(bare propagator)}\,, \tag{7.26}$$

$$f_1(x) \;=\; \frac{1}{2}\left\{\frac{x+1}{x+1-i/d} + \frac{x+1}{x+1+i/d}\right\}\,, \tag{7.27}$$

$$f_2(x) \;=\; 1 - \exp\left[-d\,(1+x)\right]\,, \tag{7.28}$$

$$f_3(x,x^*) \;=\; \tanh\left[d\,(1+x)\,(1+x^*)\right]\,. \tag{7.29}$$

[7] For a discussion of diquark confinement see the original work [BRS96] and the review in [Hel98].

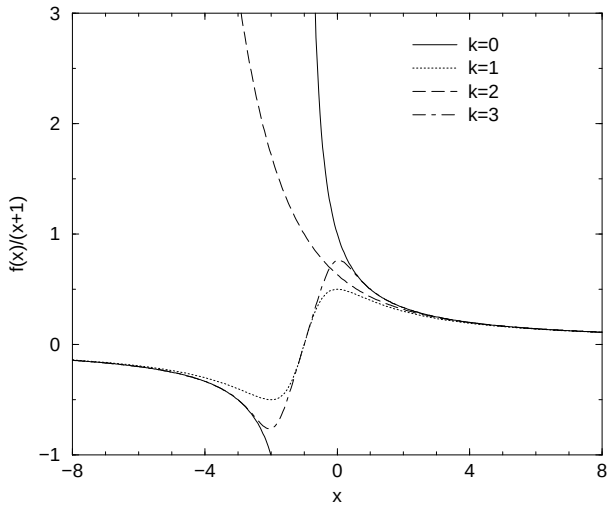

Figure 7.3: The propagator functions, $\tilde{f}_k(x) = f_k(x)/(x+1)$ for real x and for $k = 0, \ldots, 3$, cf. eqs (7.26)–(7.29). The solid line corresponds to the free propagator. Here we have set $d = 1$.

The trivial dressing function f_0 corresponds to the bare propagator. This case is considered only for comparison.

The propagator (7.27) has complex conjugate poles [Sti96] such that corresponding virtual excitations cancel each other in physical amplitudes. Hereby m has the status of a parameter that would be interpreted as the quark mass if and only if the poles were on the real axis.

In a second scenario (7.28), the dressing function is chosen such that the propagators are entire functions and non–trivial for all finite complex momenta. Then, however, they must have an essential singularity at $|p|^2 = \infty$ [EI93, BRS$^+$99]. This type of dressing function has been used quite successfully to describe the space-like aspects of baryons within the covariant diquark-quark model, see e.g. [HAOR97] and [OHAR98].

Third, it might be helpful to approximate propagators by non–analytic functions (7.29) and constrain them such that they asymptotically behave like $1/|p|^2$ for both, large space-like and time-like momenta. Since we enforce the propagators to be free of poles, they must be non–analytic functions depending on both the particle momentum p and its complex conjugate p^*. Consequently the quark–photon and quark–meson vertices are non–analytic and translation invariance is lost in the solutions to the nucleon BSE. These issues have been detailed in section 7.1.

In fig. 7.3 the dressing functions are plotted in the form $\tilde{f}_k(x) = f_k(x)/(x+1)$ for $k = 0, \ldots, 3$ for real x. Note that these dressing functions are real in that case. One observes that $\tilde{f}_1(x)$ and $\tilde{f}_3(x)$ change sign while the function $\tilde{f}_2(x)$ increases drastically. For asymptotically large space-like momenta the three model propagators $S^{(k)}$, $(k = 1, 2, 3)$ match up with the bare propagator $S^{(0)}$. The present investigation focuses on the phe-

nomenological implications of the thus modified propagators.

7.3 Kinematical Particularities of Production Processes

The calculation of bound state masses within the Bethe-Salpeter framework (essentially) relies on the space-like properties of the propagators of the constituents. However, for the description of production processes like $p\gamma \to \Lambda K$ the behaviour of the propagators of the constituents in the *time-like* region turns out to be of primary importance. In principle these propagators can be calculated using DSEs [AvS00] and also respective lattice measurements should be available in the near future; for preliminary results see e.g. [SW01, HKLW98]. Both methods comprise the non–perturbative dynamics and should therefore give the basic ingredients to describe hadrons as bound state of quarks. However, both approaches are set up in Euclidean space and one has to revert to extrapolations when the propagators are to be used for time-like momenta. If one would like to analytically continue form Euclidean space back to Minkowski space one would have to know the propagators not only on the real axis but in a region of the complex plane. In order to calculate amplitudes of physical processes between on–shell particles using the Euclidean Bethe–Salpeter formalism the temporal components of the external momenta must be purely imaginary thus leading to complex internal momenta. In these calculations therefore the structure of the propagators in the complex momentum plane is essential. As repeatedly mentioned: confinement is understood (within this phenomenological context) as the absence of poles on the time-like q^2–axis in the propagators of coloured states.

The BSE is most conveniently solved in the rest frame of the bound state where the total momentum of the bound state is $P = (\vec{0}, iM)$. In (7.14) the loop momentum k relative between quark and diquark is chosen to be real. Hence the temporal component of the quark momentum $k_q = \eta P + k$ becomes complex. Therefore the solution of the BSE 'probes' the quark propagator at complex momenta; more precisely: within a parabola shaped region, see fig. 7.4. The values of k_q^2 that are covered when integrating over k lie within a parabola that opens towards the space-like axis, cf. fig. 7.4. The intercept of the parabola with the real axis is at (small) time-like $k_q^2 = -(\eta M)^2$. Thus, solving the BSE mainly probes the behaviour of the quark propagator for space-like momenta.

The solution of the BSE yields the vertex functions that are the basic ingredients to all further calculations, like e.g. the calculation of the cross section for production processes. Having examined the momentum regime relevant to the solution of the BSE itself we now focus on the momentum regime that is 'probed' in the calculation of production processes like kaon photoproduction. A contribution to the reaction $p\gamma \to \Lambda K$ that involves a quark loop is shown in fig. 7.5. It turns out that it suffices to consider a parabola shaped region of the complex q^2–plane (i.e. it is sufficient to consider only this momentum and ignore the others). This can be understood in at least two ways: One could use the wave–functions rather than the vertex–functions for the calculation of the diagram. In this case the propagators that depend on p_q, k_q and p_d are included in the wave–functions and there would be no necessity to treat them separately. Nevertheless, considering the propagators $S(p_q), S(q), S(k_q)$ and $D(p_d)$ separately one finds that among all the internal momenta in

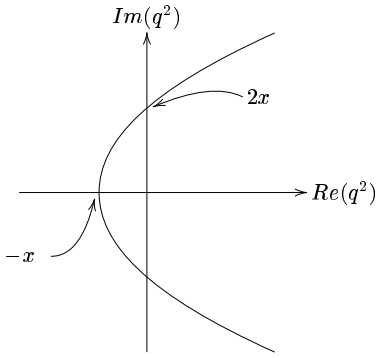

Figure 7.4: The complex q^2–plane. The interior of the parabola is needed for the calculation of the diagram in fig. 7.5, x is defined as $x = (\eta M + E)^2$. Note that in the case of the BSE one has $x = \eta^2 M^2$.

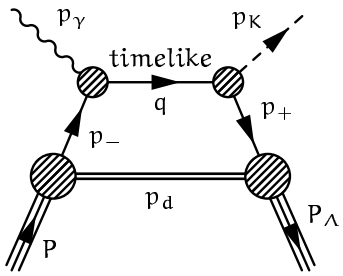

Figure 7.5: Main contribution to kaon photoproduction $p\gamma \to K\Lambda$,

the diagram it is q that reaches farthest in the time-like regime. Thus the following analysis for p_q and k_q would yield less restrictive conditions.

From the momentum routing shown in fig. 7.5 one has:

$$q = p_- + p_\gamma = \eta P + l + p_\gamma \tag{7.30}$$

where η is again the momentum partition parameter ($p_- = \eta P + l,\ p_d = (1-\eta)P - l$) and l denotes to the loop momentum. The loop momentum is chosen to be real which implies that the external momenta like P and p_γ must have an imaginary temporal component in order to correspond to physical particles. The following kinematical considerations refer to the proton rest frame and assume that the photon propagates along the y-axis,

$$P = (\vec{0}, iM), \quad p_\gamma = (0, E, 0, iE), \quad l = (\vec{l}, l_4)\ . \tag{7.31}$$

Hence the momentum entering the quark propagator becomes

$$q^2 = \left(-\eta^2 M^2 + l^2 - 2\eta M E + 2E l_y\right) + i\,(2\eta M + 2E)\, l_4 \tag{7.32}$$

where the real and imaginary parts of q^2 have been separated. This shows that we need to know the propagator $S(q^2)$ at complex q^2 in order to be able to compute the handbag diagram shown in fig. 7.5. The set of values of q^2 that occur is illustrated in fig. 7.4. The situation seems to be quite parallel to what we found for the BSE; in both cases we need to know the propagators in a parabola shaped region of the complex plane. The intercept with the imaginary axis is in both cases minus two times the intercept with the real axis (cf. fig. 7.4). However, there is one important difference. For the production processes the intercept with the real axis does depend on the photon energy E, more precisely: $x = (\eta M + E)^2$ whereas for the BSE one has $x = (\eta M)^2$. Thus for $E = 0$ the computation of the handbag diagram shown in fig. 7.5 uses the same region of the complex plane that is necessary to solve the BSE. However, for $E > 0$ the parabola is shifted in the direction of the negative real axis.

The threshold for kaon photoproduction is at E slightly less than 1GeV and the cross section has been measured [T$^+$98] up to $E \approx 2$GeV. This implies that the handbag diagram 'probes' the quark propagator *much* farther into the time-like region than the BSE itself.

The analogous kinematical analysis for strangeness–production $pp \to pK\Lambda$ (see right panel of fig. 7.4) exhibits the same qualitative features. That process as well 'probes' a parabola shaped subset of the complex plane, whereby the parabola is somewhat broader than the one in figure 7.4. However, there is again an important difference: for typical kinematical situations the parabola does extend only up to $q^2 \approx -0.53\text{GeV}^2$ into the time-like region. That is, the reaction $pp \to pK\Lambda$ 'probes' the propagators in essentially the same region as the BSE does. It is therefore not as sensitive as kaon photoproduction to the behaviour of the propagator in the time-like region.

The main conclusion of the above discussion is that certain production processes are significantly more sensitive to the structure of the quark and diquark propagators than e.g. the baryon spectrum as calculated within the Bethe-Salpeter formalism. Hence the study of such processes should provide important information about these propagators.

7.4 Results for Kaon Photoproduction

This section is divided into two parts; first the model parameters (see table 7.1) are fixed from the octet baryon masses and the nucleon magnetic moments. The numerical details for solving the octet baryon BSEs and the computation of the form factors are thoroughly discussed in [Oet00]. Then the results for the strong form factor $g_{KN\Lambda}$ are shortly discussed since they enter the calculation of the cross section for kaon photoproduction. The results for $\gamma p \to K\Lambda$, which are the main objective of the present investigation, are then presented in the second part of this section. The results that are discussed here have been first published in [AAF$^+$00a].

Within the required numerical accuracy it has been assured that the above described independence of the octet masses of the momentum partition parameter η when analytical propagators are used. As argued before, this invariance does not hold for non–analytic propagators. In these cases η has been chosen to be close to its non–relativistic value $m_q/(m_q + m_d)$ where m_q and m_d denote quark and diquark mass parameters of the

	I	II	III	IV	V	VI	expt.
diquark:		only scalar			scalar and axialvector		
f_i	2	1	1	3	1	3	
d	2.0	8.0	4.0	6.0	4.0	6.0	
$m_u = m_d$[GeV]	0.40	0.45	0.45	0.52	0.45	0.52	
m_s [GeV]	0.64	0.70	0.69	0.75	0.67	0.72	
ζ	0.70	0.95	0.92	0.97	0.92	0.97	
λ^2 [GeV^2]	0.25	0.1	0.1	0.1	0.1	0.1	
μ_p	2.83	2.47	2.64	2.32	2.70	2.33	2.79
μ_n	−2.37	−2.15	−2.32	−2.08	−2.08	−1.82	−1.91
octet masses, $M_N = 0.939$ GeV fixed							
Λ [GeV]	1.13	1.12	1.12	1.12	1.13	1.12	1.12
Σ [GeV]	1.30	1.27	1.29	1.30	1.22	1.21	1.19
Ξ [GeV]	1.37	1.37	1.39	1.36	1.37	1.33	1.32

Table 7.1: The six parameter sets of the model investigated here and the respective results for the nucleon magnetic moments and the octet masses. Calculations using the first four sets involve only scalar diquarks, whereas the sets V and VI also include axialvector diquarks. The parameter ζ determines the diquark mass (scalar and axialvector), $m_d = \zeta(m_a + m_b)$, with the mass parameters $m_{a,b}$ of its constituent quarks. The parameter λ determines the width of the diquark amplitudes, see (7.13). For set I the corresponding shape of the amplitudes was chosen to be a quadrupole ($n = 4$), for the other sets we fixed it to be a dipole ($n = 2$).

flavour channel associated with the considered baryon. This choice is natural since other ones yield larger eigenvalues of the BSE. The physical nucleon mass is used to fix the scalar diquark coupling g_s and the Λ-mass to determine the strange quark mass parameter m_s. By reproducing the phenomenological dipole fit for the proton electric form factor, G_E one essentially fixes the diquark width λ.

Table 7.1 lists the six parameter sets that will be employed to compute the observables of production processes later on. The first four sets are restricted to the dominant scalar diquark correlations. Set I refers to the pole–free exponential dressing function, f_2, while the sets II and III are associated with dressing functions of the Stingl type, f_1 (cf. eqs. (7.27) and (7.28)). These two sets differ by the value of d that characterises the separation of the complex conjugate poles. Finally set IV assumes the non–analytic pole–free dressing function, f_3 (cf. (7.29)). The dressing of the propagators increase the predicted proton magnetic moment when all other model parameters remain unchanged. Using the parameters of set II but free propagators yields $\mu_p = 2.27$ while the Stingl–type propagators result in $\mu_p = 2.46$ and $\mu_p = 2.64$ for $d = 8.0$ and $d = 4.0$, respectively. The magnetic moment of the proton falls a little short for the sets II and IV. The overall picture emerges that the

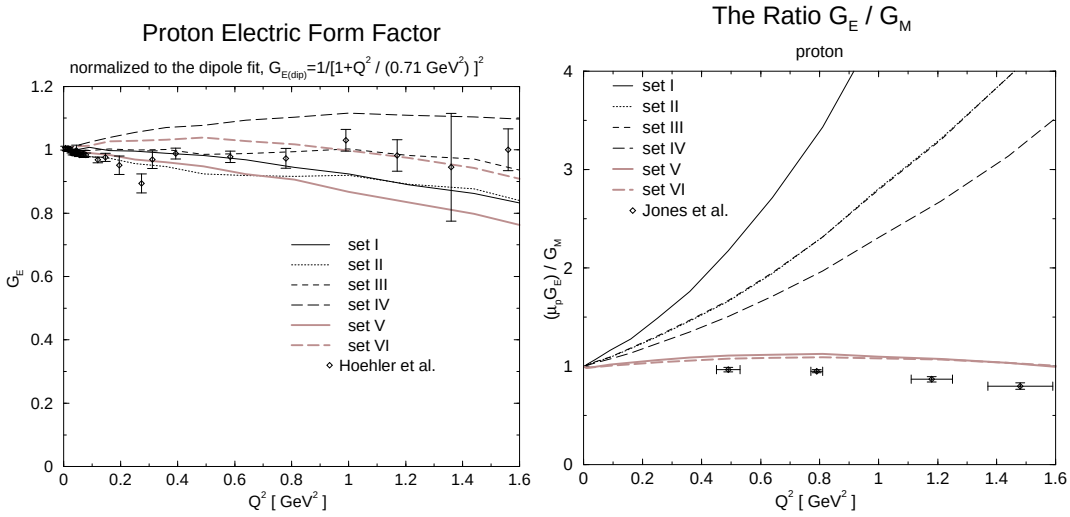

Figure 7.6: *Left panel:* Proton electric form factor normalized to the dipole fit. The experimental data are taken from ref. [H$^+$76]. *Right panel:* The ratio $(\mu_p G_E)/G_M$ for the proton with the experimental data published in ref. [J$^+$00].

restriction to only scalar diquark correlations produces too large ratios $|\mu_n/\mu_p|$ and rather large mass splittings between the octet baryons, especially between Σ and Λ.

As shown in fig. 7.6 all sets reasonably well reproduce the electric form factor, G_E. The results are confined within a region that is characterized by less than approximately 15% deviation from the dipole fit. This deviation, although rectifiable by refining the time–consuming parameter search, is of no significance for the conclusions that will be drawn from the results for the production processes. This will become clear from the discussions below.

The calculations that employ the parameters sets V and VI include a moderate admixture of axialvector diquarks, $g_a/g_s = 0.2$. For simplicity the axialvector diquark masses are chosen identical to the scalar ones. Here, the Stingl form f_1 (set V) and the non-analytic form, f_3 (set VI) are of particular interest, since later it will be shown that the exponential form, f_2 produces unacceptable results for the production processes. Upon inclusion of the axialvector diquark the good description of G_E remains unchanged while the ratio $|\mu_n/\mu_p|$ and the mass splitting between Σ and Λ even improve. For set VI the predicted octet masses are almost indistinguishable from their experimental values. As already observed in [OAvS00] and as is exhibited in the right panel of fig. 7.6, the ratio G_E/G_M calculated with axialvector diquarks included comes considerably closer to the experimental values than in a calculation that omits these degrees of freedom (sets I–IV). As explained in [OAvS00], increasing the strength of axialvector correlations in the proton forces the ratio G_E/G_M to bend to lower values at large photon virtualities. This also suggests that in order to precisely reproduce the empirical result one would need a slightly larger axialvector coupling than the assumed $g_a/g_s = 0.2$.

All sets predict the maximum of the neutron electric form factor to lie between $0.025 <$

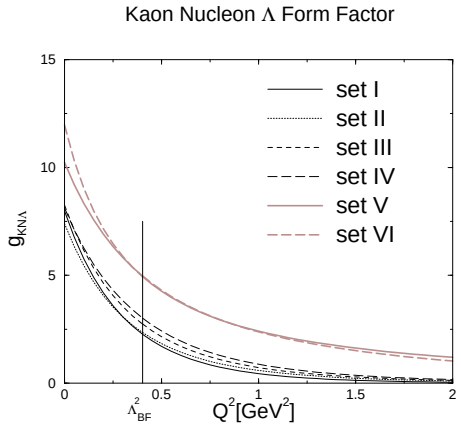

Figure 7.7: Results for the strong form factor $g_{KN\Lambda}$. The parameter sets (I–VI) are defined in table 7.1. For $Q^2 < \Lambda^2_{BF}$ are obtained from a rational fit as explained in the main text. (See [AAF$^+$00a] and [Fis99] for a detailed discussion.)

$G_E < 0.04$. This is only about half the value extracted from recent experiments [P$^+$99, O$^+$99]. Within this model approach improved descriptions for this form factor can be found in [OPvS00] and [OAvS00].

In a previous study [OAvS00] that employed free quark and diquark propagators it was not possible to reproduce the nucleon magnetic moments and the Δ mass simultaneously. The kinematical binding of the Δ required a large constituent quark mass, $m_q = 0.43$ GeV, which in turn decreased the magnetic moments (in magnitude). Furthermore the use of free propagators enforced moderate axialvector diquark contributions (about 25%) to properly describe the ratio G_E/G_M of electric and magnetic form factors for Q^2 up to 2GeV^2. In contrast, the introduction of dressing functions for the quark–photon vertex (see [AAF$^+$00a] for details) allows to choose rather large *up* quark mass parameters around $m_u = 0.45$ GeV and still obtain a proton magnetic moment that agrees with experiment reasonably well.

Figure 7.7 displays the results for the form factor $g_{KN\Lambda}(Q^2)$ that will be used in the calculation of the cross section for kaon photoproduction.[8] These results have been calculated in the Breit–frame which is special because the calculations cannot be performed below a certain momentum for the meson. This lower bound is given by: $Q^2 \geq \Lambda^2_{BF} = M^2_\Lambda - M^2_N \approx 0.4\text{GeV}^2$ and below this momentum one has to use a (rational) extrapolation. For the special case $Q^2 = 0$ it has been explicitely verified that the thus obtained results are equal to the corresponding results that are obtained in the lab–frame. The prediction for $g_{KN\Lambda}(Q^2 = 0)$ is comparable to those found by QCD-sum rule or Skyrme model calculations but somewhat smaller than the chiral bag model result, cf. [JC99] and references therein. Extrapolating $g_{KN\Lambda}(Q^2)$ to the kaon mass shell $Q^2 = -M^2_K$ yields values in the range $16.3 \leq g_{KN\Lambda} \leq 19.3$. This is slightly above the ballpark of the numbers extracted from experiment [TRdS95].

[8] These results are included here for completeness. For a detailed discussion of the theoretical background the reader is referred to [Fis99].

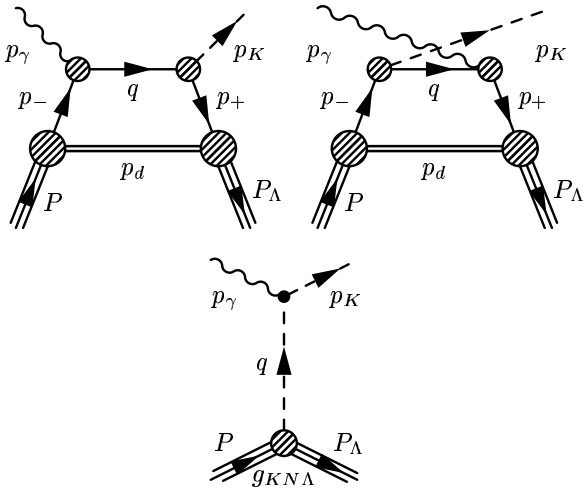

Figure 7.8: Main contributions to kaon photoproduction $p\gamma \to \Lambda K$. The incoming proton and the outgoing Λ carry the momenta P and P_Λ respectively. The lower part of the figure shows the tree level diagram that models the exchange of a virtual kaon.

Having introduced the basic formalism and having fixed the parameters of the model it is now possible to discuss the results for kaon photoproduction $\gamma p \to K\Lambda$. The main contributions to this reaction are shown in fig. 7.8 where the internal momenta of the (uncrossed) 'handbag diagram' are defined according to

$$p_- = p + \eta_p P \qquad p_d = -p + (1-\eta_p)P \tag{7.33}$$

$$q = p_- + p_\gamma \qquad p_+ = q - p_K \tag{7.34}$$

$$P_\Lambda = P + p_\gamma - p_K \qquad p_f = p + (1-\eta_p)P - (1-\eta_\Lambda)P_\Lambda\,. \tag{7.35}$$

Here η_p and η_Λ are the momentum partition parameters of the proton and the Λ, respectively. Both, η_p and η_Λ can be chosen independently in the range $0 \le \eta_p, \eta_\Lambda \le 1$.

The two 'handbag diagrams' model the coupling to one of the constituents. They are calculated within the Mandelstam formalism [Man55] which yields

$$A_1 = i\int \frac{d^4p}{(2\pi)^4}\left\{\bar{\Phi}_\Lambda(p_f, P_\Lambda)S(p_+)\Gamma_K(q,p_+)S(q)\right\}\{\Gamma_\gamma(p_-,q)S(p_-)\Phi_P(p,P)D(p_d)\} \tag{7.36}$$

for the amplitude of the uncrossed handbag diagram. Here $\bar{\Phi}_\Lambda$ and Φ_p are respectively the vertex–functions of the Λ and the proton as discussed in section 7.1. Furthermore Γ_K is the meson–quark vertex that has been discussed in the preceding section. The photon–quark coupling, Γ_γ is described by the Ball–Chiu vertex (2.32) or its generalisation to the case of non–analytic propagators, see section 7.1 and especially the discussion in [AAF$^+$00a]. The transverse contribution is usually found to be very small (for bound state reactions) and therefore it will be neglected in the following. Although the form of this vertex is not model

specific, it contains the self–energy functions and thus it implicitly depends on the model propagators. The expression for the crossed handbag diagram can be easily inferred from (7.36); this and all other technical details that enter this calculation are given in appendix B.3.

The tree level diagram models the exchange of a virtual kaon and is expected to yield a non–negligible contribution for large photon energies. For the photon–meson coupling we use a bare vertex multiplied with the kaon electromagnetic form factor (see Appendix B.3) while the meson–baryon vertex is proportional to $g_{KN\Lambda}(Q^2)$ that has been discussed in section 7.1.

The 'handbag diagrams' shown in figure 7.8 probe the propagators not only for space-like momenta but also for comparably large time-like momenta, as has been emphasised in section 7.3. This sensitivity to the behaviour of the propagators for time-like momenta distinguishes the reaction $p\gamma \to \Lambda K$ from most other production processes.

In the left panel of fig. 7.9 the total cross section $\sigma(\gamma p \to K\Lambda)$ is shown as a function of the photon energy E . One observes that the parameter sets (II–IV) predict cross sections that are comparable with the experimental data. These model calculations do not include axialvector diquarks. Once these degrees of freedom are taken into account (sets V and VI), the cross–section is overestimated by about a factor four. For the five sets II–VI one finds that the total cross section is strongly dominated by the kaon–exchange diagram (cf. fig. 7.8) while the handbag–type diagrams could be almost neglected[9] and it is obvious that in this case the results for $g_{KN\Lambda}$ (cf. fig. 7.7) directly translate into results for the cross section. If only a single diagram contributes interference cannot occur and it is evident that the model calculations do not reproduce the dip in the energy region $1.1\text{GeV} \leq E \leq 1.4\text{GeV}$. Tuning the model propagators such that the two diagrams are of equal importance this dip could be reproduced [AAF$^+$00b]. One finds that an exponential dressing function (set I) leads to an extreme overestimation of the experimental data. In this case actually the handbag diagrams dominate while the kaon exchange contributions are comparatively small. Figure 7.9 clearly shows that the large disagreement of the model results with the data certainly is not a fine–tuning problem. Rather one has to conclude that the comparison with the data rules out propagators that strongly rise in the time-like region as the one dressed by an exponential function.

The differential cross section is shown in the right panel of fig. 7.9 for the energy interval $1.2\text{GeV} \leq E \leq 1.3\text{GeV}$ as a function of the angle between the momenta of the initial proton and the final kaon in the center of mass frame (see appendix B.3 for details). Although the model calculations reproduce the empirical increase of the differential cross section as $\cos\theta_{cm}$ goes from minus to plus one, the increase appears to be overestimated. For those parameter sets (II–VI) for which the resulting cross sections are dominated by the kaon exchange diagrams the predicted differential cross sections turn out too small in the backward scattering region while they are too big in the opposite direction. As a result the total cross section agrees with the empirical data reasonably well. Again, the exponential type propagators yield differential cross sections that are way off the data and this again

[9] It is interesting to note that even for the handbag diagram alone results obtained with a Ball-Chiu or bare photon quark vertex, respectively, differ by at most a few percent.

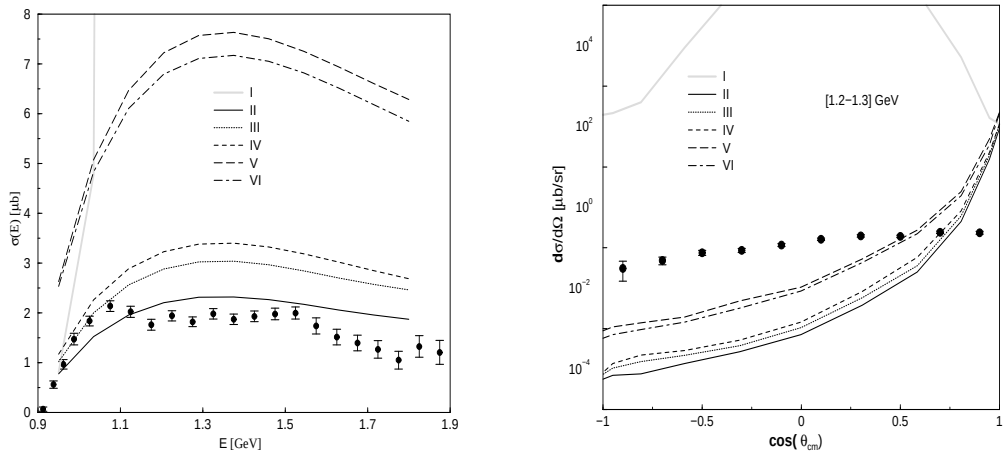

Figure 7.9: The total cross section for kaon photoproduction as a function of the incident photon momentum E (*left panel*) and the differential cross section (*right panel*) for kaon photoproduction averaged in the energy bin $[1.2, 1.3]$GeV. The parameter sets (I-VI) are defined in table 7.1. The experimental data are taken from [T^+98].

necessitates the conclusion that this type of dressing function is not acceptable.

The asymmetries that are defined in (B.44)–(B.46) have also been calculated. One finds that they essentially vanish for the model propagators that can be considered to be reasonable, i.e. sets II–VI. Although the model calculation correctly predicts that the polarised photon asymmetry Σ, see (B.46), is positive for $\cos\theta_{\mathrm{cm}} < 0$ and negative otherwise, the absolute values are off by several orders of magnitude. Only when substituting propagators that are characterized by the exponential dressing function the predicted asymmetries roughly agree with the empirical data. However, this type of propagator has already been discarded for reasons that have been detailed above.

Chapter 8

Conclusions and Outlook

The quark propagator has been the main objective of the present study. Three different approaches have been followed which mutually complement each other.

First the fermion propagator in (2+1)-dimensional QED has been investigated within the Dyson–Schwinger approach in order to allow for a direct comparison with the corresponding calculations for QCD. Hereby two different truncation schemes have been studied which allows to assess the reliability of the results. It has been found that the bare–vertex approximation as well as the Ball–Chiu ansatz for the vertex give very similar results which indicates that the results are general and not specific to the truncation scheme. Within this framework the phase structure of this model theory has been examined and in particular it has been shown that there is a phase where the chiral symmetry is spontaneously broken and where the fermions are confined. These results have been the motivation for the study of QED_3 : while being technically much simpler than QCD both theories share the same basic phenomena.

The results for the fermion propagator are encoded in the corresponding results for the self–energies A, B and it has been shown that the results for A are qualitatively different in the confined phase and in the unconfined phase. For the unconfined phase one finds that A has a power-like behaviour in the infrared which entails that $A(0) = 0$. This is in explicit contrast to the behaviour of A in the confined phase: there it is found that A becomes constant in the infrared at a non–vanishing $A(0) > 0$. This convincingly demonstrates that the fermion propagator (in QED_3) possesses the information whether or not the corresponding particle is confined. The scalar self–energy B and especially its infrared behaviour indicate whether the chiral symmetry is spontaneously broken. For the unconfined phase one finds that $B = 0$ whereas for the confined phase one finds that B is strongly enhanced for small momenta which demonstrates that the confinement phase transition is also a chiral phase transition.

The main part of the present study focuses on the quark propagator in Landau gauge QCD and on the quark–loop contribution to the gluon DSE. In an *ab initio* calculation the full coupled system of DSEs for the gluon-, ghost- and quark propagator has been solved. In order to arrive at a closed system of equations the approximate Slavnov–Taylor identities have been used to construct the vertex functions.

The solutions that have been found for the quenched approximation and for the full coupled system of DSEs are qualitatively very similar. For both cases the solutions show that chiral symmetry is spontaneously broken. This is expressed by the pion decay constant and the chiral condensate which are both nonzero. However, the strength of chiral symmetry breaking turns out to small. For $N_f = 0$ and $N_f = 6$ one obtains for the pion decay constant about 60% and 30%, respectively, of the experimentally measured value. This decrease of f_π is mainly due to the the decrease of the infrared scale σ which is then inherited by the pion decay constant, the chiral condensate and the mass function which all decrease as the number of flavours increases. The scalar self–energy B and the mass function M become both constant in the infrared quite similar to the results that have been found in QED_3.

A possible confinement signature should be apparent in A since the scalar self–energy B is essentially fixed by the pattern of chiral symmetry breaking. The results show that A becomes constant in the infrared which is in qualitative agreement with the infrared limit of A in the confined phase of QED_3. Furthermore it has been found that A has a bump at intermediate momenta that increases in size as the number of flavours is increased. This bump therefore is an interference effect due to the quark–loop which occurs only in the full coupled system.

Also the results for the gluon- and ghost renormalization functions Z and G are qualitatively very similar to the corresponding results for the quenched approximation. Since the quark–loop is subleading in the infrared (as compared to the ghost–loop) one finds for all $0 \leq N_f \leq 6$ that the gluon propagator is infrared vanishing ($Z \propto x^{1.84}$) while the ghost propagator is infrared enhanced ($G \propto x^{-0.92}$). The renormalization functions have been rewritten using the functions F and R which have a more direct physical interpretation in terms of the running coupling ($\propto F$) and the effective interaction (FR) in the quark Dyson–Schwinger equation. It has been shown that the qualitative features of F and R remain unchanged upon the inclusion of the quark–loop. However, the infrared limit $F(0)$ as well as the UV limit of R decrease as the number of flavours is increased. This N_f–dependence of R is inherited by the effective coupling FR and thus leads to the pronounced N_f–dependence of the strength of chiral symmetry breaking. The non–perturbative running coupling α_s is proportional to F in a way that the N_f–dependence of $F(0)$ cancels. This implies that α_s has an infrared fixed point at $\alpha_s \approx 9.48$ independent of the number of flavours.

One of the main issues of the present study is the investigation of the physical positivity constraints for the gluon- and quark propagators. A violation of these positivity constraints implies that no Källen–Lehmann representation exists and that the corresponding particle therefore cannot occur in the asymptotic spectrum. For the gluon propagator it has been found that positivity is violated for all $0 \leq N_f \leq 6$. This very strongly indicates that all coloured gluon states are confined. This is in contrast to the results for the quark propagator where no violation of the physical positivity constraints could be found. However, while the violation of positivity implies that the corresponding particle is confined one cannot conclude that the non–violation of positivity indicates unconfined particles.

Finally it has been investigated whether meson production processes can give phenomenological constraints on the quark propagator. It has been shown that these production processes involve a large time–like momentum transfer to one of the constituents of the bound states that participate in the reaction. Among these meson production processes kaon photoproduction has been found to be particularly well suited to constrain the quark propagator in the time–like region. This complements the Dyson–Schwinger studies which are set up in Euclidean space an thus yield the propagators only for space–like momenta.

The differential and total cross section as well as the asymmetries for kaon photoproduction have been calculated within the covariant diquark–quark model. Hereby the propagators of the quark and diquark have been dressed in a way that effectively implements confinement. In order to study the importance of the qualitative features of the quark propagator different dressing functions have been examined and compared. The results for the cross section of kaon photoproduction clearly show that the quark propagator must not rise in the time–like region and in particular propagators with an exponential dressing function have been ruled out. Among the dressing functions that have been considered the results favour the Stingl ansatz [Sti96] which has no singularities for real momenta but complex conjugate poles. This is also supported by Dyson–Schwinger studies for QED_3 [Mar95].

The comparison of the Dyson–Schwinger results for QED_3 in the confined phase and QCD reveals important similarities. For the confined phase of QED_3 it has been found that the fermion propagator becomes constant in the infrared while it vanishes with a power-like behaviour in the unconfined phase. The study within this model theory thus suggests that a fermion propagator which becomes constant in the infrared indicates fermion confinement. Transferred to QCD this would then imply that the quark propagator that has been found corresponds to a confined quark.

This possible scenario would be surprising because the results for the gluon propagator gave credibility to the hypothesis that confinement is apparent in the propagators via violation of the positivity constraints. Furthermore the non–positivity of coloured states would directly combine with the BRS quartet mechanism to explain the absence of coloured states in the physical spectrum.

However, neither for QCD nor for QED_3 any indication of positivity violation could be found for the fermion propagator. As far as QED_3 is concerned it seems to be very unlikely that this result does depend on the truncation scheme since two rather different truncation schemes have been investigated. For QCD the situation is similar though somewhat less conclusive. The difficulties that have been encountered in the renormalization of the quark

DSE and of the quark loop indicate that the quark–gluon vertex as constructed from the approximate Slavnov–Taylor identity ignores an important ingredient. This should be due to the neglection of the quark–ghost scattering kernel in the corresponding Slavnov–Taylor identity.

The discussion also highlights the central issues that have to be more thoroughly understood in order to advance the present investigation. First it has to be examined whether the violation of positivity for the quark propagator actually *is* a necessary confinement signature. Here the comparison with QED_3 clearly indicates that this is not the case. Secondly in the construction of the quark–gluon vertex the quark–ghost scattering kernel should be taken into account. This is essential because otherwise the renormalization of the quark is impossible without further prescriptions.

Appendix A

Dyson-Schwinger Equations: Numerical Methods

This appendix collects various technical aspects of the numerical solution of the DSEs in QED_3 and QCD. The focus is on the numerical methods that have been found useful as well as on the (technical) problems that occur. Most of the techniques that have been applied to solve the DSEs for QED_3 (and that are described in the following section) can be applied to the coupled system of DSEs for QCD. - However, for the case of QCD there are some additional (technical) problems which are shortly discussed in a separate section. The Chebyshev approximation has been extensively used and it is discussed in section A.2

A.1 Dyson-Schwinger Equations for QED_3

Analytically the system of DSEs for the fermion propagator and the photon propagator is first transformed into a coupled system of equations for the selfenergy functions A, B and the polarization scalar Π (see eqs. (2.47)-(2.49)). As has been said already, this is a coupled system of *nonlinear* integral equations. Therefore it has to be solved using an iterative process. If we write the system of DSEs (2.47)-(2.49) formally as

$$A(p) = 1 + \Sigma_A[A, B, \Pi, p] \tag{A.1}$$

$$B(p) = \Sigma_B[A, B, \Pi, p] \tag{A.2}$$

$$\Pi(p) = N\,\Sigma_\Pi[A, B, p] \tag{A.3}$$

where N is the number of fermion flavours and Σ_A, Σ_B and Σ_Π contain the nontrivial contributions to A, B and Π respectively. These selfenergy contributions Σ_A, Σ_B and Σ_Π do depend nonlinearly on A, B and Π. The iterative process gives a sequence of approximations

$$A_{i+1}(p) = 1 + \Sigma_A[A_i, B_i, \Pi_i, p] \tag{A.4}$$

$$B_{i+1}(p) = \Sigma_B[A_i, B_i, \Pi_i, p] \tag{A.5}$$

$$\Pi_{i+1}(p) = N\,\Sigma_\Pi[A_i, B_i, p] \tag{A.6}$$

to the exact solution $\{\bar{A}, \bar{B}, \bar{\Pi}\}$ of (A.1), (A.2) and (A.3) such that

$$A_i \to \bar{A} \qquad B_i \to \bar{B} \qquad \Pi_i \to \bar{\Pi} \tag{A.7}$$

for $i \to \infty$ given that that starting guess $\{A_0, B_0, \Pi_0\}$ is in a sense not to 'far' from the real solution $\{\bar{A}, \bar{B}, \bar{\Pi}\}$.

The selfenergies Σ_A, Σ_B and Σ_Π are expressed as loop integrals over the Euclidean 4-momentum. One of angular integrations can be performed trivially such that the radial integral over k^2 and an angular integral over the angle between the external momentum p and the loop momentum k remains to be done numerically.

To illustrate the concepts it is appropriate to shortly recall the DSE for the polarization scalar in the bare vertex approximation; the techniques and methods are general and have been also applied to the DSEs for A and B. In the the asymmetric momentum routing the DSE for Π reads:

$$\Pi(p) = 4N\frac{e^2}{p^2}\int \frac{d^3k}{(2\pi)^3}\left(\frac{3}{p^2}\langle p, p-k\rangle\langle p, k\rangle - \langle p-k, k\rangle\right)\sigma_v(p-k)\sigma_v(k) \tag{A.8}$$

with

$$\sigma_v(k) = \frac{A(k)}{k^2A(k) + B(k)} \tag{A.9}$$

and the convention that $\langle p, k\rangle = pk\cos(\theta) = pkz$ denotes the scalar product of the Euclidean four momenta p and k. Eq. (A.8) is equal to

$$\Pi(p) = 2N\frac{e^2}{p^2}\frac{1}{(2\pi)^2}\int_0^{\Lambda^2} dk^2\, k\sigma_v(k)I(p^2, k^2) \tag{A.10}$$

$$I(p^2, k^2) = \int_{-1}^{+1} dz\left(k^2(1-3z^2) + 2pkz\right)\sigma_v(p^2 + k^2 - 2pkz) \tag{A.11}$$

where the angular dependence has been made explicit and the trivial angular integration has been performed. The radial momentum integral in (A.10) can be solved using different numerical methods but it has been found that it usually suffices to use

$$\begin{aligned}\int_{x_1}^{x_N} dx\ f(x) = h\Bigg(&\frac{3}{8}f(x_1) + \frac{7}{6}f(x_2) + \frac{23}{24}f(x_3)\\ &+ f(x_4) + f(x_5) + \cdots + f(x_{N-4}) + f(x_{N-3})\\ &+ \frac{23}{24}f(x_{N-2}) + \frac{7}{6}f(x_{N-1}) + \frac{3}{8}f(x_N)\Bigg)\end{aligned} \tag{A.12}$$

which can be found in [PTVF92]. However, some of the angular integrals in the DSEs for A and B have integrable singularities of $\log$-type at $p^2 = k^2$. To handle this the radial momentum integration over k^2 has been split into two parts

$$\int_{\Lambda_{IR}}^{\Lambda_{UV}} dk^2 \to \int_{\Lambda_{IR}}^{p^2} dk^2 + \int_{p^2}^{\Lambda_{UV}} dk^2 \tag{A.13}$$

and a Gauss-Legendre quadrature has been used to avoid the endpoints of the two separate integrals. Whether the extended Simpson formula (A.12) or the Gauss-Legendre integration has been used; in both cases the mesh points have been distributed exponentially. I.e. if the mesh points $\{x_0, \ldots, x_N\}$ are uniformly distributed then the transformation

$$x_i \to y_i = x_0 \exp\left(\frac{i}{N} \log(\frac{x_N}{x_0})\right) \qquad i = 0, 1, \ldots, N \tag{A.14}$$

will leave the endpoints unchanged but will lead to a over-proportional density of mesh-points in the vicinity of x_1 and comparably little mesh-points for large values which are comparable to x_N. The radial momentum integration in (A.10) has been done with about 300 mesh-points on the average but up to 1000 to test the numerical accuracy of the results.

For the angular integration over z in (A.11) a Gauss-Legendre routine has been used with 30 mesh-points in the average but up to 150 mesh-points for few calculations to test the numerical accuracy.

It turns out that it is not completely straightforward to evaluate the integral (A.11) numerically. The difficulties that appear shown up as an extremely large (and numerically unstable) value of $\Pi(p)$ for small p^2. The difficulties can be traced back to the interpolation that is used to evaluate the selfenergy functions A and B (which define σ_ν). Related problems have been investigated in [BP95a].

These difficulties can be understood in a 'heuristic' way; for large k^2 and small p^2 the function $\sigma_\nu(p^2 + k^2 - 2pkz)$ will be very close to $1/k^2$ which implies that $I(p^2, k^2)$ will be very close to

$$I(p^2, k^2) = \int_{-1}^{+1} dz\, (k^2(1 - 3z^2) + 2pkz) \frac{1}{k^2} \tag{A.15}$$

The integral over $(1 - 3z^2)$ vanishes in this limit as well as the integral over z. However, the cancellation that is necessary to guaranty the integral over $(1 - 3z^2)$ is zero if done numerically turns out to be rather demanding. If the functions A and B are not interpolated *very accurately* and *very smoothly* the cancellation wont work if the integral is done numerically. This implies that inaccurate angle integrations will lead to spurious quadratic UV divergencies in the polarisations scalar.

The most simple interpolation is probably the linear interpolation

$$f(x) = f(x_i) + f'(x_i)(x - x_i) \tag{A.16}$$

where $x_i, i = 1, 2, \ldots, N$ are the mesh-points where the function f is actually known. For the derivative f' one could e.g. use a three point formula. Using this simple interpolation to evaluate A and B and thus σ_ν at $(p^2 + k^2 - 2pkz)$ it seems to be impossible to find a numerically stable value of $\Pi(p)$ for small p^2.

So one should use more sophisticate methods for the interpolation. The next method that might be considered appropriate are polynomial

$$f(x) = P_n(x) \tag{A.17}$$

or rational approximations

$$f(x) = \frac{P_n(x)}{P_m(x)} \tag{A.18}$$

where P_n and P_m are polynomials which are to be matched to the function f. There are routines in [PTVF92] for polynomial and rational interpolation, however, these are to slow to be applied to an array of say 200 or more function values. To speed things up one could use the polynomial or the rational interpolation on a small sub-array of function values. Lets assume that we have to evaluate the function f at x and lets furthermore assume that

$$x_m < x_{m+1} < \ldots < x < \ldots < x_n \tag{A.19}$$

such that there are about 20 mesh values of f in total with about half of them smaller and half of them greater than x. Now one uses this sub-array of values as input for interpolation. Using this piece-wise interpolation (whether it be polynomial or rational) one finds that the polarization scalar in the infrared is much more stable than with the linear interpolation, however, there are still some smaller numerical uncertainties. These can be traced back to the fact that one has used a piece-wise interpolation which leads to an interpolated function which will still have some non-smooth remnants of the borders that mark the intervals (A.19) that have been used for the interpolation.

To have an accurate interpolation which is also fast enough one is lead to the Chebyshev approximation, which is discussed in section A.2. To increase the accuracy not the functions A, B and Π themselves have been approximated but their logarithm. Furthermore, to increase the accuracy, the interpolation has been carried out using the interval $[\log(p_{min}), \log(p_{max})]$ instead of $[p_{min}, p_{max}]$ (where p_{min} and p_{max} are the IR and the UV cutoff of the radial momentum integral). Using this method has several advantages; first and foremost the fact that this yields a numerically stable and accurate polarization scalar for all momenta and especially in the infrared. But there is even more to it; the fermion Dyson-Schwinger equations, i.e. the equations for A and B contain terms proportional to

$$\frac{A(k) - A(p)}{k^2 - p^2} \tag{A.20}$$

where k^2 is the loop momentum and p^2 is the external momentum. In the limit that $k^2 \to p^2$ this becomes a derivative which would have to be approximated if one would use a linear or a polynomial/rational interpolation. This is not the case for the Chebyshev interpolation because there is an exact formula (A.29) to calculate the derivative of a Chebyshev approximated function.

A.2 Chebyshev Approximation

In this section the Chebyshev approximation method [PTVF92], [AS72] is recalled. The method is used in the computations to approximate the selfenergy functions A, B and the polarization scalar Π. This is necessary since no angular approximation have been employed

which implies that the angular integrals have to be done numerically. This, of course, implies that A, B and Π have to be evaluated at momenta which are different from the external momentum mesh.

The Chebyshev polynomials T_i are orthogonal in the interval $[-1, 1]$

$$\int_{-1}^{+1} dx \, \frac{T_i(x)T_k(x)}{\sqrt{1-x^2}} = \begin{cases} 0 & i \neq k \\ \pi/2 & i = k \neq 0 \\ \pi & i = k = 0 \end{cases} \tag{A.21}$$

and are also bounded within $[-1, 1]$. The Chebyshev polynomial T_n is of degree n and has n zeros in the interval $[-1, 1]$. There is a very compact representation of the T_n:

$$T_n(x) = \cos\big(n \arccos(x)\big) \tag{A.22}$$

which immediately gives a formula for the zeros of T_n which are located at

$$x_k = \cos\left(\frac{\pi(k-1/2)}{n}\right) \qquad k = 1, 2, \ldots, n \tag{A.23}$$

as well as for the extrema, which are located at

$$\bar{x}_k = \cos\left(\frac{\pi k}{n}\right) \qquad k = 1, 2, \ldots, n \tag{A.24}$$

The Chebyshev polynomials satisfy also a discrete orthogonality relation

$$\sum_{k=1}^{m} T_i(x_k)T_j(x_k) = \begin{cases} 0 & i \neq k \\ m/2 & i = k \neq 0 \\ m & i = k = 0 \end{cases} \tag{A.25}$$

in addition to (A.21) where $i, j < m$ and $x_k, k = 1, 2, \ldots, m$ are the m zeros of T_m.

One would like to have an approximation of an function f of the form

$$f(x) = \sum_{i=0}^{N-1} b_i T_i(x) = \sum_{i=0}^{N-1} c_i T_i(x) - \frac{c_0}{2} \tag{A.26}$$

such that the approximation is *exact* at the n zeros x_k of T_n, i.e.

$$f(x_k) = \sum_{i=0}^{N-1} b_i T_i(x_k) \tag{A.27}$$

Now one multiplies both sides with $T_j(x_k)$ and sum over the zeros. Using (A.25) one obtains

$$\frac{n}{2} c_i = \sum_{k=0}^{N} T_i(x_k) f(x_k) \tag{A.28}$$

which gives us the coefficient c_i in terms of the values of f at the zeros x_k of T_n.

Having obtained the approximation (A.26) to the function f it is now simple to find corresponding approximations for the derivative and for the integral of f, since the only the derivatives and the integral of the Chebyshev polynomials has to be known. The derivative itself as well as the indefinite integral of f will have a certain approximation of the form (A.26) with coefficients c'_i for the derivative and with coefficients C_i for the indefinite integral of f. A simple computation gives:

$$c'_{i-1} = c'_{i+1} + 2(i-1)c_i \qquad i = m-1, m-2, \ldots, 2 \tag{A.29}$$

$$C_i = \frac{c_{i-1} - c_{i+1}}{2(i-1)} \qquad i > 1 \tag{A.30}$$

where the recurrence for the coefficients c'_i has to be started with the values $c'_m = c'_{m+1} = 0$ and the formula for C_i has to be supplemented by a corresponding value of C_1.

For every sufficiently smooth function the approximation (A.26) would converge to f for $n \to \infty$. But in practice we will of course truncate the approximation at a finite n. Since the Chebyshev polynomials are bounded to the interval $[-1,+1]$ the error cannot be larger than the sum over the coefficients c_k that have been neglected. Given that f is a smooth function, the coefficients c_k will decrease very rapidly with increasing k such that the total error is essentially equal to

$$c_{n+1} T_n(x) \tag{A.31}$$

This is an oscillatory function with $n+1$ equal extrema in the range $[-1,+1]$. I.e. the total error that is made in truncating the series in (A.26) is distributed smoothly over the interval $[-1,+1]$. This heuristic explanation illustrates the fact that the Chebyshev approximation (A.26) is very close to a approximating minimal polynomial for the function f. (A minimax polynomial has the smallest maximum deviation from f among all polynomials of the same degree.)

A.3 Dyson-Schwinger Equations for QCD

The numerical methods that have been described in section A.1 can be equally applied to the DSEs of Landau gauge QCD. However, it turned out the different measure necessitates the use of different methods for the angular integrations; this is shortly explained in the present section.

Considering only the that part of the polarization that reduces to the bare vertex; in the perturbative limit on has:

$$\Pi(p^2) = \frac{2}{3\pi p^2} \int dk^2 \, \sigma_v(k^2) I(p,k) \tag{A.32}$$

with

$$I(p,k) = \int_{-1}^{+1} dz \, \sqrt{1-z^2} \big(A(k^2) + A(q^2)\big) \sigma_v(q^2) \big(k^2 + 3kpz - 4k^2 z^2\big) \tag{A.33}$$

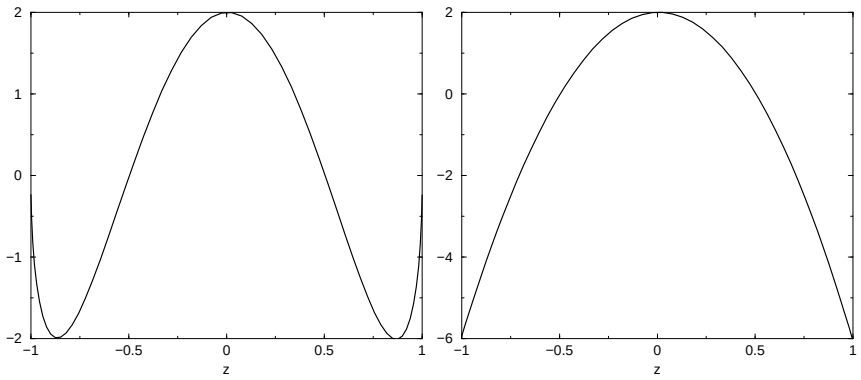

Figure A.1: Comparison of the 'effective' Integrand for the angular integral (A.33), as seen from the Gauss-Legendre method (left panel) and from the Gauss-Jacobi method (right panel).

where $q = p - k$. The difficult thing is to (numerically) avoid the potential divergence of the part

$$\int_{-1}^{+1} dz \sqrt{1-z^2} k^2 \left(1 - 4z^2\right) \tag{A.34}$$

which appears approximately in the limit that the momenta k^2 and p^2 are very different in size. For these very asymmetric momentum configurations the angular integral (A.33) reduces to approximately to (A.34) because $\sigma_v(q^2)$ is essentially $1/k^2$ and thus independent of the angle z in this limit. The integral (A.34) is analytically zero, however, if the numerical integration is not accurate enough, than one will find a spurious quadratic UV divergence (much like for QED_3). In table A.1 we compare the accuracy of the Gauss-Legendre method and the Gauss-Jacobi method for the angular integral (A.33) for different momenta p^2, k^2 and using $A = 1, B = 0.01 + exp(-x)$ to calculate $A(p^2)$ and $\sigma_v(p^2)$.

The superior accuracy of the Gauss-Jacobi method is clearly illustrated in table A.1. It's not to difficult to understand, why the Gauss-Jacobi integration method is so much more accurate for the angular integral (A.33). All Gaussian Quadrature methods split the integral up into two parts, the weight w and the function f

$$\int_a^b dx\, w(z) f(z) \approx \sum_{i=1}^{N} w_i f(z_i) \tag{A.35}$$

where w_i are the weights and x_i are the mesh points. The weight of the Gauss-Legendre method is just 1 whereas the weight of the Gauss-Jacobi method is

$$(1-z)^\alpha (1+z)^\beta \tag{A.36}$$

which is equal to $\sqrt{1-z^2}$ for $\alpha = \beta = 1/2$. I.e. for this specific choice of α and β the weight of the Gauss-Jacobi method is just equal to the $\sqrt{(1-z^2)}$ factor in (A.33) which

$p^2 = 0.1, k^2 = 0.1$	gauleg	gaujac
20	-1.660773143081649E-02	-1.654030995673128E-02
40	-1.654965140974475E-02	-1.654124830204696E-02
60	-1.654373296234553E-02	-1.654114720854071E-02
$p^2 = 0.1, k^2 = 10$	gauleg	gaujac
20	1.512119232602598E-02	1.570807865249677E-02
40	1.563268979223002E-02	1.570807865305222E-02
60	1.568550397194039E-02	1.570807865362877E-02
$p^2 = 0.1, k^2 = 1000$	gauleg	gaujac
20	-4.237893453849506E-04	1.570796347778181E-04
40	8.244329369611102E-05	1.570796353689294E-04
60	1.347291491104046E-04	1.570796359674817E-04

Table A.1: Comparison of the accuracy of the numerical angular integration for the angular integral (A.33) using Gauss-Legendre (gauleg) or Gauss-Jacobi (gaujac) integration. The integral (A.33) has been evaluated for different momenta p^2, k^2 and for different numbers of mesh points for the angular integration, N=20,40,60.

comes from the angular measure in 4 dimensions. That is the 'effective' integrand differs just by this measure factor, which is included in the weight of the Gauss-Jacobi integration method. The difference is illustrated in Fig. A.1 which shows the 'effective' integrand for the Gauss-Legendre and the Gauss-Jacobi method. As one can see: the integrand for the Gauss-Jacobi method is much simpler and thus potentially easier to integrate.

Appendix B

Technicalities

B.1 Symmetries of the Mass Terms in QED$_3$

In 2+1 dimensions parity corresponds to the inversion of one axis since the inversion of both axes could be undone by a rotation with angle π. For the following discussion it is therefore assumed that under parity P one has $(x, y) = \vec{x} \to \vec{x}_P = (-x, y)$.

The parity transformation of a two-component spinor ψ and on the gauge field A^μ is given by

$$P\psi(t,\vec{x})P^{-1} = \sigma_1\psi(t,\vec{x}_P) \tag{B.1}$$

$$PA^0(t,\vec{x})P^{-1} = A^0(t,\vec{x}_P) \tag{B.2}$$

$$PA^1(t,\vec{x})P^{-1} = -A^1(t,\vec{x}_P) \tag{B.3}$$

$$PA^2(t,\vec{x})P^{-1} = A^2(t,\vec{x}_P) \tag{B.4}$$

and time reversal T is given by

$$T\psi(t,\vec{x})T^{-1} = \sigma_2\psi(-t,\vec{x}) \tag{B.5}$$

$$TA^0(t,\vec{x})T^{-1} = A^0(-t,\vec{x}) \tag{B.6}$$

$$T\vec{A}(t,\vec{x})T^{-1} = -\vec{A}(-t,\vec{x}) \tag{B.7}$$

A mass term of the form $m\bar{\psi}\psi$ where ψ is a two-component spinor is thus odd under P and under T. Charge conjugation of the two-component spinor ψ and the gauge field amounts to

$$CA^\mu C^{-1} = -A^\mu \qquad C\psi C^{-1} = \sigma_1\psi^\dagger \tag{B.8}$$

I.e. the theory is invariant under CPT and under PT but not under P and T separately since these transformations would change the sign of the mass term $m\bar{\psi}\psi$ (ψ is a *two*-component spinor).

However, if one looks at the four-component spinor

$$\Psi = \begin{pmatrix}\psi_1\\ \psi_2\end{pmatrix} \tag{B.9}$$

the usual mass term $m\bar{\Psi}\Psi$ (which does now contain the four-component spinor Ψ) becomes

$$m\bar{\Psi}\Psi = m\left(\psi_1^\dagger\sigma_3\psi_1 - \psi_2^\dagger\sigma_3\psi_2\right) \tag{B.10}$$

The parity transformation does now give $\psi_1 \to \sigma_1\psi_2$ and $\psi_2 \to \sigma_1\psi_1$ which implies that (B.10) is invariant under parity transformations.

This is different for the mass term

$$m\bar{\Psi}\frac{1}{2}\left[\gamma^3,\gamma^5\right]\Psi = m\left(\psi_1^\dagger\sigma_3\psi_1 + \psi_2^\dagger\sigma_3\psi_2\right) \tag{B.11}$$

which is not parity invariant. In the two component formalism the mass term (B.11) would introduce a Chern-Simons mass term for the gauge field via the one-loop vacuum polarization [DJT82, AHW82, Red84]. It is not completely clear whether the mass term (B.11) and the corresponding Chern-Simons term could be generated spontaneously thus leading to spontaneous violation of parity in QED_3 . However, it seems that parity conserving vacuum configurations are the only ones that can be generated dynamically in vector theories since they are energetically preferred [VW84].

B.2 Angle Integrals

This section lists the angle integrals that have been found particularly useful in the investigation of Dyson-Schwinger equations in QCD and in QED_3 . See [GR94] and [AS72] for more on this.

For the angle integrals that appear in the Dyson-Schwinger equations for QCD the following general recursion formula has been used

$$\int_{-1}^{+1} dz\sqrt{1-z^2}z^{2n} = \frac{\sqrt{\pi}}{2}\frac{\Gamma(n+\frac{1}{2})}{\Gamma(n+2)} \tag{B.12}$$

$$\int_{-1}^{+1} dz\sqrt{1-z^2}\frac{z^n}{z-a} = \int_{-1}^{+1} dz\sqrt{1-z^2}z^{n-1} + a\int_{-1}^{+1} dz\sqrt{1-z^2}\frac{z^n-1}{z-a} \tag{B.13}$$

which comprises the following special cases:

$$\int_{-1}^{+1} dz\sqrt{1-z^2}\frac{1}{a-z} = \pi\left(a-\sqrt{(a^2-1)}\right) \tag{B.14}$$

$$\int_{-1}^{+1} dz\sqrt{1-z^2}\frac{z}{a-z} = \pi\left(a^2-\frac{1}{2}-a\sqrt{(a^2-1)}\right) \tag{B.15}$$

$$\int_{-1}^{+1} dz\sqrt{1-z^2}\frac{z^2}{a-z} = \pi a\left(a^2-\frac{1}{2}-a\sqrt{(a^2-1)}\right) \tag{B.16}$$

$$\int_{-1}^{+1} dz\sqrt{1-z^2}\frac{z^3}{a-z} = \pi a^2\left(a^2-\frac{1}{2}-a\sqrt{(a^2-1)}\right) - \frac{\pi}{8} \tag{B.17}$$

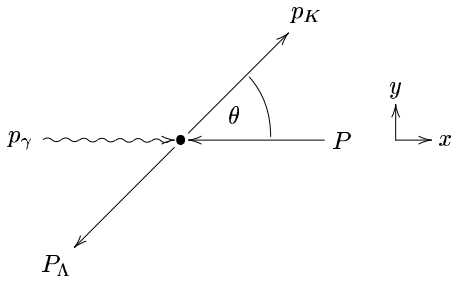

Figure B.1: Kinematics for kaon photoproduction $p\gamma \to \Lambda K$ in the center of momentum frame. The incoming proton and photon carry the momenta P and p_γ respectively. The outgoing kaon and Λ are labelled by the momenta p_K and P_Λ.

For QED_3 the following angle integrals have been used:

$$\int_{-1}^{+1} dz \frac{1}{\alpha - z} = \log\left(\frac{\alpha+1}{\alpha-1}\right) \tag{B.18}$$

$$\int_{-1}^{+1} dz \frac{z}{\alpha - z} = -2 + \alpha \log\left(\frac{\alpha+1}{\alpha-1}\right) \tag{B.19}$$

$$\int_{-1}^{+1} dz \frac{z^2}{\alpha - z} = \alpha\left[-2 + \alpha \log\left(\frac{\alpha+1}{\alpha-1}\right)\right] \tag{B.20}$$

$$\int_{-1}^{+1} dz \frac{1}{(\alpha - z)^2} = \frac{2}{\alpha^2 - 1} \tag{B.21}$$

$$\int_{-1}^{+1} dz \frac{z}{(\alpha - z)^2} = \frac{2\alpha}{\alpha^2 - 1} - \log\left(\frac{\alpha+1}{\alpha-1}\right) \tag{B.22}$$

$$\int_{-1}^{+1} dz \frac{z^2}{(\alpha - z)^2} = 2\frac{2\alpha^2 - 1}{\alpha^2 - 1} - 2\alpha \log\left(\frac{\alpha+1}{\alpha-1}\right) \tag{B.23}$$

$$\int_{-1}^{+1} dz \frac{z^3}{(\alpha - z)^2} = \frac{6\alpha^3 - 4\alpha}{\alpha^2 - 1} - 3\alpha^2 \log\left(\frac{\alpha+1}{\alpha-1}\right) \tag{B.24}$$

B.3 Kaon Photoproduction $p\gamma \to \Lambda K$

In this appendix the calculation of the diagrams shown in fig. 7.8 is detailed. They provide the main contributions to the reaction $p\gamma \to \Lambda K$.

The calculations have been performed in both: the rest frame of the proton and in the center of momentum system (CMS). For the following discussion we choose the CMS for

definiteness. The momenta are defined according to figure B.1, that is

$$P = (-E, 0, 0, iE_P) \tag{B.25}$$
$$p_\gamma = (E, 0, 0, iE) \tag{B.26}$$
$$p_K = (|\vec{p}_K| \cos\theta, |\vec{p}_K| \sin\theta, 0, iE_K) \tag{B.27}$$
$$P_\Lambda = (-|\vec{p}_K| \cos\theta - |\vec{p}_K| \sin\theta, 0, iE_\Lambda) \tag{B.28}$$

where the definitions:

$$E_P = \sqrt{M_P^2 + E^2} \tag{B.29}$$
$$E_K = \frac{1}{2(E + E_P)} \left((E + E_P)^2 - M_\Lambda^2 + M_K^2 \right) \tag{B.30}$$
$$|\vec{p}_K| = \sqrt{(E_K)^2 - M_K^2} \tag{B.31}$$
$$E_\Lambda = \sqrt{\vec{p}_K{}^2 + M_\Lambda^2} \tag{B.32}$$

have been used. The on–shell conditions and momentum conservation leave only two kinematical variables undetermined. These are usually chosen to be the energy E of the incoming photon and the angle θ between the spatial momenta of the photon and the outgoing kaon.

The three diagrams in figure 7.8 show the contributions to the transition amplitudes that we will discuss here. The uncrossed 'handbag diagram' translates into

$$A_1 = i \int \frac{d^4p}{(2\pi)^4} \left\{ \bar{\Phi}_\Lambda(p_f, P_\Lambda) S(p_+) \Gamma_K(q, p_+) S(q) \right\} \{ \Gamma_\gamma(p_-, q) S(p_-) \Phi(p, P) D(p_d) \} \tag{B.33}$$

with the momentum routing described in (7.33), see also figure 7.8. The notation is as set up in section 7.4: $\bar{\Phi}_\Lambda$ and Φ_p are the vertex–functions of the Λ and the proton respectively (see section 7.1). Furthermore Γ_K is the meson–quark vertex (7.19) that has been specified in section 7.1. The photon–quark coupling, Γ_γ is described by the Ball–Chiu vertex (2.32)

The crossed 'handbag diagram' corresponds to the expression

$$A_2 = i \int \frac{d^4p}{(2\pi)^4} \left\{ \bar{\Phi}_\Lambda(p_f, P_\Lambda,) S(p_+) \Gamma_\gamma(q, p_+) S(q) \right\} \{ \Gamma_K(p_-, q) S(p_-) \Phi(p, P) D(p_d) \} \, . \tag{B.34}$$

The definitions for q and p_+ have changed as compared to the momentum routing for the amplitude A_1 given in (7.33)-(7.35). For (B.34) we have instead:

$$q = p_- - p_K \quad \text{and} \quad p_+ = q + p_\gamma \, , \tag{B.35}$$

with all other momentum definitions unchanged.

The amplitude corresponding to the tree level diagram arising from kaon exchange is given by

$$A_3 = (\bar{u}_\Lambda [g_{KN\Lambda}\gamma_5] u_p)\, \frac{1}{q^2 + M_K^2}\, (\Gamma^\nu \epsilon_\nu) \ . \tag{B.36}$$

Here $g_{KN\Lambda}$ represents the strong form factor that has been discussed in section 7.1 and M_K is the kaon mass. The photon polarization is denoted by ϵ_ν while Γ^ν refers to kaon–photon vertex containing the electromagnetic form factor of the kaon

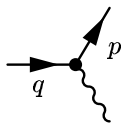

$$= \Gamma^\nu(q,p) = (q^\nu + p^\nu) F_{K^+}((p-q)^2) \ . \tag{B.37}$$

For the purpose of the present investigation it is sufficient to parameterise the kaon charge form factor with a monopole such that the phenomenological value of the kaon radius, $\langle r^2_{K^+}\rangle = (0.34 \pm 0.05)\mathrm{fm}^2$, is reproduced: $F_{K^+}(Q^2) = 1/(1 + Q^2/(0.84\mathrm{GeV})^2)$.

The Bethe–Salpeter formalism is set up in Euclidean space as has been discussed in section 7.3. The loop momentum p is chosen to be real, thus the temporal components of the external momenta in (B.25)–(B.28) have to be purely imaginary. Hence the relative momentum p_f as given in (7.35) is complex. Since the solution of the BSE provides the vertex function Φ_Λ only for real relative momenta p_f, one has to extrapolate Φ_Λ to complex momenta. This is done using rational functions that are fitted to the vertex functions (which are known at N real mesh-points). These rational functions can then easily be analytically continued. For real momenta a comparison of the fitted parameterisation to the known results allows us to estimate the reliability of this treatment.

The differential cross section depends only on the energy E of the incoming photon and the angle θ between the spatial photon and kaon momenta. That is illustrated in figure B.1. The differential cross section is defined with respect to the solid angle element $d\Omega_K = 2\pi d(\cos\theta)$ of the outgoing kaon:

$$\frac{d\sigma}{d\Omega_K}(E,\theta) = \frac{1}{4} \sum_{s_i, s_f} \frac{d\tilde{\sigma}}{d\Omega_K}(E,\theta) \tag{B.38}$$

with

$$\frac{d\tilde{\sigma}}{d\Omega_K}(E,\theta) = \frac{\alpha}{64\pi^2} 4 M_p M_\Lambda \, |A_1 + A_2 + A_3|^2 \ . \tag{B.39}$$

As indicated in (B.38) one has to average, respectively sum over the spins s_i, s_f of the initial and final states. The phase space factors denoted by α are given as

$$\alpha = \frac{1}{P \cdot p_\gamma} \frac{|\vec{p}_K|^2}{E_K E_\Lambda} \left| \frac{d\,|\vec{p}_K|}{d(E_K + E_\Lambda)} \right| \tag{B.40}$$

with

$$\left|\frac{d\,|\vec{p}_K|}{d(E_K+E_\Lambda)}\right| = \left(\frac{|\vec{p}_K|}{E_K} - \frac{\hat{p}_K\cdot\vec{P}_\Lambda}{E_\Lambda}\right)^{-1} . \tag{B.41}$$

Note that the right hand side of (B.41) remains positive given that $m_\Lambda > M_K$. In the CMS the expression (B.40) for α simplifies to

$$\alpha = \frac{|\vec{p}_K|}{|\vec{p}_\gamma|}\frac{1}{s}\,, \tag{B.42}$$

where $s = (P+p_\gamma)^2 = (p_K+P_\Lambda)^2$ denotes the total center of mass energy squared. In obtaining the phase space factors (B.40) the one particle normalisation conditions (for Minkowski space)

$$\langle p|p'\rangle_B = 2p^0(2\pi)^3\delta^3(\vec{p}-\vec{p'}) \quad \text{and} \quad \langle p|p'\rangle_F = \frac{p^0}{m}(2\pi)^3\delta^3(\vec{p}-\vec{p'})\,, \tag{B.43}$$

for bosons (B) and fermions (F) have been adopted. These conventions also enter the calculation of the transition amplitudes $A_i, i = 1,2,3$ and the normalisation of the Bethe–Salpeter wave–functions.

One obtains the various asymmetries by restricting the sum in eq (B.38) over the spins to two of the three non–scalar particles. These asymmetries are: the Λ*–polarization asymmetry*

$$P(E,\theta) = \frac{1}{4}\sum_{s_p,s_\gamma}\frac{[s_\Lambda=\uparrow]-[s_\Lambda=\downarrow]}{[s_\Lambda=\uparrow]+[s_\Lambda=\downarrow]} \tag{B.44}$$

the *polarized target asymmetry*

$$T(E,\theta) = \frac{1}{2}\sum_{s_\Lambda,s_\gamma}\frac{[s_p=\uparrow]-[s_p=\downarrow]}{[s_p=\uparrow]+[s_p=\downarrow]} \tag{B.45}$$

and the *polarized photon asymmetry*

$$\Sigma(E,\theta) = \frac{1}{2}\sum_{s_\Lambda,s_p}\frac{[s_\gamma=\uparrow]-[s_\gamma=\downarrow]}{[s_\gamma=\uparrow]+[s_\gamma=\downarrow]}\,, \tag{B.46}$$

where the shorthand notation

$$[s_\Lambda=\uparrow] = \left.\frac{d\tilde{\sigma}}{d\Omega_K}\right|_{s_\Lambda=\uparrow} \qquad \text{etc.}\,. \tag{B.47}$$

has been used and where the spins of the photon, the proton and the Λ have been denoted by s_γ, s_p and s_Λ, respectively.

The total cross section is finally obtained from (B.38) via

$$\sigma(E) = \int_0^\pi \sin\theta\; d\theta \frac{d\sigma}{d\Omega_K}(E,\theta)\,. \tag{B.48}$$

Bibliography

[AA99] S. Ahlig and R. Alkofer, *(In-)consistencies in the Relativistic Description of Excited States in the Bethe-Salpeter Equation*, Annals Phys. **275** (1999), 113–147.

[AACKK+96] I. J. R. Aitchison, G. Amelino-Camelia, M. Klein-Kreisler, N. E. Mavromatos, and D. McNeill, *Non-trivial infrared structure in (2+1)-dimensional quantum electrodynamics*, hep-th/9607192 (1996).

[AAF+00a] S. Ahlig, R. Alkofer, C. Fischer, M. Oettel, H. Reinhardt, and H. Weigel, *Production processes as a tool to study parameterizations of quark confinement*, Phys. Rev. **D64** (2000), 014004.

[AAF+00b] R. Alkofer, S. Ahlig, C. Fischer, M. Oettel, and H. Reinhardt, *Octet and decuplet baryons in a confining and covariant diquark quark model*, Nucl. Phys. **A663** (2000), 683–686.

[AB98a] D. Atkinson and J. C. R. Bloch, *QCD in the Infrared with Exact Angular Integrations*, Mod. Phys. Lett. **A13** (1998), 1055–1062.

[AB98b] D. Atkinson and J. C. R. Bloch, *Running Coupling in Nonperturbative QCD. 1. Bare Vertices and y-max Approximation*, Phys. Rev. **D58** (1998), 094036.

[ABKW86] T. W. Appelquist, M. Bowick, D. Karabali, and L. C. R. Wijewardhana, *Spontaneous chiral-symmetry breaking in three-dimensional QED*, Phys. Rev. **D33** (1986), 3704–3713.

[AHW82] I. Affleck, J. A. Harvey, and E. Witten, *Instantons and (Super)Symmetry Breaking in (2+1)- Dimensions*, Nucl. Phys. **B206** (1982), 413.

[AJ88] D. Atkinson and P. W. Johnson, *Chiral Symmetry Breaking in QCD. 2. Running Coupling Constant*, Phys. Rev. **D37** (1988), 2296–2299.

[AJ90] D. Atkinson and P. W. Johnson, *Current and Constituent Quark Masses. 1. Beyond Chiral Symmetry Breaking*, Phys. Rev. **D41** (1990), 1661.

[AMM97] I. J. R. Aitchison, N. E. Mavromatos, and D. McNeill, *Inverse Landau-Khalatnikov transformation and infrared critical exponents of (2+1)-dimensional quantum electrodynamics*, Phys. Lett. **B402** (1997), 154–158.

[AR95] R. Alkofer and H. Reinhardt, *Chiral Quark Dynamics*, Lecture notes in physics, Berlin, Germany: Springer, 1995.

[AS72] M. Abramowitz and I. A. Stegun (eds.), *Handbook of Mathematical Functions*, Dover Publications, New York, 1972.

[AvS00] R. Alkofer and L. v. Smekal, *The Infrared Behavior of QCD Green's Functions: Confinement Dynamical Symmetry Breaking, and Hadrons as Relativistic Bound States*, Phys. Rep. (2000).

[Bal90] R. D. Ball, *Baryons and Ladders*, Phys. Lett. **B245** (1990), 213–220.

[Bas00] A. Bashir, *Non-perturbative fermion propagator for the massless quenched QED3*, hep-th/0011022, 2000.

[BC80a] J. S. Ball and T. W. Chiu, *Analytic Properties of the Vertex Function in Gauge Theories. 1*, Phys. Rev. **D22** (1980), 2542.

[BC80b] J. S. Ball and T. W. Chiu, *Analytic Properties of the Vertex Function in Gauge Theories. 2*, Phys. Rev. **D22** (1980), 2550.

[BD89] N. Brown and N. Dorey, *Rutherford Appleton Laboratory Report No. RAL-89/115*, (unpublished), 1989.

[Blo95] J. C. R. Bloch, *Numerical Investigation of Fermion Mass Generation in QED*, Ph.D. thesis, University of Durham, 1995.

[Blo01] J. C. R. Bloch, *private communication*, 2001.

[BP95a] J. C. R. Bloch and M. R. Pennington, *Numerical Cancellation of Photon Quadratic Divergence in the Study of the Schwinger-Dyson Equations in Strong Coupling QED*, Mod. Phys. Lett. **A10** (1995), 1225–1233.

[BP95b] N. Brambilla and G. M. Prosperi (eds.), *Quark Confinement and the Hadron Spectrum*, World Scientific, 1995.

[BP97] N. Brambilla and G. M. Prosperi (eds.), *Quark Confinement and the Hadron Spectrum II*, World Scientific, 1997.

[BPR92] C. J. Burden, J. Praschifka, and C. D. Roberts, *Photon polarization tensor and gauge dependence in three-dimensional quantum electrodynamics*, Phys. Rev. **D46** (1992), 2695–2702.

[BR91] C. J. Burden and C. D. Roberts, *Light cone regular vertex in quenched QED in three dimensions*, Phys. Rev. **D44** (1991), 540–550.

[BRS75] C. Becchi, A. Rouet, and R. Stora, *Renormalization of the Abelian Higgs-Kibble Model*, Comm. Math. Phys. **42** (1975), 127–162.

[BRS76] C. Becchi, A. Rouet, and R. Stora, *Renormalization of Gauge Theories*, Annals Phys. **98** (1976), 287–321.

[BRS96] A. Bender, C. D. Roberts, and L. Von Smekal, *Goldstone Theorem and Diquark Confinement Beyond Rainbow-Ladder Approximation*, Phys. Lett. **B380** (1996), 7–12.

[BRS+99] J. C. R. Bloch, C. D. Roberts, S. M. Schmidt, A. Bender, and M. R. Frank, *Nucleon form factors and a nonpointlike diquark*, Phys. Rev. **C60** (1999), 062201.

[BRS00] J. C. R. Bloch, C. D. Roberts, and S. M. Schmidt, *Selected nucleon form factors and a composite scalar diquark*, Phys. Rev. **C61** (2000), 065207.

[BT98] C. J. Burden and P. C. Tjiang, *Deconstructing the vertex ansatz in three dimensional quantum electrodynamics*, Phys. Rev. **D58** (1998), 085019.

[C+98] C. Caso et al., *Review of Particle Physics*, Eur. Phys. J. **C3** (1998), 1.

[Cor80] J. M. Cornwall, *Confinement and chiral-symmetry breakdown: Estimates of F_π and of Effective Quark Masses*, Phys. Rev. **D22** (1980), 1452–1468.

[CP90] D. C. Curtis and M. R. Pennington, *Truncating the Schwinger-Dyson equations: How multiplicative renormalizability and the Ward identity restrict the three point vertex in QED*, Phys. Rev. **D42** (1990), 4165–4169.

[CPB89] R. T. Cahill, J. Praschifka, and C. Burden, *Diquarks and the Bosonization of QCD*, Austral. J. Phys. **42** (1989), 161–169.

[CPW92] D. C. Curtis, M. R. Pennington, and D. Walsh, *Dynamical mass generation in QED_3 and the $1/N$ expansion*, Phys. Lett. **B295** (1992), 313–319.

[CS98] A. Campbell-Smith, *Composite operator effective potential approach to QED(3)*, Mod. Phys. Lett. **A13** (1998), 2337–2346.

[CSM98] A. Campbell-Smith and N. E. Mavromatos, *Effective Gauge Theories, The Renormalization Group, And High T(C) Superconductivity*, Acta Phys. Polon. **B29** (1998), 3819–3870.

[Cut54] R. E. Cutkosky, *Solutions of a Bethe-Salpeter Equation*, Phys. Rev. **96** (1954), 1135.

[DG00] W. Dittrich and H. Gies, *Probing the quantum vacuum. Perturbative effective action approach in quantum electrodynamics and its application*, Springer Tracts Mod. Phys. **166** (2000), 1–241.

[DJT82] S. Deser, R. Jackiw, and S. Templeton, *Topologically massive gauge theories*, Ann. Phys. **140** (1982), 372–411.

[DMR94] Z. Dong, H. J. Munczek, and C. D. Roberts, *Gauge covariant fermion propagator in quenched, chirally symmetric quantum electrodynamics*, Phys. Lett. **B333** (1994), 536–544.

[Dys49] F. J. Dyson, *The S Matrix in Quantum Electrodynamics*, Phys. Rev **75** (1949), 1736.

[EI93] G. V Efimov and M. A. Ivanov, *The Quark confinement model of hadrons*, Bristol, UK: IOP, 1993.

[Fad65] L. D. Faddeev, *Mathematical Aspects of the Three Body Problem in Quantum Scattering Theory*, Davey, New York, 1965.

[FGML73] H. Fritzsch, M. Gell-Mann, and H. Leutwyler, *Advantages of the Color Octet Gluon Picture*, Phys. Lett. **B47** (1973), 365–368.

[Fis99] C. Fischer, *Assoziierte Strangeness-Produktion in einem kovarianten Diquark-Quark-Modell der Baryonen*, Diplomarbeit, Universtität Tübingen, 1999.

[FP67] L. D. Faddeev and V. N. Popov, *Feynman Diagrams for the Yang-Mills Field*, Phys. Lett. **B25** (1967), 29.

[Gie99] H. Gies, *Probing the Quantum Vacuum, Perturbative Effective Action Approach in QED and QCD and its Applications*, Ph.D. thesis, Universität Tübingen, 1999.

[Glö83] W. Glöckle, *The Quantum Mechanical Few-Body Problem*, Springer, Berlin, 1983.

[GM62] M. Gell-Mann, *Symmetries of Baryons and Mesons*, Phys. Rev. **125** (1962), 1067–1084.

[GMN64] M. Gell-Mann and Y. Ne'eman, *The Eightfold Way*, Frontiers in Physics, Benjamin, 1964.

[GMS98] V. P. Gusynin, V. A. Miransky, and A. V. Shapagin, *Effective action and conformal phase transition in QED(3)*, Phys. Rev. **D58** (1998), 085023.

[Gol61] J. Goldstone, *Field Theories with 'Superconductor' Solutions*, Nuovo Cim. **19** (1961), 154–164.

[GR94] I. S. Gradshteyn and I. M. Ryzhik, *Table of Integrals, Series and Products*, 5th ed., Academic Press, 1994.

[GW73] D. J. Gross and F. Wilczek, *Asymptotically Free Gauge Theories. I*, Phys. Rev. **D8** (1973), 3497.

[H$^+$76] G. Hohler et al., *Analysis of Electromagnetic Nucleon Form-Factors*, Nucl. Phys. **B114** (1976), 505.

[Haa96] R. Haag, *Local Quantum Physics*, Springer-Verlag, Berlin Heidelberg, 1996.

[HAOR97] G. Hellstern, R. Alkofer, M. Oettel, and H. Reinhardt, *Nucleon form factors in a covariant diquark-quark model*, Nucl. Phys. **A627** (1997), 679–709.

[Hel98] G. Hellstern, *Baryonen in einem kovarianten Diquark-Quark Modell mit Confinement*, Ph.D. thesis, Universität Tübingen, 1998.

[HKLW98] M. Hess, F. Karsch, E. Laermann, and I. Wetzorke, *Diquark masses from lattice QCD*, Phys. Rev. **D58** (1998), 111502.

[HM99] M. Hott and G. Metikas, *Effective action for QED in 2+1 dimensions at finite temperature*, Phys. Rev. **D60** (1999), 067703.

[HvSA98] A. Hauck, L. v. Smekal, and R. Alkofer, *Solving the gluon Dyson-Schwinger equation in the Mandelstam approximation*, Comput. Phys. Commun. **112** (1998), 149.

[Isg00] N. Isgur (ed.), *Quark Confinement and the Hadron Spectrum III*, World Scientific, 2000.

[Ish98] N. Ishii, *Meson exchange contributions to the nucleon mass in the Faddeev approach to the NJL model*, Phys. Lett. **B431** (1998), 1–7.

[J$^+$00] M. K. Jones et al., *G(E(p))/G(M(p)) ratio by polarization transfer in e(pol.) p - e p(pol.)*, Phys. Rev. Lett. **84** (2000), 1398–1402.

[JC99] M. T. Jeong and I. T. Cheon, *K N Lambda and K N Sigma coupling constants from the chiral bag model*, Eur. Phys. J. **A4** (1999), 357–362.

[Kar96] F. Karsch, *Thermodynamics of the Quark Gluon Plasma from Lattice Regularized QCD*, Lectures presented at the workshop 'Matter under Extreme Conditions', held on October 15th-17th, 1996 in Kloster Banz, 1996.

[Kau69] W. B. Kaufmann, *Numerical Solutions of the Bethe-Salpeter Equation*, Phys. Rev. **187** (1969), 2051.

[Kin83] J. E. King, *The Transverse Vertex and Gauge Technique in Quantum Electrodynamics*, Phys. Rev. **D27** (1983), 1821.

[KO79] T. Kugo and I. Ojima, *Local Covariant Operator Formalism of Non-Abelian Gauge Theories and Quark Confinement Problem*, Prog. Theor. Phys. Suppl. **66** (1979), 1.

[Kug95] T. Kugo, *The Universal Renormalization Factors Z(1)/Z(3) and Color Confinement Condition in Nonabelian Gauge Theory*, International Symposium on BRS Symmetry (on the occasion of its 20th anniversary, 1995, hep-th/9511033.

[Kug97] T. Kugo, *Eichtheorie*, Springer, 1997.

[Lan01] K. Langfeld, *SU(2) gluon propagators from the lattice: A preview*, hep-lat/0104003, 2001.

[LSW98] D. Leinweber, J. I. Skullerud, and A. G. Williams, *Gluon Propagator in the Infrared Region*, Phys. Rev. **D58** (1998), 031501.

[Man55] S. Mandelstam, *Dynamical variables in the Bethe-Salpeter formalism*, Proc. Roy. Soc. Lond. **A233** (1955), 248.

[Man76] S. Mandelstam, *Vortices and Quark Confinement in Nonabelian Gauge Theories*, Phys. Rept. **23** (1976), 245–249.

[Mar93] P. Maris, *Nonperturbative Analysis of the Fermion Propagator*, Ph.D. thesis, Rijksuniversiteit Groningen, 1993.

[Mar95] P. Maris, *Confinement and complex singularities in three-dimensional QED*, Phys. Rev. **D52** (1995), 6087–6097.

[Mar96] P. Maris, *The influence of the full vertex and vacuum polarization on the fermion propagator in QED3*, Phys. Rev. **D54** (1996), 4049–4058.

[MP78] W. Marciano and H. Pagels, *Quantum Chromodynamics: A Review*, Phys. Rept. **36** (1978), 137.

[MR97] P. Maris and C. D. Roberts, *pi and K meson Bethe-Salpeter amplitudes*, Phys. Rev. **C56** (1997), 3369–3383.

[Mut87] T. Muta, *Foundations of Quantum Chromodynamics*, World Scientific, 1987.

[Nak69] N. Nakanishi, *A General Survey of the Theory of the Bethe-Salpeter Equation*, Suppl. Prog. Theor. Phys. **43** (1969), 1.

[Nam60] Y. Nambu, *Axial Vector Current Conservation in Weak Interactions*, Phys. Rev. Lett. **4** (1960), 380–382.

[Nas89] D. Nash, *Higher-Order Corrections in (2+1)-Dimensional QED*, Phys. Rev. Lett. **26** (1989), 3024–3026.

[Nas91] C. Nash, *Differential Topology and Quantum Field Theory*, Academic Press, 1991.

[Ne'61] Y. Ne'eman, *Derivation of Strong Interactions from a Gauge Invariance*, Nucl. Phys. **26** (1961), 222–229.

[Neg97] J. W. Negele, *Understanding hadron structure using lattice QCD*, hep-lat/9804017, 1997.

[NJL61a] Y. Nambu and G. Jona-Lasinio, *Dynamical model of elementary particles based on an analogy with superconductivity. I*, Phys. Rev. **122** (1961), 345–358.

[NJL61b] Y. Nambu and G. Jona-Lasinio, *Dynamical model of elementary particles based on an analogy with superconductivity. II*, Phys. Rev. **124** (1961), 246–254.

[NO90] N. Nakanishi and I. Ojima, *Covariant Operator Formalism of Gauge Theories and Quantum Gravity*, Notes in Physics, vol. 27, World Scientific, 1990.

[O$^+$99] M. Ostrick et al., *Measurement of the neutron electric form factor G(E,n) in the quasifree H-2(e(pol.),e' n(pol.))p reaction*, Phys. Rev. Lett. **83** (1999), 276–279.

[OAvS00] M. Oettel, R. Alkofer, and L. von Smekal, *Nucleon properties in the covariant quark diquark model*, Eur. Phys. J. **A8** (2000), 553–566.

[Oet00] M. Oettel, *Baryons as Relativistic Bound States of Quark and Diquark*, Ph.D. thesis, Universität Tübingen, 2000, nucl–th/0012067.

[OHAR98] M. Oettel, G. Hellstern, R. Alkofer, and H. Reinhardt, *Octet and decuplet baryons in a covariant and confining diquark-quark model*, Phys. Rev. **C58** (1998), 2459–2477.

[OPvS00] M. Oettel, M. Pichowsky, and L. v. Smekal, *Current conservation in the covariant quark-diquark model of the nucleon*, Eur. Phys. J. **A8** (2000), 251–281.

[OS73] K. Osterwalder and R. Schrader, *Axioms for Euclidean Green's functions I*, Commun. Math. Phys. **31** (1973), 83.

[OS75] K. Osterwalder and R. Schrader, *Axioms for Euclidean Green's functions II*, Commun. Math. Phys. **41** (1975), 281.

[P$^+$99] I. Passchier et al., *The charge form factor of the neutron from the reaction H- 2(pol.)(e(pol.),e' n)p*, Phys. Rev. Lett. **82** (1999), 4988–4991.

[Pis84] R. D. Pisarski, *Chiral-Symmetry breaking in three-dimensional electrodynamics*, Phys. Rev. **D29** (1984), 2423–2426.

[Pol73] H. D. Politzer, *Reliable Perturbative Results for Strong Interactions?*, Phys. Rev. Lett. **30** (1973), 1346–1349.

[PS79] H. Pagels and S. Stokar, *The Pion Decay Constant, Electromagnetic Form-Factor and Quark Electromagnetic Selfenergy in QCD*, Phys. Rev. **D20** (1979), 2947.

[PS95] M. E. Peshkin and D. V. Schroeder, *An Introduction to Quantum Field Theory*, Addison-Wesley, 1995.

[PTVF92] W. H. Press, S. A. Teukolsky, W. T. Vetterling, and B. P. Flannery, *Numerical Recipes in Fortran*, Cambridge University Press, 1992.

[Qua99] M. Quandt, *Yang–Mills Theories in Abelian Gauges*, Ph.D. thesis, Universität Tübingen, 1999.

[Red84] A. N. Redlich, *Gauge Noninvariance and Parity Violation of Three-Dimensional Fermions*, Phys. Rev. Lett. **52** (1984), 18.

[Rei90] H. Reinhardt, *Hadronization of Quark Flavor Dynamics*, Phys. Lett. **B244** (1990), 316–326.

[RM90] C. D. Roberts and B. H. McKellar, *Critical Coupling for Dynamical Symmetry Breaking*, Phys. Rev. **D41** (1990), 672.

[RS00] C. D. Roberts and S. M. Schmidt, *Dyson-Schwinger equations: Density, temperature and continuum strong QCD*, Prog. Part. Nucl. Phys. **45S1** (2000), 1–103.

[RW94] C. D. Roberts and A. G. Williams, *Dyson-Schwinger Equations and Their Application To Hadronic Physics*, Prog. Part. Nucl. Phys. **33** (1994), 477.

[S$^+$75] S. Stein et al., *Electron Scattering at 4-Degrees with Energies of 4.5-GeV - 20-GeV*, Phys. Rev. **D12** (1975), 1884.

[SB51] E. E. Salpeter and H. A. Bethe, *A Relativistic equation for bound state problems*, Phys. Rev. **84** (1951), 1232–1242.

[Sch51] J. S. Schwinger, *On the Greens Functions of Quantized Fields. 1*, Proc. Nat. Acad. Sci. **37** (1951), 452.

[Sch59] J. Schwinger, *Euclidean quantum electrodynamics*, Phys. Rev. **115** (1959), 721.

[SRAL90] M. Schaden, H. Reinhardt, P. A. Amundsen, and M. J. Lavelle, *An Effective Action for Yang-Mills Field Strengths*, Nucl. Phys. **B339** (1990), 595–622.

[SS96] H. Suman and K. Schilling, *First Lattice Study of Ghost Propagators in SU(2) and SU(3) Gauge Theories*, Phys. Lett. **B373** (1996), 314–318.

[Sti96] M. Stingl, *A Systematic extended iterative solution for quantum chromodynamics*, Z. Phys. **A353** (1996), 423–445.

[SW01] J. I. Skullerud and A. G. Williams, *Quark Propagator in Landau Gauge*, Phys. Rev. **D63** (2001), 054508.

[T$^+$98] M. Q. Tran et al., *Measurement of gamma p - K+ Lambda and gamma p - K+ Sigma0 at photon energies up to 2-GeV*, Phys. Lett. **B445** (1998), 20–26.

[Tan97] P. C. Tandy, *Hadron physics from the global color model of QCD*, Prog. Part. Nucl. Phys. **39** (1997), 117–199.

[Tay71] J. C. Taylor, *Ward Identities and Charge Renormalization of the Yang-Mills Field*, Nucl. Phys. **B33** (1971), 436–444.

[tH82] G. 't Hooft, *The Topological Mechanism for Permanent Quark Confinement in a Nonabelian Gauge Theory*, Phys. Scripta **25** (1982), 133.

[TJZW85] S. B. Treiman, R. Jackiw, B. Zumino, and E. Witten, *Current Algebra and Anomalies*, Princeton Series in Physics, Princeton University Press, 1985.

[TRdS95] R. G. Timmermans, T. A. Rijken, and J. J. de Swart, *Lambda N K and Sigma N K couplings from LEAR PS-185 data*, Nucl. Phys. **A585** (1995), 143.

[vB98] P. v. Baal (ed.), *Confinement, Duality, and Nonperturbative Aspects of QCD*, NATO ASI Series B, vol. 368, Plenum Press, 1998.

[vS98] L. v. Smekal, *Perspectives for Hadronic Physics from Dyson-Schwinger Equations for the Dynamics of Quark and Glue*, Habilitationsschrift, Universität Erlangen-Nürnberg (1998).

[vSHA97] L. v. Smekal, A. Hauck, and R. Alkofer, *The Infrared Behavior of Gluon and Ghost Propagators in Landau Gauge QCD*, Phys. Rev. Lett. **79** (1997), 3591–3594.

[vSHA98] L. v. Smekal, A. Hauck, and R. Alkofer, *A Solution to Coupled Dyson-Schwinger Equations for Gluons and Ghosts in Landau Gauge*, Annals Phys. **267** (1998), 1.

[VW84] C. Vafa and E. Witten, *Eigenvalue Inequalities for Fermions in Gauge Theories*, Commun. Math. Phys. **95** (1984), 257.

[WA01] P. Watson and R. Alkofer, *Verifying the Kugo-Ojima Confinement Criterion in Landau Gauge QCD*, Phys. Rev. Lett. **86** (2001), 5239.

[Wei73] S. Weinberg, *Nonabelian Gauge Theories of the Strong Interactions*, Phys. Rev. Lett. **31** (1973), 494–497.

[Wic54] G. C. Wick, *Properties of Bethe-Salpeter Wave Functions*, Phys. Rev. **96** (1954), 1124.

[Wig56] A. S. Wightman, *Quantum field theories in terms of vacuum expectation values*, Phys. Rev. **101** (1956), 860.

[Wil74] K. G. Wilson, *Confinement of Quarks*, Phys. Rev. **D10** (1974), 2445–2459.

[YM54] C. N. Yang and R. Mills, *Conservation of Isotopic Spin and Isotopic Gauge Invariance*, Phys. Rev. **96** (1954), 191.

[ZAWR97] U. Zückert, R. Alkofer, H. Weigel, and H. Reinhardt, *Baryons as hybrids of solitons and three-quark bound states*, Phys. Rev. **C55** (1997), 2030–2042.

Curriculum Vitae

Persönliche Daten:

Steven Ahlig
Falkenweg 10
72076 Tübingen

geboren am :	18. Juli 1972 in Wippra
Familienstand :	ledig
Staatsangehörigkeit :	deutsch

Ausbildung:

- 9/1979 bis 6/1988 Polytechnische Oberschule in Vatterode
- 9/1988 bis 5/1992 A.-v.-Humboldt Gymnasium Lauterbach
- 5/1992 Abitur am A.-v.-Humboldt Gymnasium in Lauterbach
- 10/1992 bis 6/1997: Studium an der Universität Tübingen, Hauptfach Physik
- 6/1997 bis 6/1998: Diplomarbeit *'(In-)Konsistenzen in der Beschreibung relativistischer angeregter Zustände in der Bethe-Salpeter Gleichung'* unter Anleitung von PD Dr. R. Alkofer
- Abschluss 6/1998: Diplom-Physiker
- seit 6/1998 Promotion: *'Analytic Properties of the Quark Propagator: QCD, QED_3 and Kaon Photoproduction'* unter Anleitung von PD Dr. R. Alkofer

Stipendien und Beschäftigungen:

- 6/1997 bis 6/1998: Studentische Hilfskraft am Institut für theoretische Physik der Universität Tübingen
- 7/1998 bis 12/2000: Wissenschaftlicher Mitarbeiter am Institut für theoretische Physik der Universität Tübingen
- seit 1/2001: Stipendiat des Graduiertenkollegs: *'Hadronen im Vakuum, in Kernen und Sternen'*

Akademische Lehrer:

Alkofer, Baake, Baumann, Clement, Dittrich, Fischer, Gaukler, Gönnenwein, Grabmayr, Hartmann, Hasselbach, Hübener, Kaul, Klaeren, Kramer, Kümmerer, Lutz, Mertens, Müther, Pfister, Plies, Reinhardt, Riekers, Ruder, Schwenk, Staudt, Stumpf, Wagner,
Weigel, Wörz-Busekros

DANK

Mein Dank gilt vor allen dem Betreuer meiner Doktorarbeit Herrn Privatdozent Reinhard Alkofer. Seine Kompetenz, seine Ideen und Vorschläge sind auf vielfache Weise in diese Arbeit eingeflossen. Seine integre Art und seine Fähigkeit zu motivieren halfen oftmals über die – wohl unvermeidlichen – Durststrecken hinweg.
Herrn Professor Hugo Reinhardt danke ich für seine Unterstützung die insbesondere auch den Besuch der Konferenzen in Oberwölz und Erice angeregt und ermöglicht hat.
Mein besonderer Dank gilt auch Herrn Privatdozent Lorenz von Smekal. Sein Wissen, sein Ideenreichtum und auch seine sehr motivierende Art haben die Zusammenarbeit stets zu einem gleichermassen fruchtbaren wie angenehmen Ereignis werden lassen.
Ein herzlicher Dank geht an die Mannen des Diquark–Quark Projektes: Martin Oettel und Christian Fischer. Die gute Zusammenarbeit und das muntere Miteinander haben die Jahre am Institut und darüber hinaus wesentlich geprägt und zusätzlich aufgehellt.
Dank auch der gesamten Arbeitsgruppe; die Atmosphäre hätte kaum angenehmer und förderlicher sein können. Insbesondere möchte ich Oliver Schröder für ungezählte Diskussionen und Teepausen danken. Auch Laurent Moyaerts möchte ich besonders danken; für die sehr gute Stimmung im gemeinsamen Büro, für seine Expertise in Sachen ’Musik’ und für die Möglichkeit täglich und ganz nebenbei etwas Französisch zu lernen.
Ein besonderer Dank gilt meinen Eltern. Sie haben mich während meines gesamten Studiums und insbesondere auch während der Doktorarbeit in jeder Hinsicht unterstützt und gefördert.